Universitat Politècnica de Catalunya

Departament de Física Aplicada

Programa de Doctorat

Doctorat en Ciència i Tecnologia Aeroespacial

Transitional periods of the atmospheric boundary layer

Memòria presentada per

Estel Blay Carreras

per obtenir el títol de Doctora per la Universitat Politècnica de Catalunya.

Director:
David Pino Gonález

June 4, 2014

If there is effort, there is always accomplishment.

Jigoro Kano

Contents

Chapter 1

Introduction

The atmospheric boundary layer is the part of the troposphere influenced by the presence of the surface, and where some weather phenomena occur. During the day, with fair weather conditions, a convective boundary layer exists. In contrast, during the night, a stable boundary layer appears. It is important to note that the evolution from a convective boundary layer to a stable boundary layer and vice versa happens through two transitional processes. Due to its complexity and the rapid variability, there is a lack of studies about the morning or afternoon/evening transitions.

This thesis fills the lack of knowledge in the morning and afternoon/evening transition of the atmospheric boundary layer. It is based on observations from the project Boundary-Layer Late Afternoon and Sunset Turbulence and numerical simulation experiments and uses two different types of models with increasing complexity: mixed-layer and large-eddy simulation models.

1.1   Motivation and Context

Aviation is currently one of the most used transport for long distances, as it is the fastest and safest option. Over recent decades, there has been an increment in the number of flights, opening aviation to the general public. However, this increment in the number of flights has also increased the number of aircraft accidents caused by different factors, including atmospheric conditions (Luers and Haines, 1983; Pike, 1988; Shao et al., 2013). Even though, new technologies such as the traffic collision avoidance system or the low level wind shear alert system help to avoid different dangerous situations, there are still many aircraft accidents per year. Figure 1.1 shows the number of aircraft accidents every year from 1967 to 2010 (blue columns), which have tended to increase steadily, reaching some maxima in 1973, 1985, 2001 and 2005 (Lozano Sánchez, 2013). The figure was created using several international and national databases: the International Civil Aviation Organization, the Federal Aviation Administration, the National Transportation Safety Board, the Civil Aviation Authority and

Transport Canada, Aviation Safety Network, Airsafe, Airdisaster, Cabin Safety Research Technical Group, and Aircraft Crashes Record Office. The figure also shows the number of accidents related to weather conditions (red columns). There is a large variability of approximately 30% to 60% in the percentage of weather-caused accidents per year. In general, despite all the technological advances, current aircraft are still in danger in the face of unexpected meteorological conditions, with 43% being the mean of aircraft accidents caused by weather.
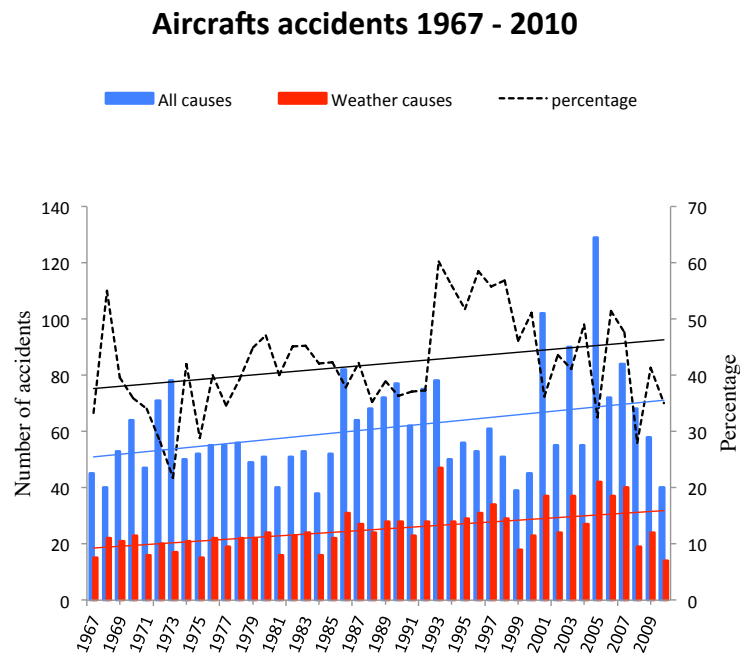
Figure 1.1: Aircraft accidents from 1967 to 2010 due to all causes (blue bars), caused by weather (red bars), and the percentage of those caused by weather in respect to all causes (dashed line). Courtesy of Jordi Mazón.

Figure 1.2 shows the relevance of each cause by weather in the different flight phases, which are: take-off, climbing, flight, descent, approach and landing (Lozano Sánchez, 2013). The atmospheric phenomena causing more accidents are: turbulence, fog, clear air turbulence (CAT), rain, icing, visibility, snow and storms. This figure shows that turbulence and visibility are the main causes of weather-aircraft accidents. Turbulence causes around 62% and 56% of accidents in the flying and descending phases, respectively, with some influence to a lower extent in the other phases. Low visibility is crucial in ground operations, as it causes approximately 54% of the accidents during take-off, 51% during the climb, and 36% during the landing phase.

In this thesis, we focus on the study of two specific periods of the diurnal
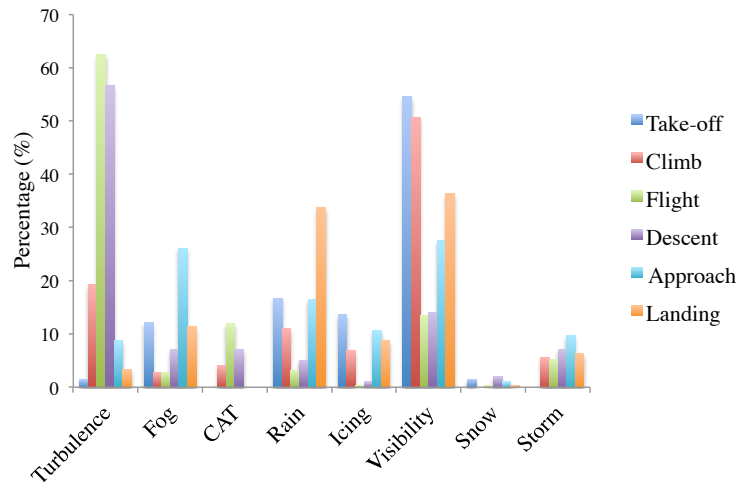
Figure 1.2: Percentage of the main types of weather causing aircraft accidents in the different phases of flight. Courtesy of Jordi Mazón.

cycle of the atmospheric boundary layer (ABL). ABL is the lower part of the troposphere influenced by the presence of the surface, and where some weather phenomena occur. It is usually around 1 km deep, but at mid-latitudes it can vary from 100 m to 3 km. It is in this part of the atmosphere where most of the dangerous phases of the flight occur, the ones with the highest quantity of accidents: descending, approaching and landing, as well as taking off and climbing. The main reason for this danger is the proximity to the ground, the lower aircraft speed, the large number of maneuvers and, also, because the density of airplanes in the airspace is very high. According to Boeing statistical studies, 16% of fatal accidents occur during takeoff and the initial climb, while 29% occur during approach and landing (Boeing, 2009). Therefore, a better understanding of the atmospheric boundary layer can help to offer more consistent, timely and accurate weather information for the world airspace system, which can definitely reduce the aircraft accidents caused by weather.

The ABL has a marked diurnal cycle, as shown in Fig. 1.3. On clear days during daytime, a convective boundary layer (CBL) exists, where the conserved variables (heat, moisture and atmospheric constituents) are constant with height. During the night, CBL evolves to a stable boundary layer (SBL), which consists of vertical layers with different thermodynamic characteristics due to the competition between mechanical mixing and the stabilizing effects of the radiation cooling at the ground. The evolution from CBL to SBL, and vice versa, happens through two transitional processes, which will be described in detail in the following sections. We focus our research on these transitional periods,
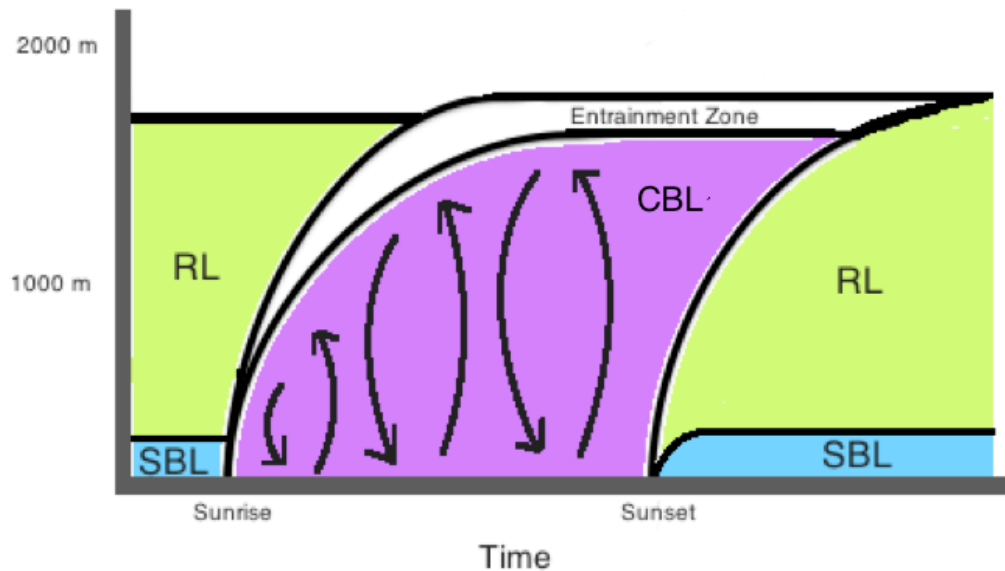
Figure 1.3: Sketch of the diurnal cycle of the Atmospheric Boundary Layer.

where there is a lack of knowledge (Angevine, 2008; Lothon et al., 2014) and where also there is a high amount of air traffic (Graf et al., 2012).

   To summarize, main motivation of this thesis is to obtain a better under-standing of the transitional periods of the atmospheric boundary layer.

1.2   The Atmospheric Boundary Layer

Figure 1.3 shows the general structure and evolution of the ABL over land. During daytime, in fair weather conditions, the sun warms the earth's surface and, as a consequence, the air close to it. Therefore, this air has lower density than its surroundings (it is positively buoyant), and can ascend in the form of large energetic eddies (also known as thermals) and thereby form a convective boundary layer. During this upward movement, the air cools adiabatically. At some point, the positive buoyancy ceases and the rising air stops at the atmospheric boundary-layer depth (z_1), which defines the top of the mixed layer (ML). ML is characterized by intense mixing driven by convective turbulence. Inside the ML, this intense turbulence produces vertically uniform values of the thermodynamic variables and other atmospheric constituents, such as potential temperature (θ), specific humidity (q) or some trace pollutants. Above the ML, there is the free atmosphere (FA), where the effects of the earth's surface are nearly negligible, which causes the wind to be approximately geostrophic. Here,
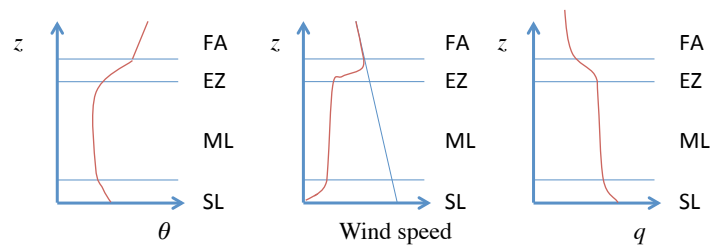
Figure 1.4: From left to right, an illustration of the vertical profile of potential temperature, specific humidity, and wind speed in ABL during daytime.

viscous dissipation and molecular diffusion are low, and there is often rapid horizontal transport by mean wind. ML and FA are separated by an inversion or entrainment zone, marked by a jump (increase or decrease) in the atmospheric thermodynamic variables or compounds. In this zone, there is an interchange of heat, humidity, momentum and other compounds between ML and FA.

The atmospheric characteristics of the ABL are largely determined by its heat, momentum and moisture budgets, which are primarily driven by atmospheric turbulence. Figure 1.4 illustrates the vertical profile of these relevant variables (potential temperature, specific humidity and wind speed) of the ABL in convective conditions. The figure defines the surface layer (SL) (normally occupying the bottom 10% of the ABL), as well as the ML, the entrainment zone (EZ) and the free atmosphere.

From midday, turbulence starts to decay, due to the decrease in the surface flux, and the transition period begins. This is followed by the formation of the stable boundary layer. During nighttime, due to the radiative cooling of the ground, a stable layer is created next to the surface. The stable boundary layer is characterized by weak and sporadic turbulence. Above this layer, there is the residual layer (RL), a reminiscence of the diurnal convective boundary layer, where light turbulence can continue during the night. Figure 1.5 shows the vertical profile of the same variables presented in Fig. 1.4, but during the nighttime, when the stable boundary layer and the residual layer exist.

The increasing knowledge of the ABL processes has been based on two main types of studies: the application of the theoretical concepts of turbulence (Batchelor, 1967; Tennekes, 1973; Pope, 2000) to perform numerical simulations of the atmospheric characteristics (Lilly, 1966b; Deardorff, 1972; Lenschow, 1974; Stull, 1976; Jacobson, 2005; Pielke, 2002; Stensrud, 1993); and detailed observations recorded during various intensive campaigns: Wangara 1967, Kansas 1968, or Minnesota 1973, CASES 99, BLLAST 2011 (Hess et al., 1981; Kaimal and Wyngaard, 1990; Poulos et al., 2002; Svensson et al., 2011; Lothon et al., 2014). Moreover, there are currently systematic observations being taken at Boulder (USA) or Cabauw (Van Ulden and Wieringa, 1996; The Netherlands). Most of the studies were devoted to investigating the ABL characteristics and the relevant processes, either during the day (when unstable or neutral conditions
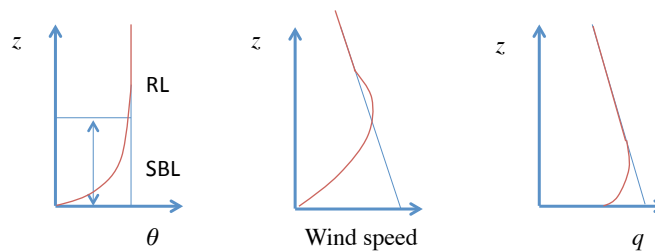
Figure 1.5: From left to right, an illustration of the vertical profile of potential temperature, specific humidity and wind during the night.

usually prevail (Kaimal et al., 1976; Mahrt and Lenschow, 1976; Stull, 1988; Moeng and Sullivan, 1994; Cuijpers and Holtslag, 1998)) or at night (when a stable atmosphere is usually found (Nieuwstadt, 1984; Garratt, 1994; Derbyshire, 1990; Cuxart et al., 2000; Beare et al., 2006b)). However, only a few studies have dealt with the transitions between day and night, where the atmosphere's stability changes rapidly.

1.3 Transitions of the Atmospheric Boundary Layer

The ABL experiences two transitional periods during the day (see Fig. 1.3). The morning transition is initiated when the surface sensible heat flux becomes positive and a shallow entraining ML grows into the surface inversion (Angevine et al., 2001; Lapworth, 2006; Edwards et al., 2006; Nunes et al., 2010). The evening transition is initiated when the surface sensible heat flux becomes negative, and it typically consists of the decay of the convective turbulence under the action of dissipation (Nieuwstadt and Brost, 1986; Sorbjan, 1997; Pino et al., 2006b; Rizza et al., 2013; Nadeau et al., 2013), even thought the decay, for instance of TKE, can start earlier, followed by the growth of a stable boundary layer from the surface under the action of surface cooling.

The evening and morning transitions have some distinct dynamical mechanisms and thus may require separate studies. Despite there being similar main physical phenomena which control both transitions (surface fluxes, stratification and wind shear), during the afternoon, there are some additional effects (such as radiation, subsidence, or advection) which yield to a much more complicated scenario (Vilà-Guerau de Arellano, 2007; Angevine, 2008; Pietersen et al., 2014). Moreover, during the evening transition, defining the boundary layer itself is difficult (Grimsdell and Angevine, 2002; Nadeau et al., 2011), since there is no agreement, for instance, on the scaling law to apply (Pino et al., 2006b; Van Driel and Jonker, 2011; Sorbjan, 2010).

Some studies (de Arellano et al., 2004; Casso-Torralba et al.; Ouwersloot et al., 2012) have shown that both transitions are also important for the exchange of species. At night the residual part overlying the stable layer can be

ventilated in the free troposphere, so that water vapor and pollutants emitted at the surface and diluted into the convective layer during the day can be introduced into the free atmosphere and transported on a larger scale. In contrast, when high entrainment rates have been observed in the early morning (de Arellano et al., 2004), the remaining pollutants of the residual layer modify their concentration when they are introduced into the shallow boundary layer.

Several authors have previously studied the transitional regimes of turbulence. Through laboratory experiments, Monin et al. (1975) studied the decay of grid–generated turbulence under neutral conditions. During the decay, the turbulence maintains the initial isotropy, with the energy decay following a power law t^{-n}, t being time. Cole and Fernando (1998), by performing an experiment in a water tank, studied the decay of temperature and velocity fluctuations in a convective turbulent boundary layer in response to cooling at the surface. They found that, when the cooling rate is constant, the decay times of turbulent velocity and temperature scale with the temperature difference between the cooling surface and the mixed–layer temperature divided by the cooling rate. Stillinger et al. (1983) studied the decay of homogeneous turbulence in a uniform stratification, showing that turbulence becomes highly anisotropic. On the other hand, turbulence decay has also been studied by using theoretical models (George, 1992), large–eddy simulation models (LES) (Touil et al., 2002; Svensson et al., 2011; Darbieu et al., 2012a; Rizza et al., 2013) or direct numerical simulations (DNS) (Biferale et al., 2003).

Regarding the transitions in the ABL, the morning evolution from a stable boundary layer has been studied using observations by Angevine et al. (2001); LeMone et al. (2002); Lapworth (2006); Bange et al. (2007) and Sokol et al. (2014). Angevine et al. (2001) describe a comprehensive set of morning transition LIDAR observations from flat locations, and they conclude that shear is important in controlling the timing of morning convection onset. Lapworth (2006) presented 6 years of observations and found that the near-surface wind and screen temperature are proportional by a factor that depends on the gradient wind. Both studies highlight the important role of wind shear during the morning transition. Bange et al. (2007) used a helicopter probe to measure the characteristics of the morning shallow convective boundary layer. By measuring the buoyancy flux vertical profile, they concluded that entrainment was the most important mechanism for shallow convective boundary layer growth.

The morning transition has also been studied by means of numerical simulations (Sorbjan, 2007; Beare, 2008). Sorbjan (2007) performed LES numerical experiments on the growing convective boundary layer phase of the morning transition, with simulations forced by different geostrophic winds and different initial stratifications in the FA. He compared a similarity relation for the entrainment velocity (based on the depth of the maximum potential temperature gradient) with the simulations, and found they agreed reasonably. Beare (2008) found that, in the early stages of the morning transition, the boundary layer is a combination of a shallow ML capped by a significant shear-driven stable boundary layer. He called it a "mixed convective-stable boundary layer state".

The decay of convective turbulence during the afternoon in the ABL has

been analyzed by Goulart et al. (2003) using theoretical models; by Nieuwstadt and Brost (1986); Sorbjan (1997); Goulart et al. (2003); Beare et al. (2006a); Darbieu et al. (2012b); Goulart et al. (2011) by means of LES; by Edwards et al. (2006); Svensson et al. (2011) using single column models; and Shaw and Barnard (2002) used DNS to study the same problem. Moreover, Caughey and Kaimal (1977); Grant (1997); Acevedo and Fitzjarrald (2001); Grimsdell and Angevine (2002); Anfossi et al. (2004); Fitzjarrald et al. (2004); Edwards et al. (2006); Rizza et al. (2013) reported some observations, and in some cases compared these with LES results.

Regarding the observations, it is important to emphasize the results obtained by Grimsdell and Angevine (2002). By using wind profiler observations, they found that there existed a decrease in the height and intensity of the turbulence during the afternoon. The beginning of the transition period started well before sunset. They defined two types of transition based on the presence of an intense return of the backscatter signal. However, Angevine (2008) declared that there is only one type of transition formed by a boundary layer which decreases with time and that has a residual layer above at an approximately constant height. Therefore, there is no general agreement on how to describe the afternoon and evening transition periods and their characteristics (Lothon et al., 2014).

The decay of turbulent kinetic energy (TKE) during the afternoon transition was first analyzed by Nieuwstadt and Brost (1986). He based his analysis on a shearless and cloudless ML, where TKE decays as a result of a sudden shut-off of the upward surface heat flux, according to power law t^{-n} . Later, Sorbjan (2007) studied TKE decay considering a gradual change of the heat flux with time, showing a decrease based on two time scales: the time scale of the gradual change of the heat flux and the convective velocity scale. Recently, Nadeau et al. (2011) analyzed TKE decay considering realistic decreases in surface sensible heat flux. They observed that TKE decays in two stages. During the first stage (afternoon transition), the decay is slow, but during the second stage (evening transition) there is a rapid collapse of turbulence. Moreover, they were able to model the decay observed in the surface layer with a model based on mixed-layer theory.

Some of the previous numerical works and observations have shown two particular features of the evening transition: first, the existence of important vertical movements (1 m s^{-1}) during the later afternoon transition; and second, the evolution of the characteristic length scales of the fundamental variables in these moments (Lothon et al., 2014).

The characteristic length scales during the evening transition still remain an open question, and it is basic for completely understanding the physics controlling the ABL during the evening. Keeping in mind that the length scales of the CBL (Jonker et al., 1999) and the SBL are different, during the afternoon transition some kind of evolution has to occur. Nieuwstadt and Brost (1986) found that the length scale of maximum spectral energy of the vertical velocity remained constant during the decay process. On the other hand, Sorbjan (1997) asserted that convection persisted in the decaying ML even when the buoyancy flux at the surface became negative, because small eddies decayed earlier than

large eddies. Also, he showed that the evolution of the decaying ML is governed by two scales: one external time scale related to the time evolution of the surface heat flux and the convective time scale. The ratio between these two time scales has not been deeply investigated and it can control the setup of the nighttime stable boundary layer. Moreover, Pino et al. (2006b) analyzed the weighted integral of the density energy spectrum to show that the characteristic length scale has a different evolution during the decay.

By using numerical models and observations, Emeis and Schäfer (2006); Balsley et al. (2008) and Wehner et al. (2010) showed the existence of a turbulent residual layer, uncoupled from the surface, which can produce large scale vertical movements enhancing the entrainment fluxes. These results might seem in contradiction with the turbulence principles, which say that small eddies are generated from larger eddies (inertial cascade), even in cases where there is no turbulence source (Batchelor, 1982). However, there is no contradiction, because in the decaying convective turbulence process small eddies dissipate faster than larger ones, necessarily increasing the characteristic length scales (Jonker et al., 1999; Pino et al., 2006b; Sorbjan, 2010; Van Driel and Jonker, 2011). Moreover, variables present during the decaying turbulence had a different evolution of the characteristic length scale. This result was also observed in the real atmosphere (Fitzjarrald et al., 2004). In this work, six cases of the evening transition from convective to stable boundary layers were observed by means of flux towers and aircraft measurements. They clearly observed a decrease in the dominant length scale of the vertical velocity variance, though the characteristic length scales of the horizontal velocity variances decreased more slowly, or they even increased during some of the nights. Therefore, the differences in the exponent of the decaying variances of the three components of the velocity are a clear indication that the turbulence does not relax to an isotropic state during the decay process.

1.4   Research strategy

The research strategy of this thesis is based on the study of different specific issues which have remained poorly explored during transitional periods of the atmospheric boundary layer. Due to the special characteristics of the transitional periods, which involve fast changes in conditions, several unresolved questions arose that were considered during the Boundary-Layer Late Afternoon and Sunset Turbulence (BLLAST) project. The following chapters describe the studies developed, thanks to the observations obtained during the BLLAST field campaign. In some cases, we also use two different models (mixed-layer model (MLM) and LES).

The measurements obtained with BLLAST are used directly to develop and verify the hypothesis as well as to initialize and validate the model results. BLLAST measurements are useful for the development of this thesis, as they focus mainly on the late afternoon transition. Moreover, given the large amount of data obtained from several in situ and remote sensing instruments (full-size aircraft, Remotely Piloted Airplane Systems, remote sensing instruments, radio

soundings, tethered balloons, surface flux stations, and various meteorological towers) over different terrains, we are able to test the suggested hypothesis and avoid the consideration of measurement errors.

Furthermore, the use of models helps us understand the behavior of some processes. In this thesis numerical models are used mainly to analyze the importance of the residual layer and the subsidence in the development of the boundary layer in the morning transition.

In the next section the methodology used in the research studies is explained in detail.

1.5 Methodology

The methodology used to develop this thesis is based on two numerical models, a MLM and a LES model, and the observations recorded during the BLLAST field campaign.

1.5.1 Mixed-layer model

Mixed-layer theory (Lilly, 1968; Tennekes, 1973; Tennekes and Driedonks, 1981; Carson, 1973) helps us to interpret many of the numerical experiment results and observations presented in this thesis. Mixed-layer theory assumes constant values of some atmospheric variables within the ML with a sharp jump at the top of the mixed-layer. By so doing, the thermodynamic equations are simplified assuming that the turbulence inside the boundary layer is intense enough to maintain vertical homogeneous distributions of scalar variables. The surface layer is considered negligible as it is really thin compared with the ML and the inversion is taken either to be infinitesimally thin or to have a finite thickness (see Vilà-Guerau de Arellano and van Heerwaarden, 2014 for a complete explanation of mixed-layer theory).

Figure 1.6 illustrates the vertical profile of potential temperature and its corresponding vertical heat flux as assumed in the mixed-layer theory showing the simplicity of the model. The negative heat flux around z_1 is the entrainment flux produced by the warm air entering the ML from the free atmosphere. Above this entrainment zone, the thermodynamic variables are characterized by the conditions in the FA assumed linear with height in the MLM (Vilà-Guerau de Arellano and van Heerwaarden, 2014).

In this thesis, the zero-order ML assumption was used. In this assumption, the vertical profiles of the variables show a discontinuity at the height of the inversion from the ML values to free atmospheric ones.

As shown in Fig. 1.6, potential temperature in the mixed-layer theory remains constant with height and its vertical distribution is independent of height in the ABL. Therefore, the vertical gradient of the potential temperature remains unchanged over time and the potential temperature vertical flux is linear with height. This condition is called a quasi steady-state condition. A similar approximation can also be used for other variables like specific humidity, which
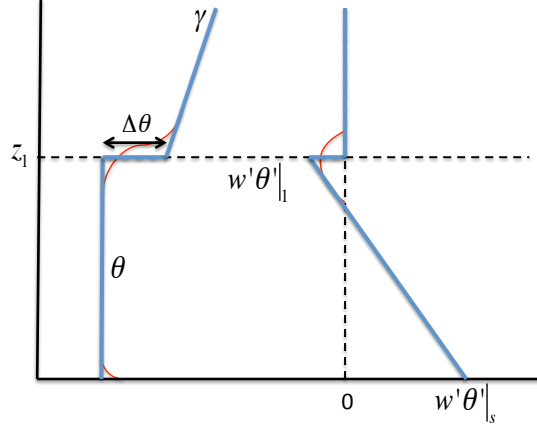
Figure 1.6: Schematic representations of the vertical profiles of the virtual potential temperature and virtual potential temperature flux by means of a zero-order MLM (blue line). The thin red line is an approximated real profile.

without phase changes is a conserved variable as well as a mixing ratio for some atmospheric constituents.

If we assume that potential temperature flow has horizontally homogeneous properties ($\frac{\partial \bar{\theta}}{\partial x} = \frac{\partial \bar{\theta}}{\partial y} = 0$), and that the mean vertical velocity is zero in the ML, the time evolution of the mean potential temperature (integrated from 0 to z_1) in the ML ($\bar{\theta}$) under convective conditions is driven by surface and entrainment heat fluxes only, and reads (Tennekes and Driedonks, 1981):

$$\frac{\partial \bar{\theta}}{\partial t} = \frac{\overline{\omega'\theta'}|_{\mathrm{s}} - \overline{\omega'\theta'}|_1}{z_1}, \tag{1.1}$$

where $\overline{\omega'\theta'}|_{\mathrm{s}}$ and $\overline{\omega'\theta'}|_1$ are the turbulent heat flux at the surface and at z_1 (entrainment heat flux), respectively. A similar equation can be used for the tendency of any scalar ($\bar{c}$) in the ML, changing $\overline{\omega'\theta'}|_{\mathrm{s}}$ and $\overline{\omega'\theta'}|_1$ by the turbulent scalar fluxes at the surface and at z_1 ($\overline{\omega'c'}|_{\mathrm{s}}$ and $\overline{\omega'c'}|_1$).

In Fig. 1.6, we can observe the negative vertical heat fluxes around z_1. The entrainment heat flux has an important role in the evolution of the mean potential temperature, because it is responsible for the exchange of heat between the CBL and the FA. The evolution of entrainment heat flux is driven by the inversion jump and the boundary-layer depth growth rate as :

$$\overline{\omega'\theta'}|_1 = -\Delta\theta_1 \frac{\partial z_1}{\partial t}, \tag{1.2}$$

where $\Delta\theta_1$ is the jump in potential temperature at the inversion.

To compute Eq. 1.2, the conditions of discontinuity between the free tro-
posphere and the boundary layer represented by the inversion jump are used.
Therefore, the potential temperature inversion jump has to be defined through
the increase in mixed-layer depth, which is influenced by the subsidence ve-
locity and also results from the variation of mean potential temperature. The
evolution of the potential temperature inversion jump reads:

$$\frac{\partial \Delta \theta_1}{\partial t} = \gamma \frac{\partial z_1}{\partial t} - \frac{\partial \bar{\theta}}{\partial t}, \quad (1.3)$$

where γ is the potential temperature lapse rate above the inversion.

It is important to note that the MLM equations are not a closed system
of equations. Therefore, we need to include an additional equation to close
it. Usually, this equation relates the surface and entrainment heat fluxes as
(Tennekes and Driedonks, 1981):

$$\overline{\omega'\theta'}|_1 = -\beta \, \overline{\omega'\theta'}|_s, \quad (1.4)$$

where β is usually a constant value prescribed in the model (Tennekes and
Driedonks, 1981).

Although MLM is a simple model, it has been proven to correctly describe
the evolution of the convective boundary layer (Pino et al., 2003; Conzemius
and Fedorovich, 2006; Ouwersloot et al., 2012). Therefore, MLM can be used
to create rapid and simple characterization of the CBL and the results can
be contrasted with the results from more complex numerical models, such as,
Large-Eddy Simulation models.

1.5.2 Large-eddy simulation

Large-eddy simulation is a numerical method based on the idea that atmo-
spheric turbulent flows contain a wide range of length and time scales. LES
models explicitly resolve the turbulent scales larger than a certain length and
that contain the largest part of the flow energy. The resolved part of the spec-
trum usually contains approximately 90% of the turbulent energy, even though,
this percentage may vary depending on the stratification, or the selected grid
resolution. LES models parameterize the smaller scales, which are less energetic
(Ferziger and Peric, 2002; Lesieur et al., 2005). The most energetic eddies in
the ABL have the size of the ABL height (around 1 km). On the other hand,
the smallest eddies are usually 10^6 times smaller, and these are parametrized in
LES (see Fig. 1.7). They are almost irrelevant in transfer processes, but they
are responsible for other phenomena such as the dissipation of kinetic energy.

LES models has been used to study the aerodynamics from cars to turbo
machinery, as well as for the atmospheric boundary layer, including convective
and stable boundary layers over recent decades. A LES model used to study the
atmospheric boundary layer is based on the first concepts of Deardorff (1972)
and Lilly (1966a). A LES model is a three-dimensional model, time dependent
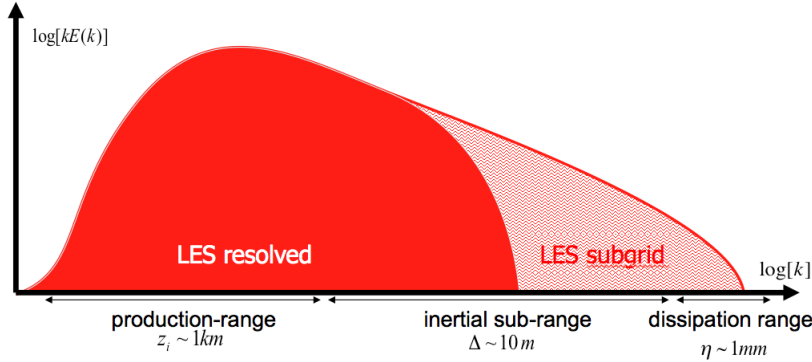
Figure 1.7: Schematic representations of the LES spectrum boundary layer turbulence.

and expensive, but much less costly than DNS, where all the scales are explicitly resolved. Moreover, LES is the preferred method for flows in which the Reynolds number is too high, owing to the excessive number of degrees of freedom or because the geometry is too complex to allow application of DNS.

The specific LES model used to develop parts of this thesis is the Dutch Large-Eddy Simulation model (DALES, Heus et al., 2010). DALES is based on the model first developed by Nieuwstadt and Brost (1986) and later modified and improved on by several scientists. For instance, Cuijpers and Duynkerke (1993) were the first to introduce a complete humidity and condensation scheme, and Ouwersloot et al. (2011) included the option of introducing different heterogeneous surface conditions. The Boussinesq approximation is applied in the filtered Navier-Stokes equations, which are the equations resolved in the model. On the other hand, the parametrization for the smaller scales is based on a-half-order closure assumption.

1.5.3 Observations

The measurements taken during the BLLAST field campaign are used to develop the research studies presented in this thesis. The campaign was performed during June and July 2011 in the south of France. Its objective was to measure precisely with in situ and remote sensing measurements the atmospheric afternoon/evening transition in order to try to solve a set of unknowns which surround this period of the diurnal evolution of the ABL. These unknowns can be summarized as:

- *Definitions of the transition periods.* Description of the afternoon transition and the evening transition vary, depending on the source (Grimsdell and Angevine, 2002). BLLAST aimed to develop a deep study of the transition period following a clear and concise description based on

Nadeau et al. (2011). Specifically, they described that the afternoon transition starts as soon as the surface buoyancy flux begins to decrease and ends when it becomes negative. On the other hand, they defined that the evening transition is the transition from the zero-buoyancy flux to a well-established nocturnal layer.

- *Competing forcing during the afternoon transition.* The surface buoyancy flux decreases towards zero during afternoon transition, and other competing forcing processes become important such as radiation, advection, entrainment or wind shear (Pino et al., 2006b; Van Heerwaarden and Vilà-Guerau de Arellano, 2008; Angevine, 2008). BLLAST wanted to analyze the influence and interaction of these forces during afternoon transition.

- *TKE decay.* Several authors studied the decay of TKE with numerical simulations and observations (Nieuwstadt and Brost, 1986; Sorbjan, 2007; Nadeau et al., 2011). There is no consensus on the exact relationship between the forcing and the power law, which we expected to study during BLLAST.

- *Scaling and the evolution of length scales.* The evolution of length scales has been one of the main questions addressed in past studies on the afternoon transition. However, it remains unclear and only partly understood because it is not really know how the eddies evolve during this period. Moreover, BLLAST wanted to analyze which kind of scaling is more appropriate, based on Nadeau et al. (2011)'s definition of afternoon and evening transition: convective scaling, stable boundary-layer scaling or a new scaling (Sorbjan, 2010; Van Driel and Jonker, 2011; Sorbjan, 2012).

Apart from these unknowns, observations from the BLLAST field campaign are also used in this thesis to study near surface temperature and flux evolution during the afternoon transition. Specifically, we focus on the study of Monin-Obukov Similarity Theory (MOST) during afternoon transition. MOST is well proved during daytime (Businger et al., 1971). However, during afternoon transition, when the log-surface layer disappears really close to the ground, the gradient-theory fails. Consequently, negative surface heat flux is observed in combination with a positive gradient of potential temperature (Sahlée et al., 2007; Smedman et al., 2007). Moreover, we wanted to make a special effort to analyze the lifted minimum temperature during afternoon transition. This phenomenon has been studied under stable conditions since the thirties (Ramdas and Atmanathan, 1932; Raschke, 1957; Narasimha and Vasudeva Murthy, 1995; Mukund et al., 2013), but it has never been previously observed or analyzed during transitional periods. The lifted minimum temperature is not directly connected with the main unknows defined for BLLAST campaign, even though, the large amount of data collected during BLLAST give us the opportunity to go in deep in this phenomenon.

1.6   Thesis outline

This thesis is structured in six different chapters, four of which are based on studies accepted by or submitted to scientific journals.

After the brief introduction, motivation and theoretical approach, Chapter 2 describes in detail the Boundary-Layer Late Afternoon and Sunset Turbulence field experiment. This chapter consists of a description of the motivation of the project as well as a description of the field campaign, which includes the strategy plan and all the characteristics of the instruments used. Moreover, a general description of the meteorological conditions of the Intensive Operation Periods is also included.

In Chapter 3, we study the role of the residual layer and large-scale subsidence in the development and evolution of the convective boundary layer. The main motivation was to improve the knowledge about morning transition through the analysis of the role played by residual layer and the subsidence during this period of the day and on the diurnal evolution of the convective boundary layer. This chapter also shows the results obtained by a sensitivity analysis of the residual layer and subsidence. We show the differences in: the potential temperature vertical profile; the mixed-layer temperature temporal evolution; the boundary-layer depth temporal evolution; the entrainment heat flux and momentum fluxes; the turbulent kinetic energy budget, with and without consideration of the residual layer; and subsidence in the models' initial profiles. Finally, we analyze the influence of the residual layer on the observed evolution of the CO_2 mixing ratio.

In Chapter 4, we analyze the counter-gradient heat flux observations during the evening transition period. The main motivation was to define and quantify a failure in the flux gradient theory. We compare the convective time with the delay time, defined by the difference between the instant when the buoyancy flux goes to zero and the time when the local gradient of the virtual potential temperature changes sign. Moreover, we conduct an analysis of the Monin-Obukhov length to describe the convective characteristics and to contrast it with the duration of the delay time. To finalize the study, we analyze the Turbulent Rayleigh number to observe the importance of thermal diffusivity and viscosity in the enlargement of this delay.

Chapter 5 consists of a study of the lifted temperature minimum during evening transition. Our main objective was to describe the phenomenon during a period of the diurnal cycle of the atmospheric boundary layer, which is different from previous studies. We analyze the wind conditions to observe the importance of orography during this period of the day. We analyze the importance of turbulence to observe this phenomenon. Finally, we observe and describe its radiative origin.

Finally, Chapter 6 summarizes the main results obtained in the previous chapters, and it also includes an outlook for future work which could be developed.

Chapter 2

Boundary–Layer Late Afternoon and Sunset Turbulence (BLLAST) field experiment

[1]

The aim of the Boundary-Layer Late Afternoon and Sunset Turbulence (BLLAST) project is to study the processes occurring during the afternoon transition of the atmospheric boundary layer. The researchers of this project are an international group of scientists working from different research centers in Europe and the USA. One of the main goals of the BLLAST project was to perform an observational campaign focused on obtaining accurate and reliable measurements during the Late Afternoon Transition.

2.1   Motivation

As explained in the previous chapter, the CBL has been studied since the fifties. For instance, the overland growth of the CBL due to solar heating of the Earth's surface has been extensively observed and successfully modeled (Moeng and Sullivan, 1994; Sorbjan, 1996; Fedorovich et al., 1996; Yi et al., 2001). In contrast, the transitional periods (either when the CBL emerges from the nocturnal stable boundary layer or when the CBL decays to an intermittently turbulent residual layer that overlie a stably-stratified boundary layer) are difficult to measure and

---

[1]The content of this chapter is under review to be published in Atmospheric Chemistry and Physics as M. Lothon et al.: The BLLAST field experiment: Boundary Layer Late Afternoon and Sunset Turbulence, Atmos. Chem. Phys. Discuss., 14, 10789-10852, 2014

model, and have therefore received less attention until recently. During the last years few studies, like Beare et al. (2006a), model the entire evening transition and the nocturnal boundary layers. The main difficulties related with these periods are turbulence intermittency and anisotropy, horizontal heterogeneity, and rapid time changes. Even the definition of the boundary-layer depth during these transitional periods is not clear, because there is no consensus on what criteria to use and no simple scaling laws to apply (Angevine, 2008).

Afternoon transition remains largely unexplored, from both the modeling and observational point of view. The objectives of the BLLAST 2011 field experiment were to obtain more and better observations of the afternoon transition, so as to better understand the physical processes that control it, and to elucidate the role of the afternoon transition on mesoscale and turbulent-scale motions, as well as on the transport of species.

2.2 Experimental area

The BLLAST field campaign was performed from 14 June to 8 July 2011 in the surrounding area of Lannemezan (France). The area also known as Plateau de Lannemezan is a relatively flat plateau with an area of ca. 200 km^2 located close to the Pyrenees Mountains and the Spanish border (see Fig. 2.1a). The experimental area has approximately the same distance between the Mediterranean sea and the Atlantic ocean. Moreover, it is aligned with a main S-N oriented valley, which begins to the south of the plateau.

The terrain is covered by heterogeneous vegetation, which can be mainly described as grassland, meadows, crops and forest, as shown in Figs. 2.1b and 2.2. As a general idea, under calm conditions a mountain-plain circulation governs the low troposphere, with a northerly flow over the Plateau during daytime that turns to southerly during nighttime.

2.3 Observations

The BLLAST campaign consisted of 11 Intensive Observational Periods (IOPs) distributed over 3.5 weeks.

The general strategy of the observations was based on the simultaneous use of in situ and remote sensing measurements. There were some instruments which took measurements constantly during the entire campaign, such as the Eddy Covariance stations (EC-stations) and remote sensing. There are some others which took measurements only during the afternoon transition of the IOPs; some examples of which are radio soundings, balloons or aircraft.

The campaign area was divided into three different sites, where most of the instruments were located and the aircraft and the Remotely Piloted Aircraft Systems (RPASs) overflew to take their measurements. Figure 2.1b shows a general view of the site distribution over the Plateau de Lannemezan.

Each of these sites was designed with a precise scientific individual objective.
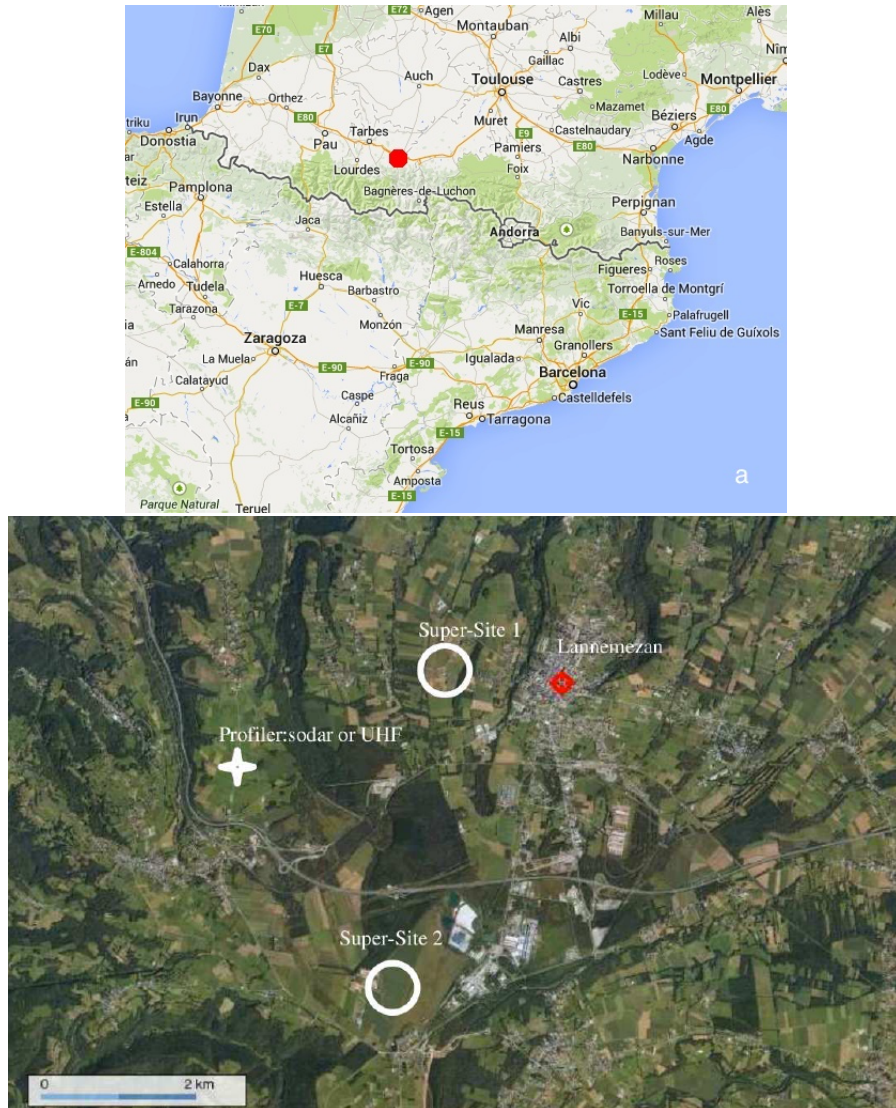
Figure 2.1: (a) Map view showing the location of BLLAST field campaign (red marker) and (b) zoom of the BLLAST field campaign area with the three sites marked by two circles and one cross. Courtesy of Marie Lothon.
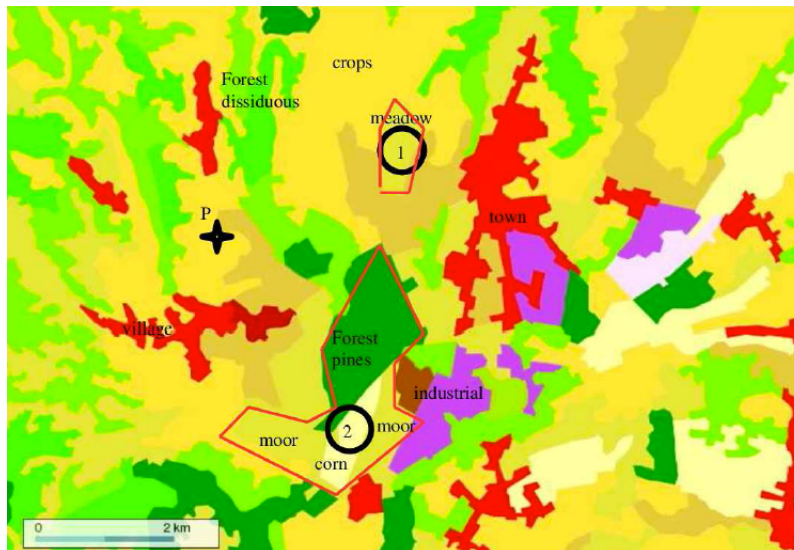
Figure 2.2: Land use types surrounding the BLLAST site with the three sites marked by two circles and one cross. Courtesy of Marie Lothon.

The objective of the first one (Supersite 1) was to analyze the vertical structure of the lowest part of the atmosphere during the afternoon/evening transition. To achieve this objective, Supersite 1 included a sodar, wind profilers, a microwave radiometer, a ceilometer, a backscatter lidar, a Doppler Lidar, a 60-m high tower instrumented every 15 m, a radiative divergence tower, radio soundings and tethered balloons. All the instruments in Supersite 1 were divided into 5 different sites, which were: a vertical monitoring site, a 60-m tower site, a divergence site, an edge effect site and a micro-scale surface heterogeneity site. Figure 2.3 shows the distribution of the sites in Supersite 1.

Supersite 2 was designed to study the effect of terrain heterogeneity during the afternoon transition. To measure the structure and evolution of the transition among different vegetated surfaces, several sonic anemometers (SA) were deployed over three adjacent surfaces: moorland, a maize field and a forest. Additionally, several soundings were made with two tethered balloons and RPASs. Figure 2.4 shows the distribution of sites over different land uses in Supersite 2.

Finally, to study the 3D atmospheric circulation, we created Supersite 3 and equipped it with an acoustic Doppler Sodar which closed a triangle formed also by two UHF radars located in Supersites 1 and 2. Supersite 3 was placed at Capvern, which is a commune located 4 km away from Lannemezan.

Moreover, two different aircraft were used to probe the boundary layer during the campaign: a Piper Aztec and a Sky Arrow. They overflew the campaign area taking measurements which could also be compared with other instruments' measurements. They flew at different levels, performing horizontal legs within and just above the CBL and in vertical spirals. These strategies were also
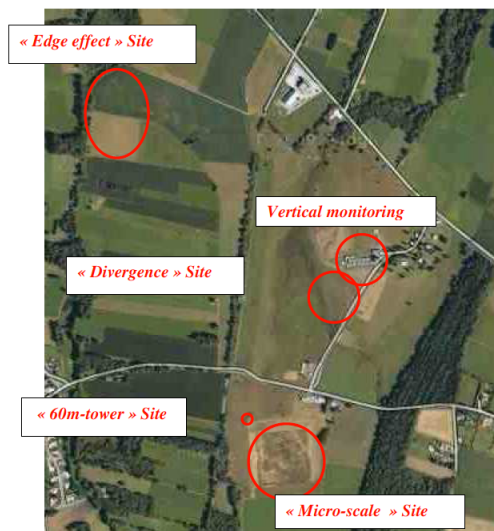
Figure 2.3: Aerial view of Supersite 1 showing the distribution of all the sites (vertical monitoring site, 60-m tower site, divergence site, edge effect site and micro-scale surface heterogeneity site). Courtesy of Marie Lothon.

combined with the flights of RPASs at lower levels. Repeated legs at the same height and on same axis by the same RPAS provided very interesting information about the evolution of turbulence along this leg.

Research centers which participated in the BLLAST campaign and their roles during the campaign are summarized in Table 2.1.

2.3.1 Continuous Observations

In the following sections, we summarize the in situ and remote sensing instruments deployed during BLLAST over the 3 Supersites for a continuous observation of the atmosphere. We describe here the deployment of those instruments for the observation of the surface layer processes, boundary-layer profiling and sky monitoring. Table 2.2 shows the location of all the continuous observation instruments.

2.3.1.1 Turbulence and mean meteorological parameters at the surface layer

In a 10×10 km^2 area, 9 masts, located over different vegetation coverages, were equipped with a total of 26 instruments recording data with 10 or 20 Hz frequency. They measured the three wind components and temperature. Some of them measured the specific humidity and the CO_2 mixing ratio. Table 2.3 describes the characteristics and variables measured by the different masts.

Table 2.1: List of BLLAST member centers, member numbers for each center and their role in the campaign

Center Name	City Country	Number of participants	Role
University of Utah	Salt Lake City, UT, USA	2	Surface oper.
NOAA	Boulder, CO, USA	1	Mesoscale model.
Technische Universitaet	Braunschweig, GE	2	Remotely Piloted Aircraft Systems (RPAS) oper.
LPCA	Dunkerque, FR	5	Aerosol lidar
Tübingen University	Tübingen, GE	5	RPAS oper.
Laboratoire d'Aérologie	Toulouse, FR	11	Coordination, computer hardware, UHF-VHF, LES, RS, aircraft, towers and field oper. and administration
Météo-France, GAME	Toulouse, FR	17	Ground oper. , forecast model., coordination model., Lidar, opera. radar, Frequent RS
SAFIRE	Toulouse, FR	5	Aircraft oper.
UPC-BarcelonaTech	Barcelona, SP	2	LES and MLM model.
OMP / SEDOO	Toulouse, FR	3	Data center
Météo-France, DIRSO/CDM65	Toulouse, FR	1	Forecast
University of Leeds	Leeds, UK	1	Field oper.
Univer. de les Illes Balears	Mallorca, SP	4	RPAS and Surface oper., mesoscale model.
ZHAW-UMARS	Zürich, CH	3	RPAS oper.
University of Notre Dame	Notre Dame, IN, USA	1	Surface oper.
University of Davis	Davis, CA, USA	1	Surface oper.
University of California	San Diego, CA, USA	2	USA IR camera
LMD, Ecole Polytechnique	Paris, FR	1	Doppler lidar
IBIMET	Firenze, IT	2	Aircraft oper.
Forschungszen trum Jülich	Jülich, GE	1	Surface
PMOD-WRC	Davos Dorf, CH	2	Radiation meas.
MAQ Wageningen Univer.	Wageningen, NE	9	Instrument., model. GABLS, surface model. and oper., radiation oper., scintillometer
University of Bergen	Bergen, NO	2	RPAS oper., ground oper.
Univer. Complutense Madrid	Madrid, SP	3	Micobarom.
ENAC	Toulouse, FR	1	RPAS Authorization Security

Table 2.2: Distribution of the continuous observation instruments in their Supersites.

Instrument	Supersite 1	Supersite 2	Supersite 3
60-m tower (5 levels)	X		
HR, LR wind			
HR, LR temperature			
HR, LR humidity			
HR, LR O3			
HR, LR CO2			
Radiation			
Soil moisture			
IR Camera			
Radiation Divergence tower (5 levels)	X		
10-m tower			
Skin flow tower (4 levels)	X		
HR wind			
HR temperature			
2-m towers (1 level)		X	
Soil moisture			
30-m tower		X	
HR, LR wind			
HR, LR temperature			
HR, LR humidity			
Radiation			
Surface temperature probes network	X	X	
VHF wind profiler	X		
UHF wind profiler	X	X	
Sodar	X		X
Aerosol Lidar	X	X	
Doppler Lidar	X		
Radiometer	X		
Scintillometry	X		
Ceilometry	X	X	
Full Sky Imagery	X		
Microbarometry	X		
Aerosols	X		
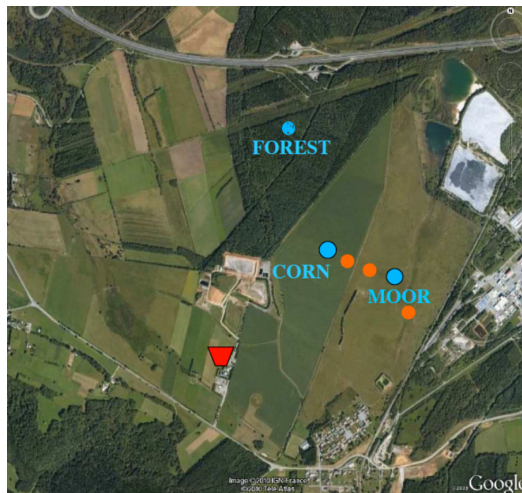
Figure 2.4: Aerial view of Supersite 2 showing the distribution of all the sites (forest site, corn site and moor site). Blue circles mark the EC surface station, orange circles tag the surface soil temperature sensors and the red trapezium point the remote sensing vertical monitoring (UHF). Courtesy of Marie Lothon.

They were installed over different terrains to observe the importance of heterogeneity, even though, they also had individual objectives. The corn, moor and forest sites were devoted to studying the impact of surface heterogeneities during the afternoon transition. The micro site's main focus was the small surface heterogeneities andthe 60-m tower was committed to measuring vertical profiles in and above the surface layer. The skin-flow's aim was to investigate the near-surface divergence of the sensible heat flux. At the edge site, three masts were installed over different land uses to validate a flux-footprint model (Boer et al., 2012). Figure 2.5 shows all the instruments measuring turbulence and mean meteorological parameters in the surface layer. Heat, momentum and CO_2 fluxes at the surface were estimated at all sites using a uniform processing method (De Coster and Pietersen, 2011).

Next to the skin flow tower, a 10-m mast was installed to analyze the atmospheric radiation. Its main objectives were to measure the radiation balance at the surface, the radiation divergence, and to examine its relative contribution to the heat budget.

Apart from the EC-stations used during the BLLAST field campaign, three micro barometers were deployed at Supersite 1 to analyze the surface layer. They were installed forming a triangular array of approximately 150 m and at 1 m height. The objective of these sensors was to study the small-scale static pressure fluctuations produced in the atmospheric boundary layer (Sastre et al., 2012; Román-Gascón et al., 2012).

A high-resolution IR camera was also installed on Supersite 1, mounted on

Table 2.3: List of EC-stations, vegetation cover, site latitude and longitude, height above the sea level and the properties measured during BLLAST campaign .

Site name	Land use	Latitude (N) Longitude (E)	Height ASL [m]	Variables measured
Corn (Site 2)	Corn	43° 05' 24 " 0° 21' 30"	645	Temperature, wind, H_2O, CO_2, pressure, radiation, soil temperature, soil humidity, soil heat flux
Moor (Site 2)	Mixed moor-like vegetation	43° 05' 24 " 0° 21'4 3"	641	Temperature, wind, H_2O, CO_2, pressure, radiation,soil temperature, soil humidity, soil heat flux
Micro (Site 1)	Grass and shrubs	43° 07' 26" 0° 21' 51"	601	Temperature, wind, H_2O, CO_2, pressure, radiation
60-m tower (Site 1)	Mixed	43° 07' 27" 0° 21' 45"	602	Temperature, wind, H_2O, CO_2, pressure, radiation
Forest (Site 2)	Douglas Spruce	43º 05' 34" 0º 21' 19"	620	Temperature,wind, H_2O CO_2 pressure
Skin flow (Site 1)	Grass	43° 07' 32" 0° 21' 57"	591±5	Temperature, wind
	Wheat, rye and peas	43° 07' 56" 0° 21' 37"	582	Temperature,wind, H_2O,CO_2, pressure, wet-bulb temperature, soil temperature, soil humidity, soil heat flux
Edge (Site 1)	Grass	43° 07' 52" 0° 21' 33"	581	Temperature,wind,H_2O,CO_2, pressure, wet-bulb temperature, soil temperature, soil humidity, soil heat flux
	Mixed	43° 07' 53" 0° 21' 35"	581	Temperature, wind, H_2O, CO_2, pressure
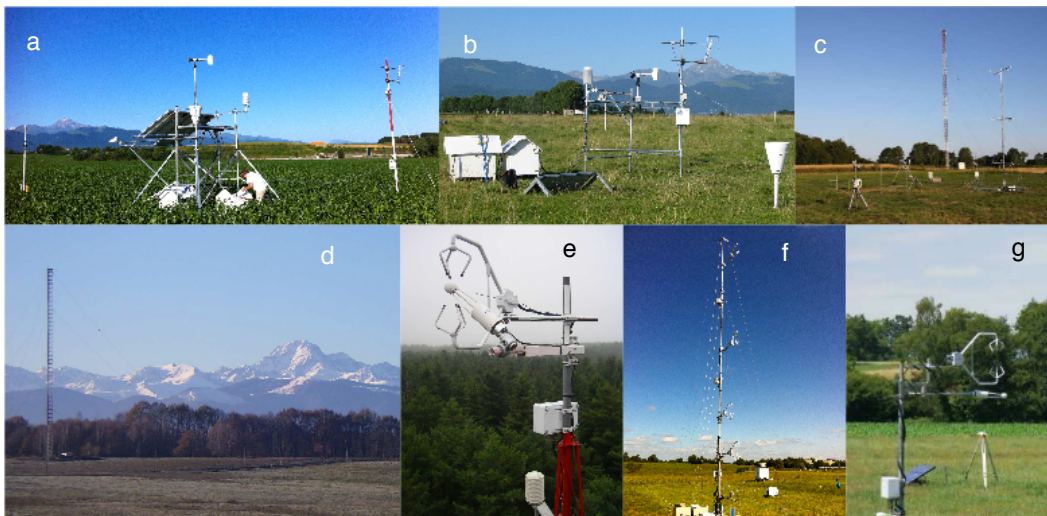
Figure 2.5: Instruments measuring the turbulence and mean meteorological parameters at the surface layer during BLLAST: (a) corn site, (b) moor site (c) microsite, (d) 60-m tower, (e) forest site, (f) skin flow site and (g) edge site.

the 60-m tower. At the beginning of the field campaign it was looking North (divergence site) and at the end South (microscale site) (Garai et al., 2013).

Finally, scintillometers were also deployed. They measured heat fluxes along the path which separates the emitter from the receiver. The first one was installed on the edge site at Supersite 1. The second one had a 3 km path from the top of the church of Campistrous to the roof of the Laboratoire d'Aerologie (LA). The last one was a large aperture scintillometer, and it had a 4 km path from the chimney of an industrial plant to the roof of the LA.

2.3.1.2 Boundary-layer profiling

During the BLLAST campaign, the atmospheric boundary layer was continuously probed by : wind profilers, doppler lidars and aerosol lidars (see Fig. 2.6).

At Supersite 1, the whole atmospheric column was covered by the combination of: a sodar, which measured wind direction and speed from 10 m to 300 m; a UHF profiler, which measured reflectivity, vertical and horizontal wind and dissipation of the turbulence from 200 m to 3000 m; and a VHF profiler, which measured reflectivity, vertical wind speed and horizontal wind speed from 1.5 km to 16 km. Additionally, the atmospheric circulation at the scale of the Plateau was estimated by a network of 3 profilers: a UHF at Supersite 1, a UHF at Supersite 2, and a sodar at Supersite 3.

The UHF wind profiler was also used to define the height of the boundary layer top inversion, or other strong vertical gradients in the atmosphere

(Angevine et al., 1994; Heo et al., 2003). The boundary layer depth measured by this instrument is defined as the height of maximum backscattered intensity.

Moreover, a Doppler lidar was also installed at Supersite 1 during the BLLAST experiment. It measured the vertical velocity of the wind at high temporal and vertical resolutions. It was used to study the structure of the thermals and to calculate the vertical velocity integral scales and the intensity of turbulence during the afternoon transition.

Finally, there were also two aerosol lidars at Supersite 1 and Supersite 2 to monitor the aerosol distribution.

2.3.1.3 Sky monitoring

To monitor the sky, we used a full sky camera located at Supersite 1, obtaining images of the entire sky and qualitatively monitoring the cloud cover. Moreover, there was also a ceilometer next to the camera to obtain cloud heights which do a profile every 15 s. This instrument used a laser diode at a wavelength of 905 nm to measure the height of cloud basesup about 7600 m (maximum range of the system) (see Fig. 2.7) (Haeffelin et al., 2012).

2.3.2 Intense Observational Periods

During the BLLAST campaign, 11 IOPs were defined with additional continuous measurements coming from manned aircraft, RPASs, tethered and frequent radio sounding balloons, and in situ aerosol measurements, as shown in Fig. 2.8.

2.3.2.1 Balloons

During BLLAST, three different types of balloons were used: standard radio soundings, frequent radio soundings and tethered balloons. Table 2.4 shows different characteristics of the sounding systems and the launching sites.

During IOPs, standard radio soundings were MODEM and GS-H, and were launched at least 4 times per day at 6:00, 12:00, 18:00, 00:00 UTC to obtain the structure of the troposphere during the diurnal cycle. Moreover, the University of Bonn also launched some standard radio soundings at Supersite 1 during the first IOPs (GRAW radiosondes). Simultaneous launches of 3 radio soundings from the three Supersites were used to estimate the sub-mesoscale divergence during some IOPs.

Frequent radio soundings were also used during BLLAST, but only at the afternoon transition. They were launched by Météo-France/GAME/GMEI, and they consisted of 2 balloons of different sizes attached to the same probe. Both balloons rose to 2 km height where the probe and the smaller balloon were separated from the larger balloon. The probe could be re-used because the smaller balloon had a parachute and the probe was protected. To recover the probe, a model predicted the landing area (Legain et al., 2013).

Finally, there were 3 tethered balloons operating during the late afternoon of IOP days, from 14:00 to 21:00 UTC. The balloon located at Supersite 1 was
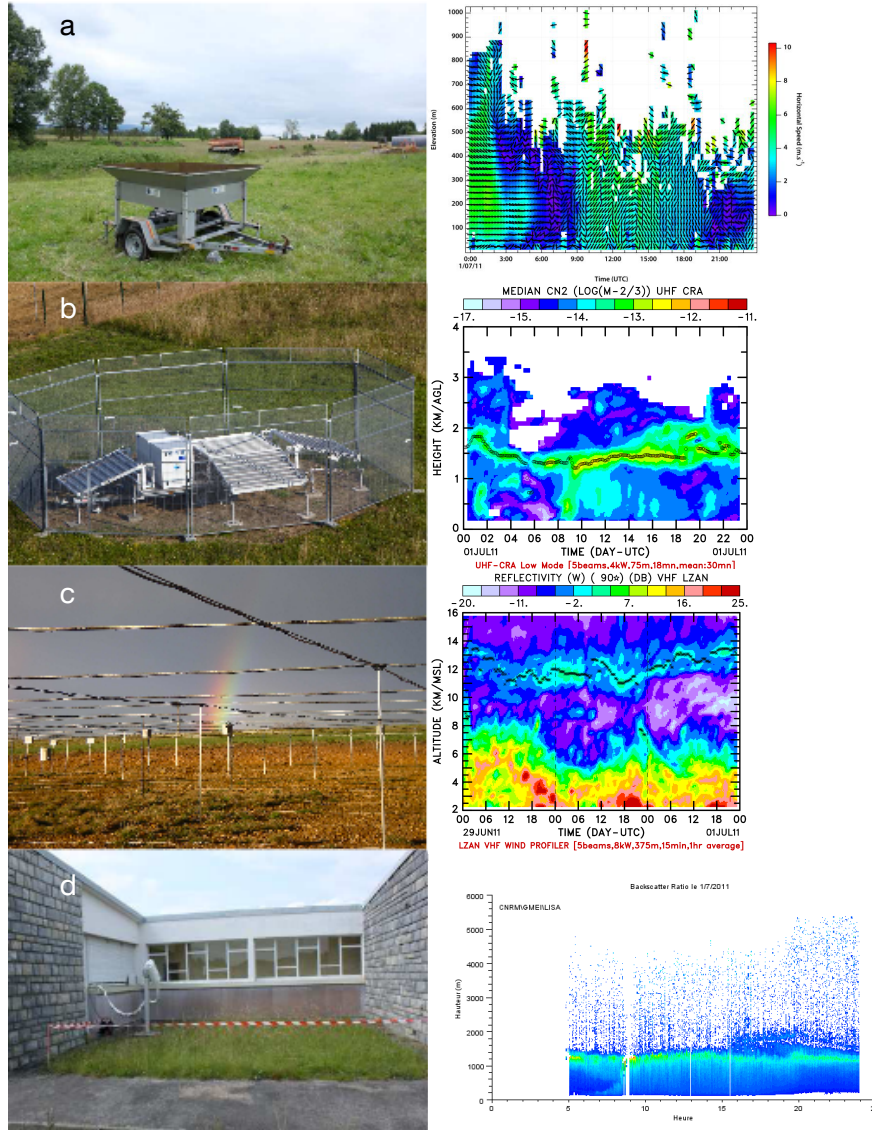
Figure 2.6: Measurements taken by the boundary layer profilers on 01 July 2011 of the BLLAST campaign: (a) Remetch Sodar PA2 at Supersite 3 (instrument and horizontal wind), (b) UHF (Ultra High Frequency) at Supersite 1 (instrument and reflectivity) (c) VHF (Very High Frequency) wind profiler at Supersite 1 (instrument and reflectivity), and (d) Aerosol lidar (instrument and backscatter ratio).
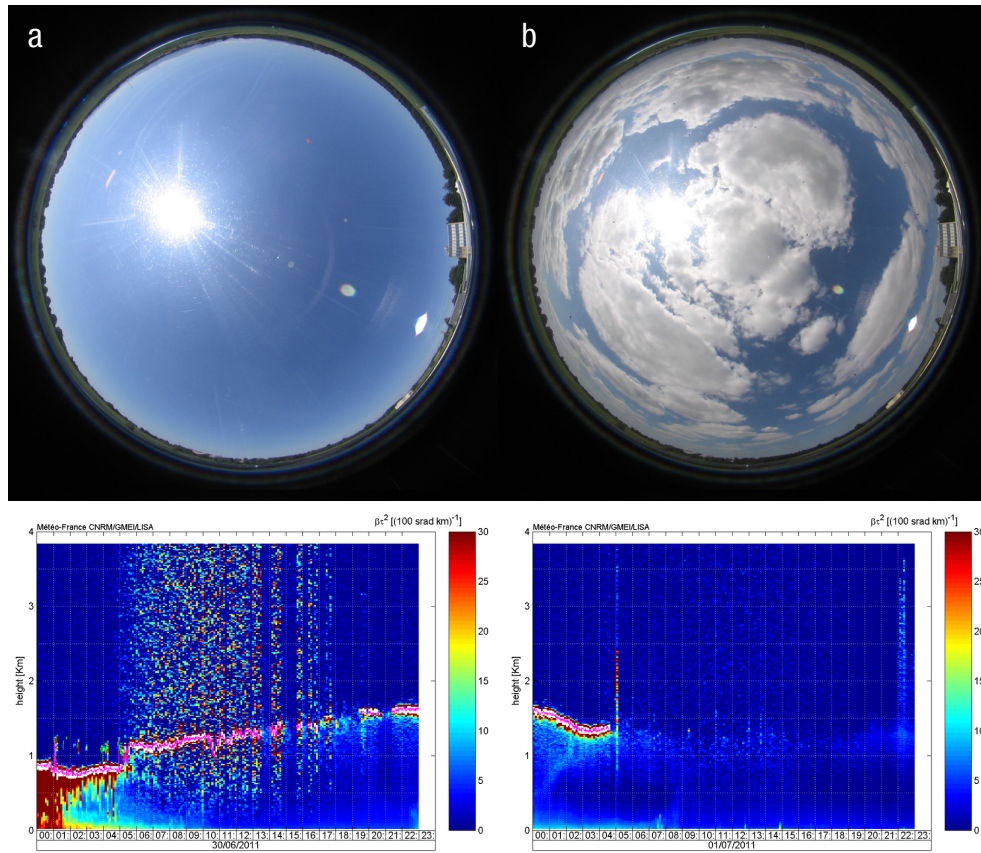
Figure 2.7: (Top) Sky picture obtained with the total sky camera at 14:00 UTC and (bottom) the backscatter from the ceilometer (a) 30 June 2011 and (b) 1 July 2011.
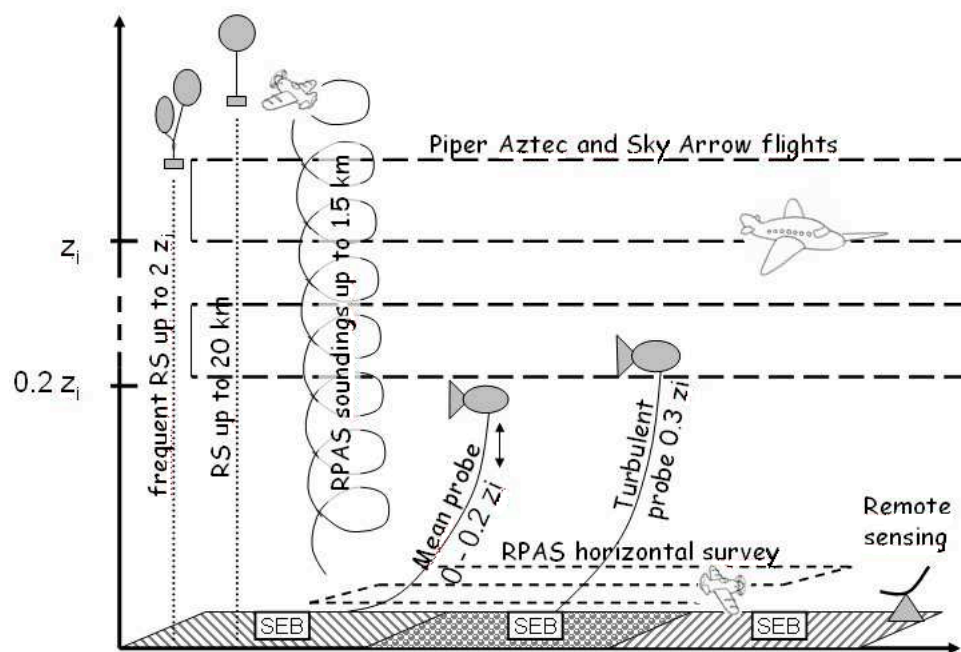
Figure 2.8: Illustration of the observing strategy during the Intensive Operational Period. RS = Radio sounding, RPAS = Remotely Piloted Aircraft System, SEB = Surface Energy Balance. Courtesy of Fabienne Lohou.

Table 2.4: Launching sites and characteristics of radio soundings and tethered balloons

	Site 1	Site 2
Radio soundings		
Standard radio soundings – max 20 km	x	
Frequent radio soundings – max 2 km		x
Tethered balloons		
Balloon 1 / 5 levels LR wind, temperature, humidity		x
Balloon 2 / 5 levels LR wind, temperature, humidity		x
Balloon 3 / 1 level HR wind, temperature, humidity	x	

equipped with one new developed turbulence probe. This probe was composed of SA, whose oscillation angles were measured by an inertial navigation system, and by of fine-wire (FW) in a radiation shield for air temperature measurements. The other two tethered balloons were located at Supersite 2 to study the role of terrain heterogeneity. Specifically, they were located over the maize field and the moor field. Depending on the IOP, the strategy consisted of leaving them fixed at a low height or moving them vertically.

2.3.2.2 Remotely piloted aircraft systems

Three teams used RPASs during the campaign. During BLLAST, a Temporary Restricted Airspace (TRA) which covered Supersites 1 and 2 at a vertical extent of 7500 ft was defined, but the height limitation could vary. For instance, when the manned aircraft were overflying the area of interest, depending on their lowest flight level, the RPASs could not usually fly over 400 ft. The area was a 2.25 km radius cylinder centered at *43° 6' 18" N, 0° 21' 6" E.*

The RPASs belonging to Tübingen and Braunschweig University were designed to fly in horizontal legs, allowing the computation of means and fluctuations of temperature, humidity and wind, from which estimation of turbulent covariances could be obtained (Van den Kroonenberg et al., 2012; Martin et al., 2011). However, they could only do few flights. On the other hand, the RPASs from the University of Bergen were smaller and more suited to make soundings up to the top of the TRA within 15-30 min. Additionally, these last RPASs made a dense horizontal exploration 60 m above ground, with measurements of the surface temperature (Reuder et al., 2012).

2.3.2.3 Manned Aircraft

During the BLLAST campaign two aircraft were used: the French Piper Aztec from Service des Avions Francais Instrumentés pour la Recherche en Environnement (SAFIRE) (Saïd et al., 2005), and the Italian Sky Arrow from Istituto di Biometeorologia (Ibimet) and Istituto per i Sistemi Agricoli e Forestali del

Mediterraneo (Isafom) (Gioli et al., 2009; Zulueta et al., 2013). During the campaign, these two aircraft performed their flights in the middle to late afternoon. The measurements from the aircraft could be compared with the ones obtained by the ground-based instruments (flux stations and remote sensing devices), and they performed coordinated flights with the tethered balloons and RPASs.

Along its flight track, the Piper Aztec and Sky Arrow were able to measure pressure, temperature, moisture, CO_2 concentration and 3-D wind with a spatial resolution of a few meters (see central image in Fig. 2.9). Their endurance was 2.5 hours. The Piper Aztec flew at 70 m s^{-1} and the Sky Arrow at 40 m s^{-1}. The Piper Aztec participated in the campaign from June 14 to July 8, while, the Sky Arrow participated in the campaign from June 14 to June 26.

The flight strategy were generally based on two strategies: to fly in horizontal planes and to perform spiral profiles. The levels of the horizontal runs were often dependent on the thickness of the boundary layer, which in general was determined from a vertical sounding at the beginning of the flight and the information given from the ground before take off (UHF wind profiler, radio soundings, ceilometer). Figure 2.9 shows two examples of the flight schedules for 19 June and 1 July 2011 (lateral images). In the flight strategy on 19 June 2011, both aircraft simultaneously flew at 13:30 and 16:45 UTC followed a cross pattern from east-west and north-south at two different altitudes, Piper Aztec at 800 ft and Sky Arrow at 700 ft. The flight strategy of 1 July 2011 was simpler, Sky Arrow was fling in horizontal legs from east-west and vice verse at 4 different altitudes (800 ft, $0.4z_1$, $0.6z_1$ and $0.8z_1$) and doing vertical profiles at the western end of the legs.

2.4 General description of IOPs

The most favorable situations for analyzing the evolution of the CBL during the afternoon transition corresponded to either anticyclonic or dry post-frontal conditions. In the first atmospheric conditions, the low troposphere was governed by the mountain-valley flows, with a northeasterly flow over the Plateau during daytime turning to south-west during nighttime. The CBL was either clear, or with few cumulus clouds. Post-frontal conditions corresponded to northwesterly winds that could be modified by the mountain-valley circulation. On these days, some cumulus clouds appeared.

During IOPs, the wind at the surface was generally weak. Surface sensible heat flux varied in relation with the surface characteristics between 100 W m^{-2} at midday over grass and moor to 400 W m^{-2} over the forest. Figure 2.10 shows the temporal evolution of the measured surface heat flux over different land uses during all the IOPs of the campaign. The latent heat fluxes were much more consistent between the various surfaces, reaching around 350 W m^{-2} at midday for all IOPs, which can be related with previous rainy periods in May and early June. The boundary-layer depth was usually around 1000 m, and it did not reach more than 1400 m during the campaign. The morning growth rate was quite variable from day to day.
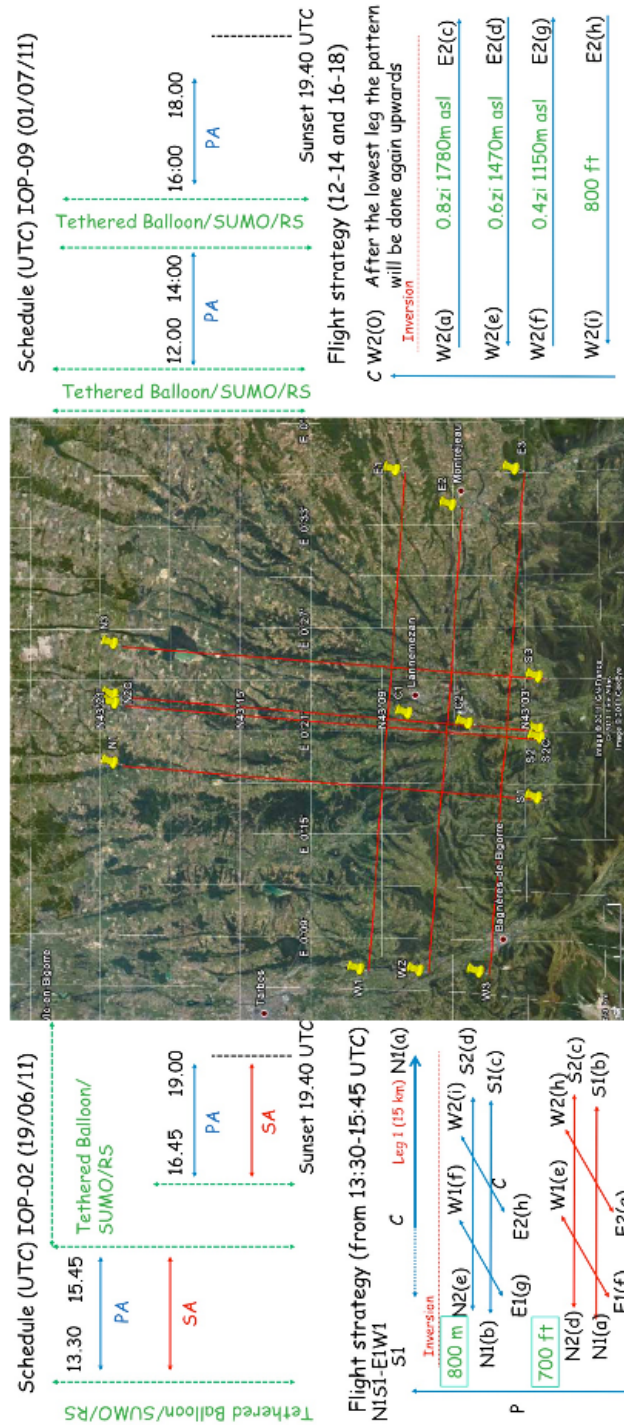
Figure 2.9: Flight schedule and flight plan of 19 June of 2011 (left) and 1 July 2011 (right) and flight path following during BLLAST campaign. Courtesy of D. Pino and J. Vilà-Guerau de Arellano.
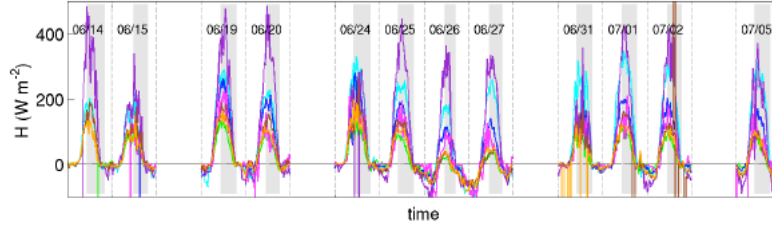
Figure 2.10: Temporal evolution fo the surface sensible heat flux measured over different land usesduring all IOPs of the BLLAST campaign. Courtesy of Marie Lothon.
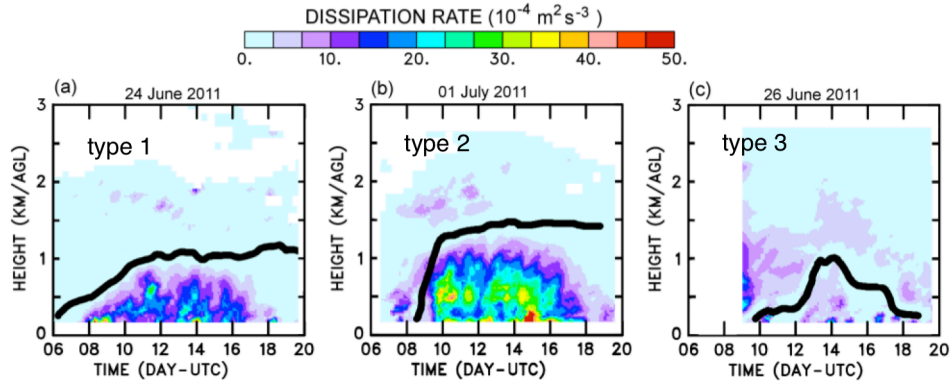

Figure 2.11: Three observed patterns of the evolution of the boundary-layer depth measured by UHF at Supersite 1. Courtesy of Marie Lothon.

Analyzing the observed z_1 , we deduce three different patterns of the evolution of the boundary-layer inversion from the local maximum of the refractive index coefficient measured by the UHF wind profiler (See Fig. 2.11). The first z_1 evolution consisted of a smooth increase in the height of the CBL from morning until midday. In these IOPs, z_1 reach values close to 1000 m. The second type of BL development showed an abrupt increase in the boundary-layer depth during the morning, reaching higher values of z_1 up to around 1200-1400 m and becoming approximately constant the rest of the day. Finally, the last boundary-layer evolution observed consisted of a steep increase and decrease in the boundary-layer depth.

In the following subsection, we describe the meteorological characteristics of each IOP. The analysis of the local meteorological conditions is developed whenever possible, with the information obtained from the standard radio soundings launched from LA around 12:00, 18:00 and 00:00 UTC.

IOP 1 (15 June 2011)

During this IOP, a high-pressure system was located over the area of the campaign. However, a large low-pressure system was approaching from the northeast. This low pressure-system arrived over the Pyrenees region the following day, 16 June 2011, and meteorological conditions became unsuitable for performing an IOP (see Fig. 2.12a).

The evolution of the boundary-layer depth from this IOP showed an intermediate growth rate and slightly descending summit inversion during the LAT (see Fig. 2.12b). This can be included in type 1 shown in Fig. 2.11.

During this IOP, standard radio soundings were not launched during the afternoon transition; the only one was launche dat 11:15 UTC. On the other hand, we used frequent radio soundings at 16:47 and 19:05 UTC to analyze the local meteorological conditions during the afternoon.

IOP 1 had clear skies with short partially clouded periods (not shown). The potential temperature was around 300 K at 11:15 UTC, with variation lower than 2 K from 16:47 to 19:05 UTC. Humidity was relatively high, 14 g kg^{-1} at 11:15 and 16:47 UTC, with a variation of 2 g kg^{-1} during the afternoon (19:05 UTC). The wind was very light close to the ground and it increased to approximately 2 m s^{-1} inside the boundary layer from the time of the first to last radio soundings being launched. In the free atmosphere, the wind speed increased to 8 m s^{-1} in all radio soundings analyzed. The wind pattern was clearly marked by the mountain-valley flow. Around 11:15 UTC, the winds came from the north-east and turned to north-west in the afternoon (19:05 UTC). All variables were constant in the free atmosphere from 11:15 to 19:05 UTC (see Figs. 2.12c, d, e and f).

IOP 2 (19 June 2011)

This was the first day of an anticyclonic period caused by a high-pressure system extended from the Atlantic Ocean. Therefore, clear skies were observed during the whole day (not shown). However, a large low-pressure system was approaching from central Europe (See Fig. 2.13a).

The evolution of the boundary-layer depth in IOP 2 presented a rapid growth during the morning, with leveling inversion during the afternoon transition (see Fig. 2.13b). This can be included in type 2 shown in Fig. 2.11. This leveling inversion can also be observed in the analysis of radio sounding measurements (see Fig. 2.13c).

The potential temperature was lower than the previous IOP. At 11:15 UTC, potential temperature was 293 K. During late the afternoon, at 17:43 UTC, it increased 4 K. During the night, a stable boundary layer was observed and the potential temperature close to the ground was 291 K. The humidity evolved from 5.5 g kg^{-1} at 11:15 UTC to 7.5 g kg^{-1} at 22:54 UTC. Wind conditions were similar to the previous IOP. Wind speed was really low inside the boundary layer, below 4 m s^{-1}, and wind speed in the free atmosphere was higher, approximately 15 m s^{-1}, producing a marked shear in the inversion zone from

11:15 to 22:54 UTC. Wind direction from 11:15 to 17:43 UTC was north-west turning to south-east at night (22:45 UTC). All variables were well-mixed in the free atmosphere from 11:15 to 22:45 UTC (see Figs. 2.13c, d, e and f).

IOP 3 (20 June 2011)

In general, meteorological conditions were really similar to the previous day with a high-pressure system covering the area of Lannemezan. Although the large low-pressure system over central Europe was moving away, a new one was approaching from the west the British Islands (see Fig. 2.14a). This low pressure system caused a three days period when the weather conditions were not suitable for the objectives of the campaign.

The evolution of z_1 on IOP 3 presented an intermediate growth rate, reaching values of around 1100 m during midday (see Fig. 2.14b). This can be included in type 1 shown in Fig. 2.11. The vertical profile of potential temperature clearly shows this continuous increase in the boundary-layer depth during the day (see Fig. 2.14c).

In IOP 3, potential temperature increased from 300 K at 11:01 UTC to nearly 303 K at 16:59 UTC. Moreover, during nighttime, when a stable boundary layer was observed, the potential temperature near the ground descended to 295 K at 23:04 UTC. During daytime, the humidity was more or less constant, around 8 g kg^{-1} at 11:01 and 16:59 UTC, increasing to 12 g kg^{-1} at nighttime (23:04 UTC). Wind speed at the ground was higher at 11:01 UTC (close to 5 m s^{-1}) than during the afternoon, which decreased to 3 m s^{-1} (at 16:59 UTC). As the day progressed, it decreased more to values close to 2 m s^{-1} at 23:04 UTC. Wind direction turned from north-east to south-west from 16:59 to 23:04 UTC (see Figs. 2.14c, d, e and f).

IOP 4 (24 June 2011)

A large high-pressure system was covering the western part of Europe and the north of Africa (see Fig. 2.15a).

The evolution of the boundary-layer depth had an intermediate growth rate, reaching values of z_1 lower than the previous IOP of approximately 1000 m at midday. Moreover, the boundary-layer depth slightly decreased during the afternoon transition (see Fig. 2.15b). This is also shown in the vertical profile of potential temperature (see Fig. 2.15c). This evolution of the boundary-layer depth can be included in type 1 shown in Fig. 2.11.

In IOP 4, some clouds appeared during the morning, moving to the east, but the sky cleared up during the day (not shown). Potential temperature was lower from the previous IOP, evolving from 290 to 295 K from 10:52 to 16:40 UTC. At nighttime (23:12 UTC), the potential temperature near the surface descended to 288 K. What is more, the humidity was constant from 10:52 to 23:12 UTC, close to 6 g kg^{-1}, showing a deep shear in the inversion area. In relation with wind conditions, the UHF measured a very strong inversion (with a large wind-shear) at approximately 1.5 km (not shown), which can also be

observed in the vertical profile of wind speed shown in Fig. 2.15c. As the day progressed, the wind speed increased from 2 m s^{-1} at 10:52 UTC to 3 m s^{-1} at 16:40 UTC. At nighttime (23:12 UTC), it continued increasing, but it was also light at under 4 m s^{-1}. The wind direction, as in the previous IOP, turned from east to south-west from 16:40 to 23:12 UTC (see Figs. 2.15c, d, e and f).

IOP 5 (25 June 2011)

The synoptical conditions were similar to the previous day, with a large high-pressure system expanding toward Eastern Europe from Western Europe and North Africa (see Fig. 2.16a).

The evolution of z_1 from IOP 5 was very smooth, as the growth rate was really low, creating a really thin layer which reached values of just around 600 m during midday (see Fig. 2.16b). Despite this, it can be included in type 1 shown in Fig. 2.11.

Potential temperature increased faster and to higher values than the previous day, from 298 K at 11:00 UTC to 303 K at 17:00 UTC. When the stable boundary layer was well developed at 23:00 UTC, the potential temperature decreased to 296 K. Humidity from 11:00 to 17:00 UTC was constant at 6 g kg^{-1}, but at nighttime (23:00 UTC) it increased to 9 g kg^{-1} in the stable boundary layer. Wind speed during daytime was higher than previous IOPs and it increased homogeneously from 3 m s^{-1} at 11:00 UTC to 7 m s^{-1} at 23:00 UTC. Wind direction was constant to the east inside the boundary layer and to the west in the free atmosphere from the time of the first to the last radio sounding (see Figs. 2.16c, d, e and f).

IOP 6 (26 June 2011)

The synoptical conditions started to change from the previous IOP; the large high-pressure system covering Europe began to be affected by a low-pressure system that was approaching from the western coast of the Iberian Peninsula (see Fig. 2.17a).

The evolution of the boundary-layer depth consisted of a slow growth in the boundary layer during the morning, and a collapse of the inversion during the afternoon transition, reaching maximum values of below 700 m (see Fig. 2.17b). This day belongs to type 3 shown in Fig. 2.11.

IOP 6 was not a completely clear day; there were some high level clouds until noon, and some precipitation in the mountains. Moreover, convective clouds appeared in the afternoon over the mountains (not shown). Nonetheless, IOP 6 had warmer potential temperatures, even at 11:00 UTC (307 K) or at 17:00 UTC (308 K), which, among other explanations, could be related to a shallow boundary layer. Humidity evolved from 7 g kg^{-1} at 11:00 UTC to 10 g kg^{-1} at 17:00 UTC, but it maintained the values during nighttime (23:00 UTC). In contrast, wind speed was constant from 11:00 to 17:00 UTC, at values close to 4 m s^{-1}, and it increased to 9 m s^{-1} at 23:00 UTC within the boundary

layer. Wind direction evolved from east at 17:00 UTC to south at 23:00 UTC (see Figs. 2.17c, d, e and f).

IOP 7 (27 June 2011)

This was the last of 4 consecutive days with suitable meteorological conditions. A low-pressure system was covering the Iberian Peninsula which caused a two days period when the weather conditions were not suitable for IOPs, while a high-pressure system was moving to Central Europe (see Fig. 2.18a).

The evolution of z_1 from IOP 7, as in the previous IOP, was really smooth and the boundary-layer inversion collapsed from a rather shallow BL of less than 500 m at 17:00 UTC (see Fig. 2.18b) also shown in the vertical profile of potential temperature (see Fig. 2.18c). This evolution was also included in type 3 shown in Fig. 2.11.

The evolution of the potential temperature was similar to the previous IOP, with the high potential temperatures of close to 308 K during daytime at 11:00 and 17:00 UTC. However, at 23:00 UTC the potential temperature decreased rapidly to 300 K due to a cold front which was approaching from the British Islands. The humidity was higher than the previous day, due to a prolongated warm period. At 11:00 and 17:00 UTC, humidity was 9 g kg^{-1}, and at 23:00 UTC it increased to 14 g kg^{-1} . Wind speed increased during the day from 4 m s^{-1} at 11:00 UTC to 6 m s^{-1} at 23:00 UTC. Wind direction, as on previous days, moved from north at 11:00 UTC to east at 17:00 to west at 23:00 UTC (see Figs. 2.18c, d, e and f).

IOP 8 (30 June 2011)

This was the first of three consecutive IOPs. A large high-pressure system was located over the area of the campaign, which covered most of Europe and North Africa (see Fig. 2.19a).

The evolution of the boundary-layer depth was characterized by a large growth rate during the morning and z_1 being constant during the afternoon transition (see Fig. 2.19a). This kind of evolution is close to those described in type 1 (see Fig. 2.11).

During IOP 8, the sky was covered with low clouds, but it cleared slowly because the clouds became thinner in the afternoon (not shown). After a period with weather conditions not suitable for the objectives of the campaign, the potential temperature did not reach high values; it was around 292 K at 11:00 UTC and increased to 296 K at 17:00 UTC, then decreased to lower values at night (23:00 UTC). The humidity was constant during daytime, around 6 g kg^{-1} from 11:00 to 17:00 UTC, and it slightly increased to 8 g kg^{-1} at 23:00 UTC . Wind speed did not have large variation from 11:00 to 17:00 UTC, with low wind speed blowing within the boundary layer at 3 m s^{-1}. At 23:00 UTC, the wind speed increased slightly. There was a really marked shear with an

inversion jump of approximately 6 m s^{-1} observed in all the radio soundings. Wind direction was not constant, turning and fixing from north-east at 11:00 UTC to south-west at 17:00 UTC (see Figs. 2.19c, d, e and f).

IOP 9 (1 July 2011)

During this IOP, a large high-pressure system was located southwest of the British Islands. The influence of this high-pressure system extended towards the east (see Fig. 2.20a). Higher up in the atmosphere, at 500 hPa, a strong ridge extended over Southern Europe, causing a predominantly western flow in the region.

The evolution of z_1 presented faster growth during the morning, with leveling inversion during the afternoon transition (see Fig. 2.20b). This sharp increase in the boundary-layer depth can be explained by assuming the merge of the boundary layer with the residual layer, as will be explained in the next chapter. The evolution of z_1 can be included in type 2 (see Fig. 2.11). This leveling inversion is also shown in the vertical profiles of Fig. 2.20c.

Potential temperature was slightly higher than the previous day; specifically, it was 296 K at 11:00 UTC and 299 K at 17:00 UTC, decreasing to 297 K at 23:00 UTC. Humidity was again constant during IOP 9, although, it was slightly lower at around 5 g kg^{-1} from 11:00 UTC to 17:00 UTC. At 23:00 UTC the vertical profile of humidity is less clear, showing a pronounced curve inside the stable boundary layer. Wind speed was light, under 3 m s^{-1} observed in all radio soundings. Wind direction was north-east until 17:00 UTC and moved to north-west at 23:00 UTC (see Figs. 2.20c, d, e and f).

IOP 10 (2 July 2011)

During this IOP, the synoptical conditions changed and there was a low-pressure system located over the area (see Fig. 2.21a).

The evolution of the boundary-layer depth was charaterized by a moderate growth rate, and the height descended slightly during the afternoon transition (see Fig. 2.21b). Even though z_1 did not reach values as high as during the previous IOP, it reached approximately 1000 m. This evolution can be described as type 1 shown in Fig. 2.11.

The sky was clear, but some low stratocumulus started to appear at the end of the day (not shown).

During IOP 10, there were no standard radio soundings launched by LA at 23:00 UTC. Therefore, we show a GRAW radio sounding launched at 20:30 UTC. The potential temperature was higher than during the previous day, at 300 K at 11:00 UTC and 304 K at 17:00 UTC. The potential temperature at night descended to just 298 K at ground level. The humidity was similar to the previous day, close to 5.5 g kg^{-1} from 11:00 to 17:00 UTC, and increased to 7 g kg^{-1} at 23:00 UTC. The wind was weak in the boundary layer, around 2 m s^{-1} from 11:00 to 17:00 UTC, with a slight increase at 20:30 UTC. However, there was a really marked shear at z_1 of 10 m s^{-1} at 11:00 UTC. Wind direction was

mainly from the north-east in all the radio soundings (see Figs. 2.21c, d, e and f).

IOP 11 (5 July 2011)

This was the last IOP of the campaign. A high-pressure system was located over the area, expanding from the Scandinavia (see Fig. 2.22a).

The evolution of the boundary-layer depth from IOP 11 was characterized by a slow growth of the boundary-layer depth during the morning. Moreover, it collapsed during the afternoon, giving maximum values of the boundary-layer depth less than 1000 m (see Fig. 2.22b). This situation is considered in type 3 (see Fig. 2.11).

Due to the special evolution of the boundary-layer depth, the potential temperature also evolved in a particular way. At 11:00 UTC the potential temperature was around 300 K, with a clear inversion jump; but in the following radio sounding at 17:00 UTC, the potential temperature inversion jump was nearly unappreciable and the potential temperature increased to 302 K. The humidity was higher than the previous days, being 7 g kg^{-1} near the surface during the time of the three radio soundings. Wind speed clearly increased during daytime from 1.5 m s^{-1} at 11:00 UTC to nearly 5 m s^{-1} at 17:00 UTC. At 23:00 UTC, the wind speed was slightly higher, but the increment was less marked than during daytime. Wind direction turned from east at 11:00 UTC to west at 17:00 UTC (see Figs. 2.22c, d, e and f). The wind became strong later in the day, starting progressively around 1800 UTC above surface according to the UHF.
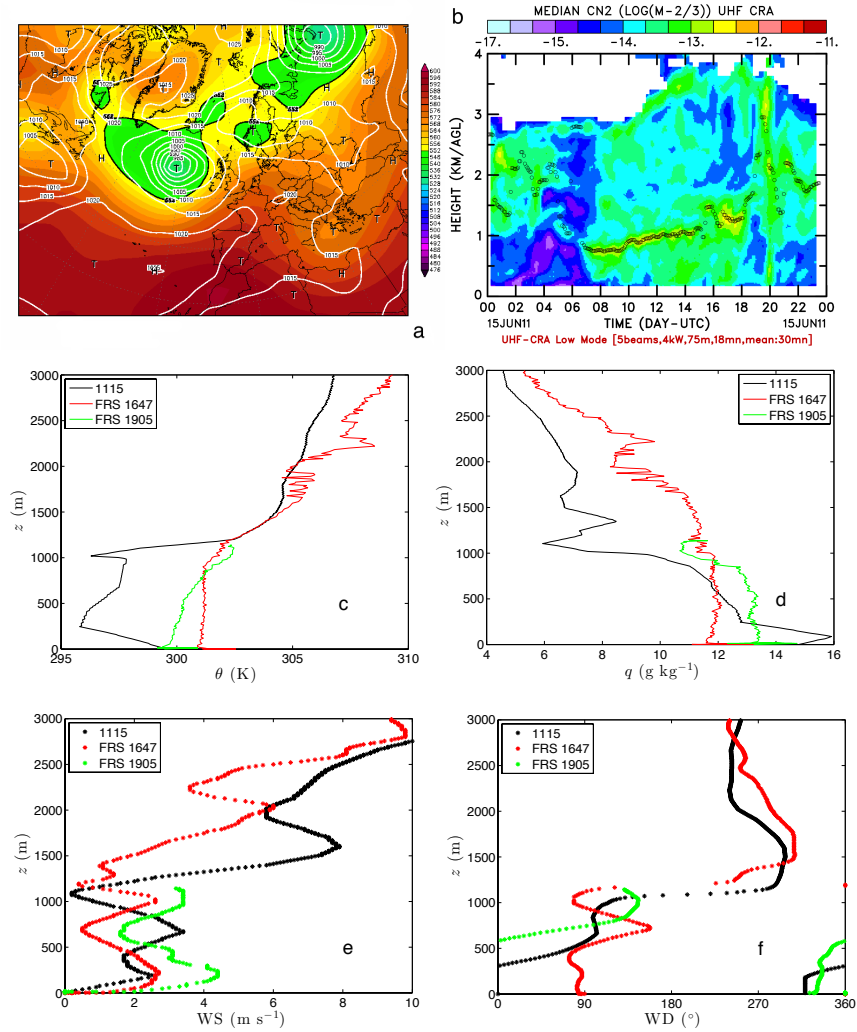
Figure 2.12: (a) 500hPa geopotential height (color contours) and surface pressure (white contours) obtained by NCEP Reanalysis, (b) temporal evolution of the boundary-layer depth measured by UHF located at Supersite 1 and vertical profiles of (c) potential temperature, (d) humidity, (e) wind speed and (f) wind direction measured by radio soundings during 15 June 2011.
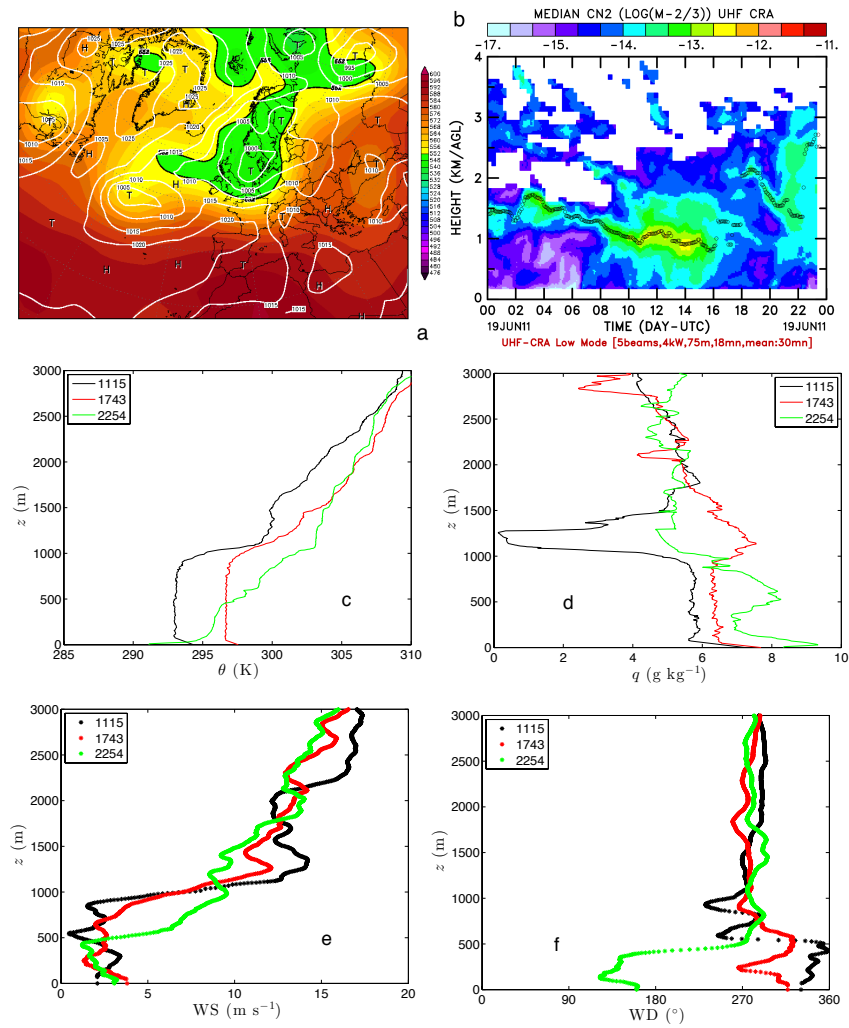
Figure 2.13: Same as Fig. 2.12 for 19 June 2011.
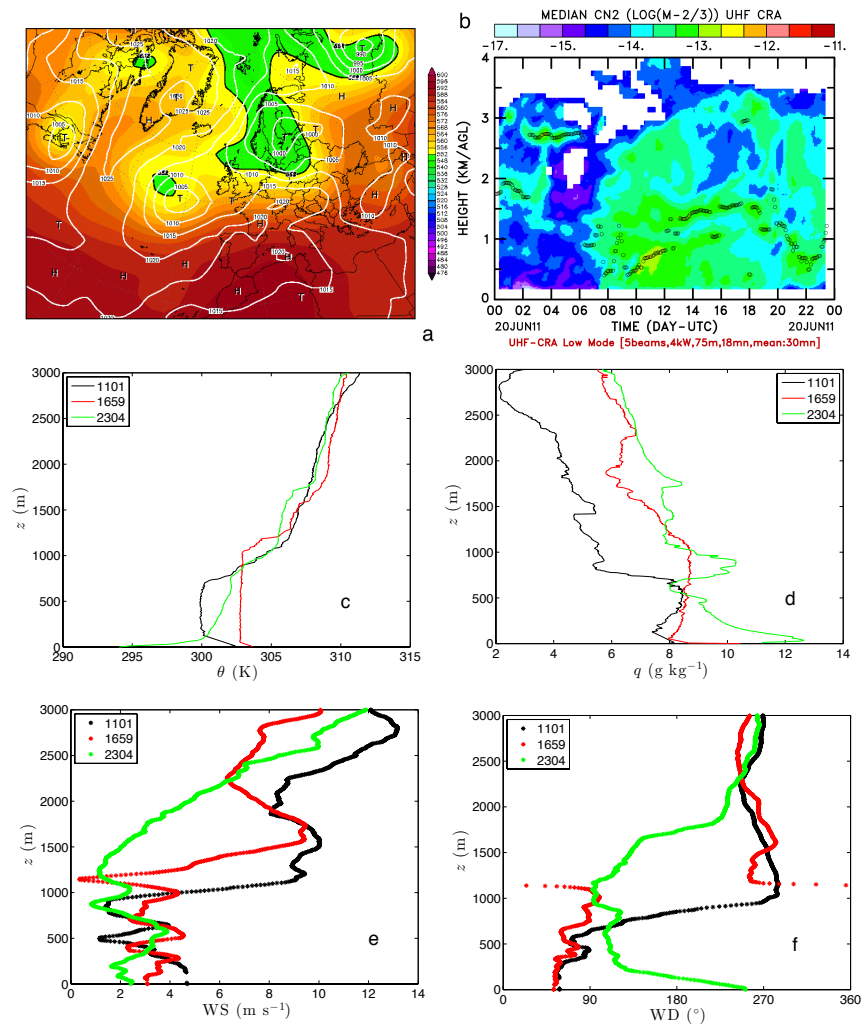
Figure 2.14: Same as Fig. 2.12 for 20 June 2011.
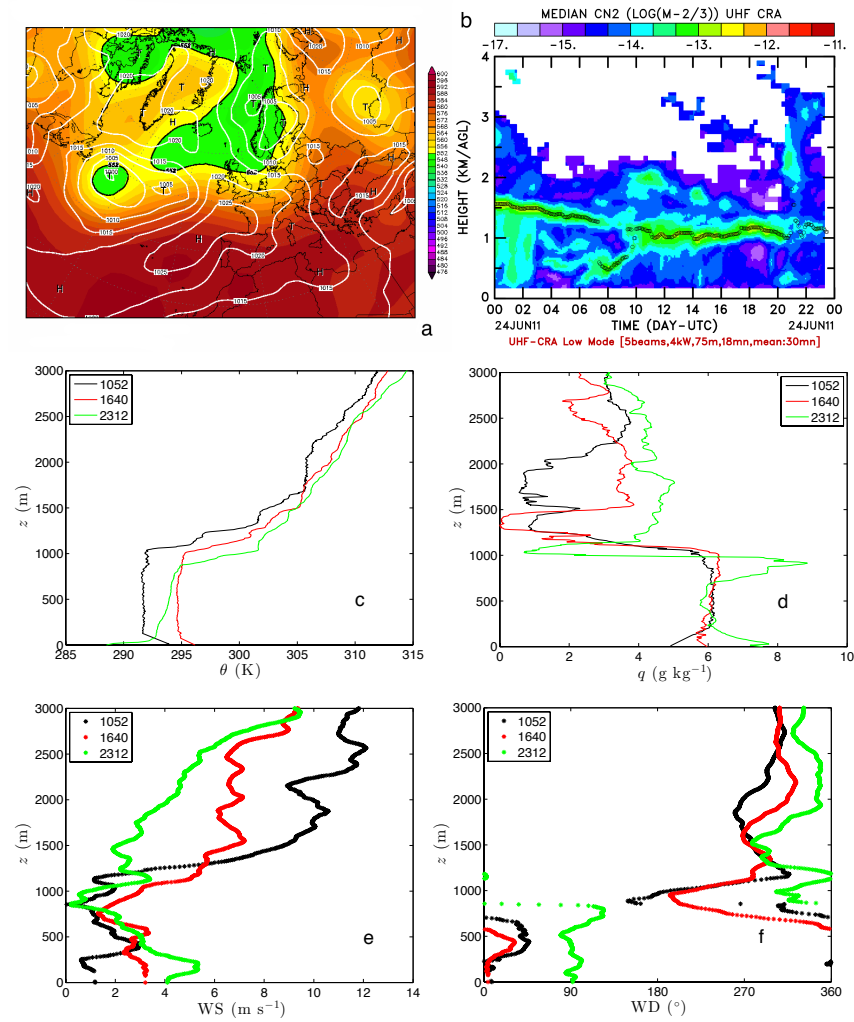
Figure 2.15: Same as Fig. 2.12 for 24 June 2011.
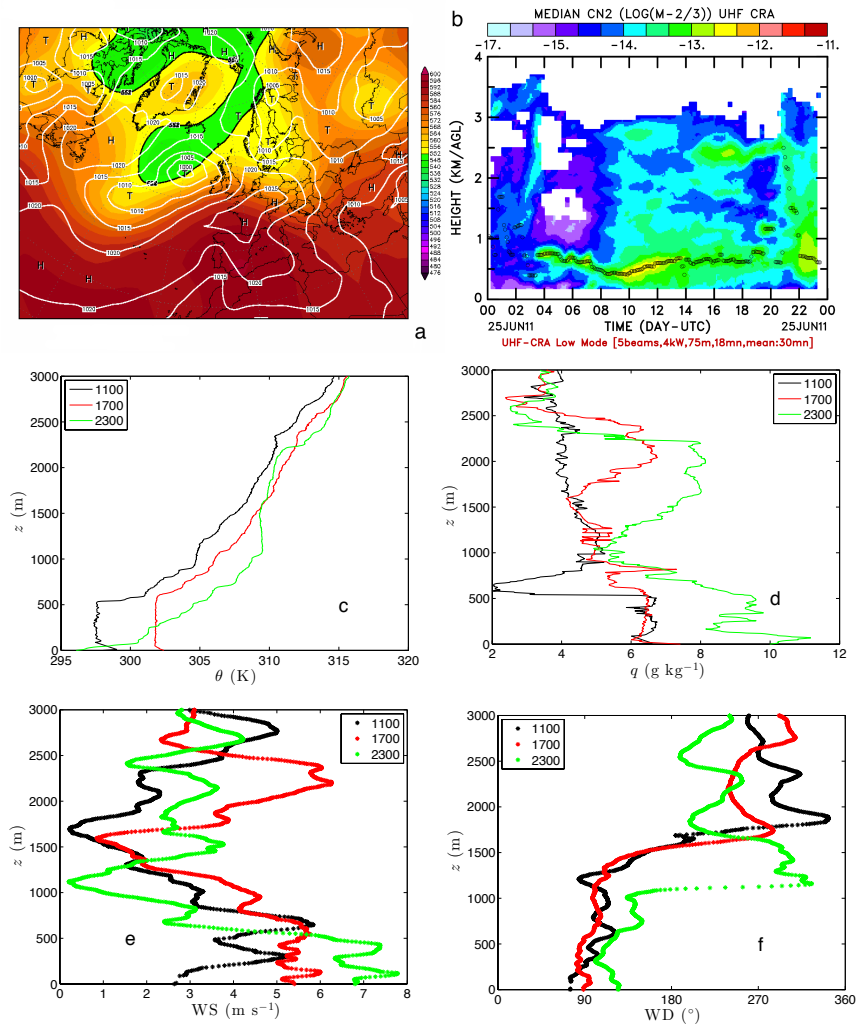
Figure 2.16: Same as Fig. 2.12 for 25 June 2011.
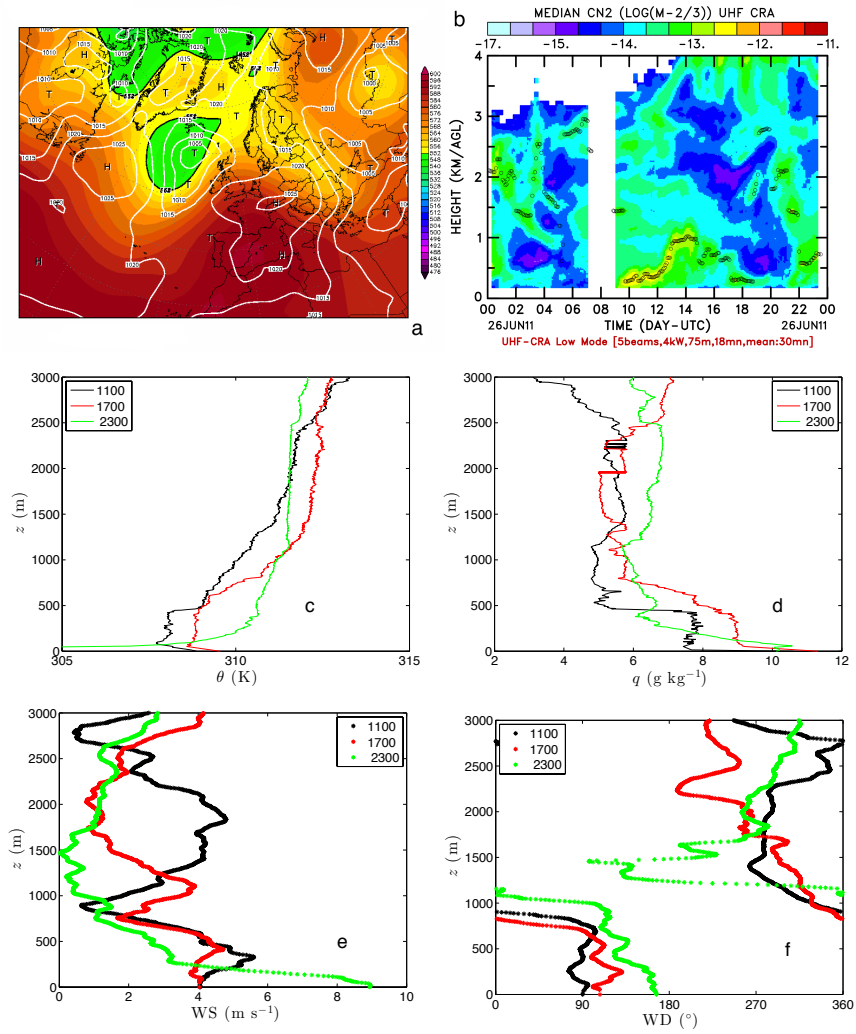
Figure 2.17: Same as Fig. 2.12 for 26 June 2011.
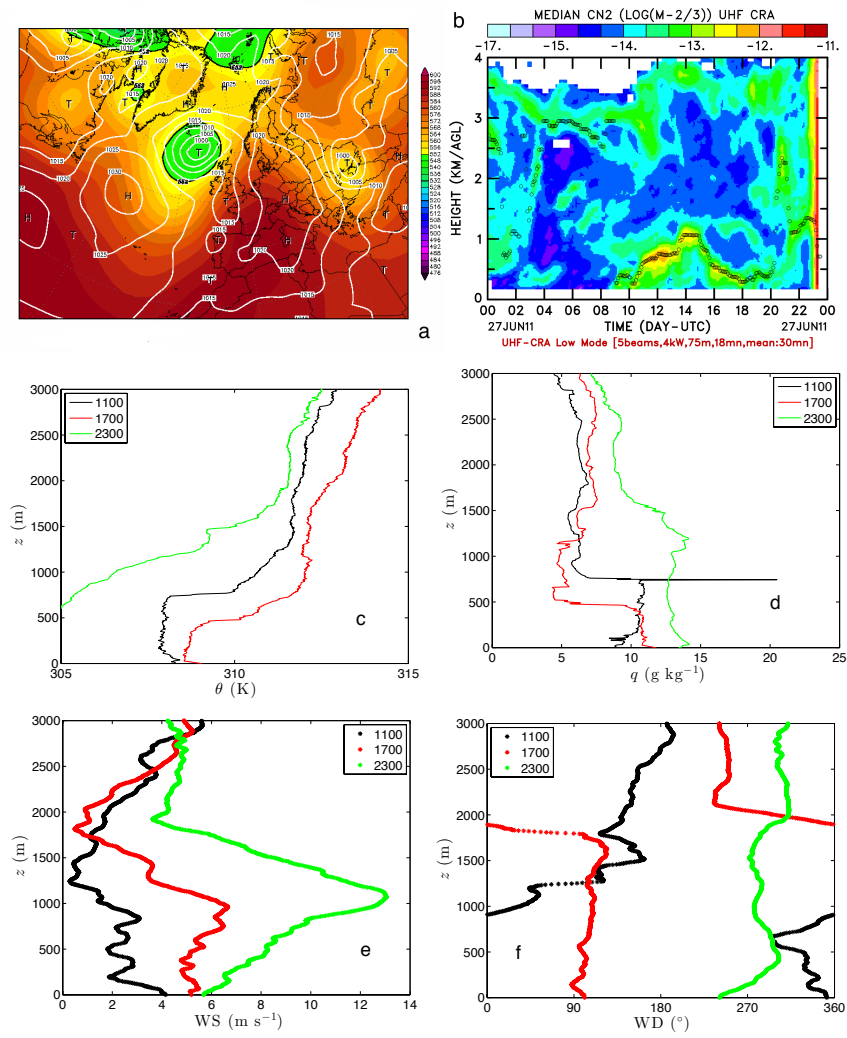
Figure 2.18: Same as Fig. 2.12 for 27 June 2011.
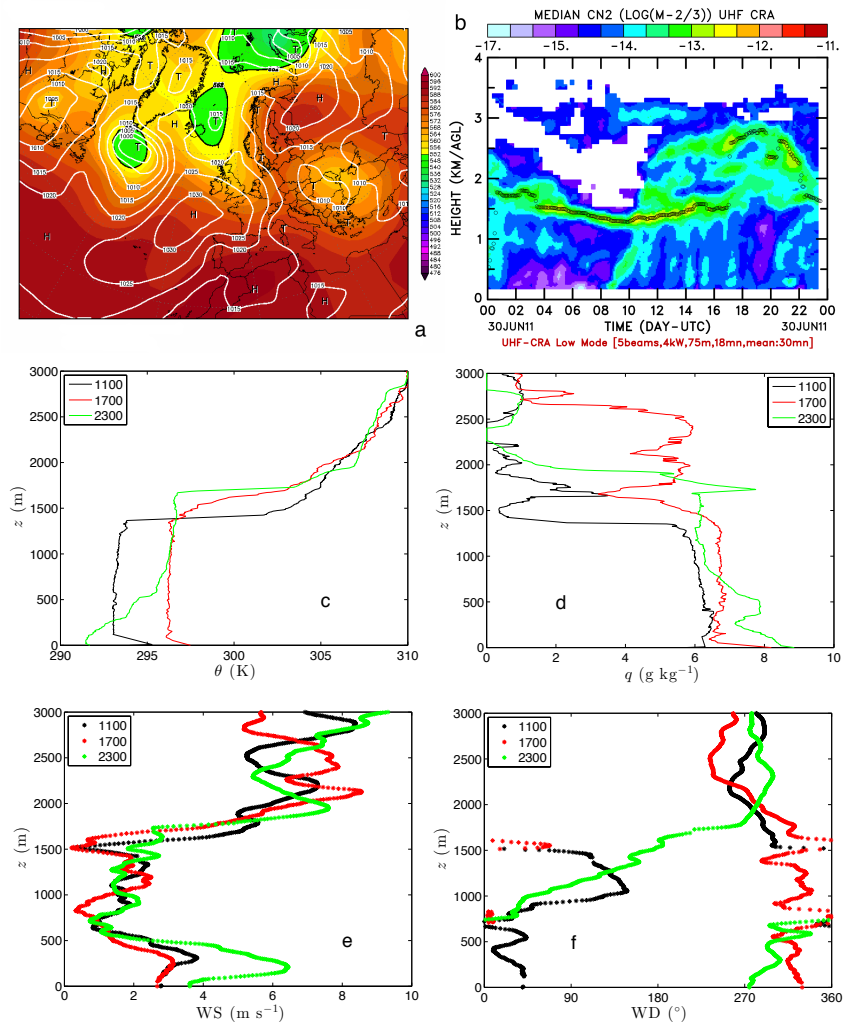
Figure 2.19: Same as Fig. 2.12 for 30 June 2011.
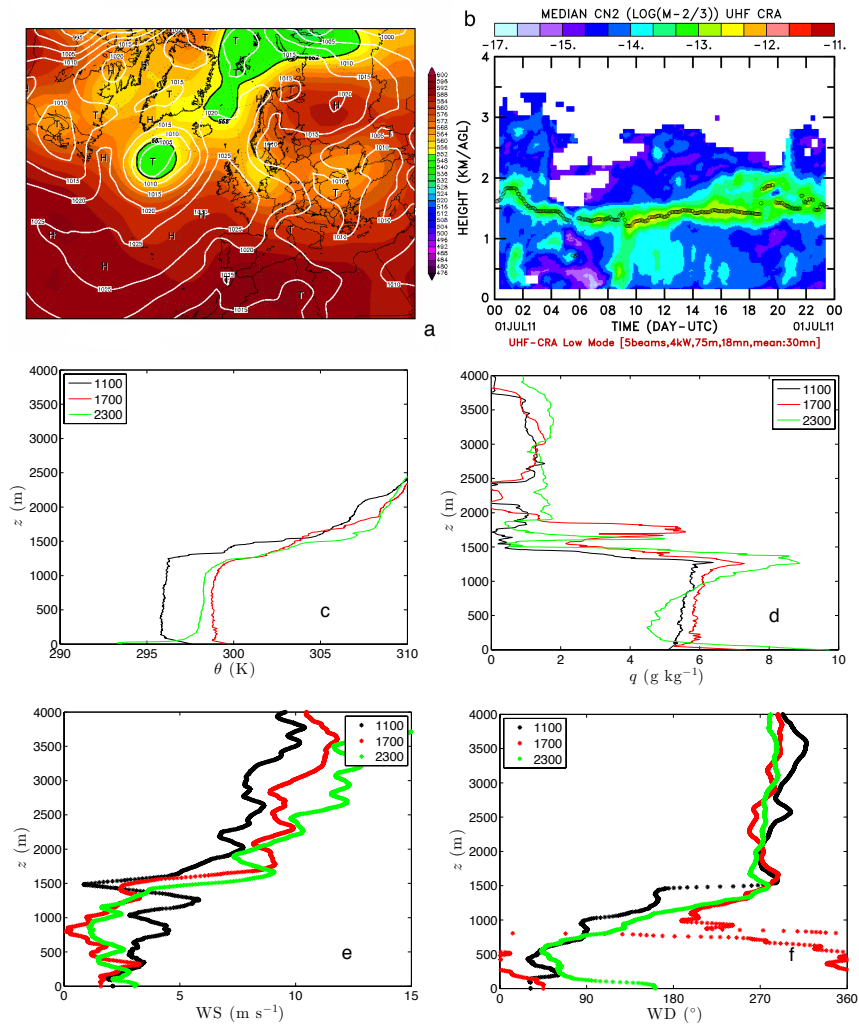
Figure 2.20: Same as Fig. 2.12 for 1 July 2011.
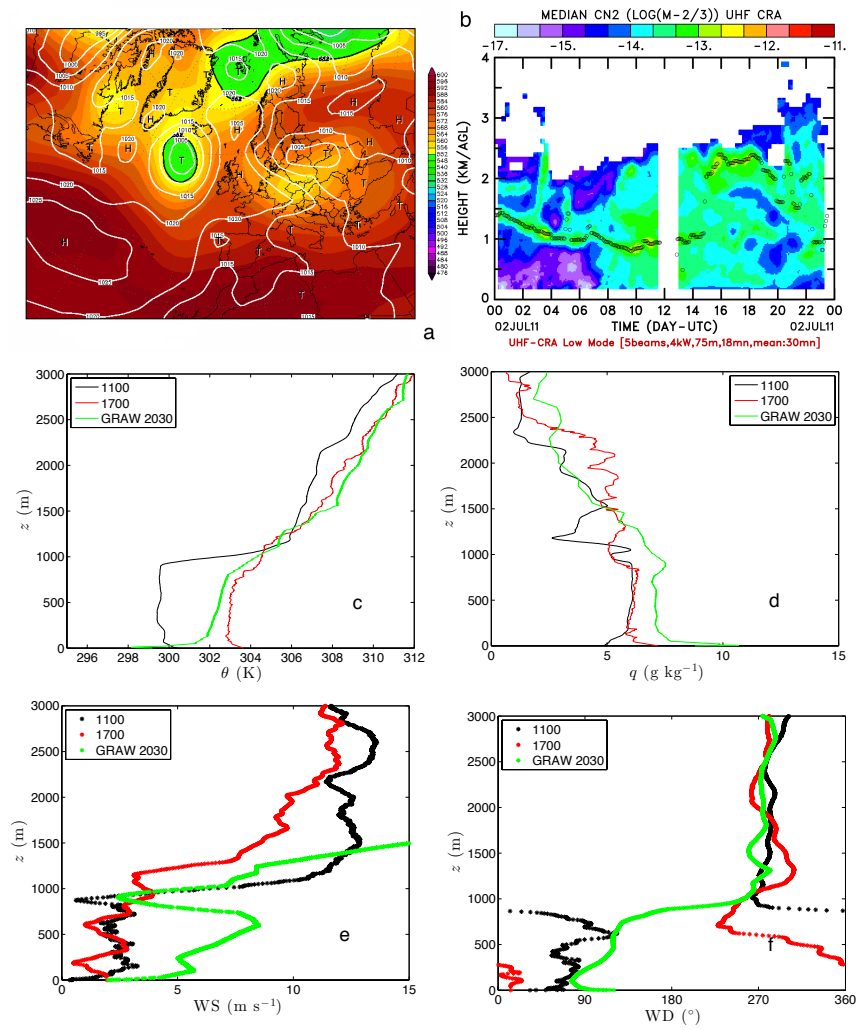
Figure 2.21: Same as Fig. 2.12 for 2 July 2011.
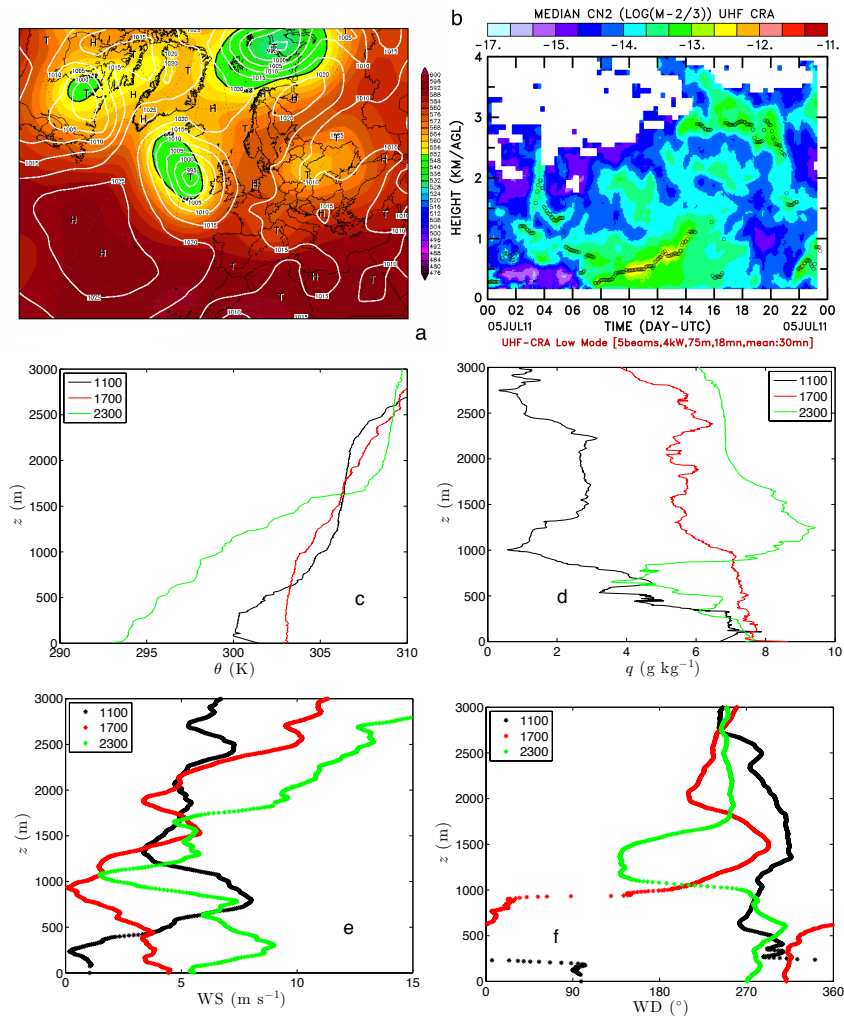
Figure 2.22: Same as Fig. 2.12 for 5 July 2011.

Chapter 3

Role of the residual layer and large–scale subsidence on the development and evolution of the convective boundary layer

[1]

Observations, mixed-layer theory and DALES are used to analyze the dynamics of the boundary layer during an intensive operational period (1 July 2011) of the Boundary-Layer Late Afternoon and Sunset Turbulence campaign. Continuous measurements were made by remote sensing, in situ instruments, and radio soundings, while other measurements were made by remotely piloted aircraft systems and two manned aircraft that probed the vertical structure and the temporal evolution of the boundary layer during the campaign. Some of these observations inspired the initial vertical profiles of potential temperature, specific humidity and wind, as well as the temporal evolution of the surface heat and moisture fluxes prescribed in the model runs.

This chapter is devoted to analyze the importance of the morning conditions in the subsequent evolution of the convective boundary layer. Specifically, the research focuses on the role played by the residual layer during the morning transition and by the large-scale subsidence on the evolution of the boundary layer. By using DALES, we show the importance of the dynamics of the boundary layer during the previous night in the development of the boundary layer in the morning. DALES numerical experiments that include the residual layer are capable of modeling the observed sudden increase of the boundary-layer depth during the

---

morning transition and the subsequent evolution of the boundary layer. These simulations show a large increase in the entrainment buoyancy flux when the residual layer is incorporated into the mixed layer. We also examine how the inclusion of the residual layer above a shallow convective boundary layer modifies the turbulent kinetic energy budget.

Large-scale subsidence mainly acts during the afternoon when the boundary layer is fully developed and, for the studied day, it is necessary to consider this in order to reproduce the afternoon observations.

Finally, we also investigate how CO_2 stored the previous night in the residual layer plays a fundamental role in the evolution of the CO_2 mixing ratio during the following day.

3.1   Introduction

The atmospheric boundary layer, characterized by a clear diurnal cycle, has been intensively studied since the 70's. A CBL exists during the day under fair weather conditions. The physical processes associated with CBL development have been extensively studied. Sorbjan (1996), Sullivan et al. (1998) and Conzemius and Fedorovich (2006) studied the role of the entrainment processes, and Moeng (1984); Fedorovich et al. (2001); Pino et al. (2003, 2006b); Pino and Vilà-Guerau de Arellano (2008) studied the contribution of shear in the generation and maintenance of CBL. Moreover, Yi et al. (2001); de Arellano et al. (2004); Casso-Torralba et al.; Vilà-Guerau de Arellano et al. (2009) studied the influence of CBL evolution on the CO_2 or isoprene budget.

Several methodologies have been used to study the CBL: LES numerical experiments (Moeng, 1984; Nieuwstadt and Brost, 1986; Cuijpers and Duynkerke, 1993; Sorbjan, 2007), MLM (Tennekes, 1973; Tennekes and Driedonks, 1981; Fedorovich, 1995; Pino et al., 2006b) observations (Kaimal et al., 1976; Angevine et al., 1994; Cohn and Angevine, 2000) and laboratory experiments (Deardorff et al., 1980; Fedorovich et al., 1996).

During the night, a shallower SBL with less turbulent intensity exists near the surface (Nieuwstadt, 1984; Carlson and Stull, 1986; Mahrt, 1998; Beare et al., 2006a). Between this layer and the FA, there may exist a neutrally stratified layer resulting from the decay of turbulence by the previous day's CBL. This layer, called the residual layer (RL), appears before sunset, when eddies have less energy due to the reduction of surface fluxes. The RL has the same characteristics in the state variables as in the original CBL (Stull, 1988). The importance and the role of the RL was studied by some authors (Balsley et al., 2008; Wehner et al., 2010) who examined turbulence in the RL by analyzing the Richardson number gradient in order to explain aerosol formation. Emeis and Schäfer (2006) used different instruments (e.g. sodar and ceilometer) to measure and study the heights of RL, CBL and SBL, as well as their influence on urban air quality and pollution.

The evolution from CBL to SBL and vice versa happens through two transitional processes. These two periods are difficult to study due to their rapid vari-

ability. The afternoon transition has been studied by using observations and/or numerical simulations (Sorbjan, 1997; Cole and Fernando, 1998; Edwards et al., 2006; Pino et al., 2006b; Angevine, 2008; Nadeau et al., 2011). However, there are still many unknowns during this period, as described in Section 1.3.

Regarding the morning transition, Angevine et al. (2001); Lapworth (2006); Bange et al. (2007); Angevine (2008) used observations to investigate the timing and importance of entrainment and surface winds in the development of CBL. LeMone et al. (2002) analyzed data recorded during CASES–97 to study the warming and moistening of the atmosphere due to boundary-layer depth, wind direction, and surface heterogeneity during this period. Sorbjan (1996); Beare (2008) analyzed the morning transition by using numerical models, such as LES, to study the relevance of different temperature lapse rates or the importance of domain sizes and grid length. Other authors used MLM, to study the impact of the atmospheric boundary-layer dynamics on the atmospheric chemistry (Ouwersloot et al., 2011).

Some aspects about the relevance of the RL during the morning transition have been studied by Fochesatto et al. (2001) and Gibert et al. (2011), who analyzed the dynamical coupling between the CBL and the RL by using lidar measurements. They observed the generation of internal gravity waves when there is a stable and stratified RL or when there is thermal forcing. They concluded that horizontal wind shear is not enough to observe internal gravity waves. Other authors (Stensrud, 1993; Balin et al., 2004) focused their research on the elevated RL, which is created when a CBL over an elevated terrain is advected over a lower CBL. Moreover, Han et al. (2011) studied the evolution of the CBL when it is covered by a neutral layer after the morning transition. Finally, Doran et al. (2003) and Morris et al. (2010) examined the vertical mixing of different chemical compounds, such as ozone, nitrogen oxide or carbon monoxide during the morning transition.

3.2 Objectives

The role of the RL during the morning transition and the role of subsidence during the whole evolution of the convective boundary layer is studied by using observations, mixed-layer theory (Tennekes and Driedonks, 1981) and LES model (DALES (Heus et al., 2010)). In contrast with previous studies, by performing a sensitivity analysis on the residual layer and subsidence characteristics, we analyze the importance of these processes on the diurnal evolution of the convective boundary layer. By combining RL and subsidence, four different DALES numerical experiments were performed: RL with subsidence (RLs), RL without subsidence (RLns), non-RL with subsidence (nRLs), and non-RL without subsidence (nRLns). Specifically, our research objectives can be summarized as follows:

1. To study the variations in the evolution of the boundary-layer depth resulting from the presence of RL and subsidence.

2. To analyze whether the previous night's characteristics have any relevance on the potential temperature vertical profile and temporal evolution.

3. To observe the sensitivity of the turbulent kinetic energy budget during the morning transition and the evolution during the day resulting from RL.

4. To study the influence of RL on the observed evolution of the CO_2 mixing ratio.

We take advantage of the observations made during an intensive observational campaign of the project BLLAST (Lothon et al., 2014). Specifically, the selected period used to develop this study was IOP 9 (1 July 2011), a clear and calm day. This IOP presented the best characteristics to study the role of residual layer during the morning transition. As it was explained in Section 2.6, the evolution of z_1 can be included in type 2 which means that z_1 shows an abrupt increase during the morning, reaching values around 1200-1400 m before midday and becoming approximately constant the rest of the day.We study the role played by RL during the morning and the role of subsidence in the evolution of the CBL can be studied because the boundary-layer depth remains constant after the morning transition.

3.3 Methodology

As described in Section 1.4, we use the observations recorded during the BLLAST field campaign and two numerical models: MLM and DALES.

3.3.1 Observations

The observations used here to initialize, drive and qualitatively validate the numerical experiments were recorded during the observational campaign of the BLLAST project (Lothon et al., 2014).

To develop this study, we mainly use the data recorded at the EC-stations, standard radio soundings, radar wind data and UHF wind profiler all of them located in Supersite 1.

The EC-stations were able to obtain a high rate measurements, that enable the observation of fluctuations in wind, temperature, humidity, CO_2 and surface fluxes as shown in Table 2.5. Specifically, we use the measurements taken at the 60 m tower, the micro-site and the edge site.

Additionally, we use the measurements of the UHF wind profiler to define the boundary-layer depth and the standard radio soundings launched during this IOP to analyze the vertical profiles of temperature, wind and humidity. The characteristics of these measurements are described in Section 2.6.
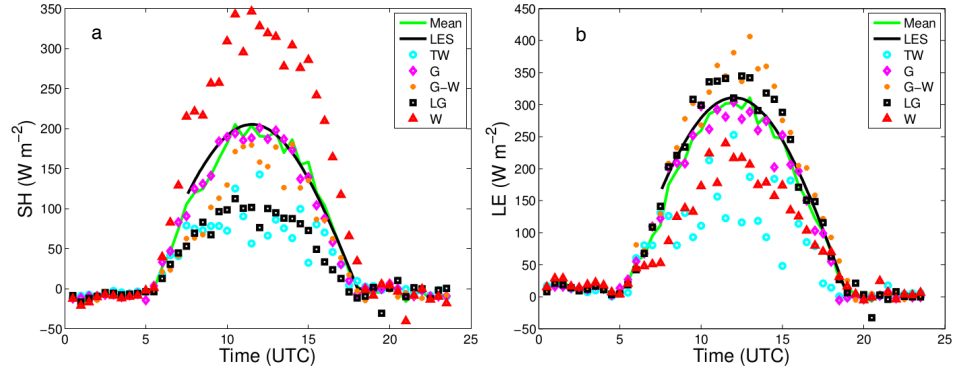
Figure 3.1: Temporal evolution of (a) sensible and (b) latent heat fluxes on 1 July 2011 observed at 2 m and 30 m at the tower, its mean (green line), and the prescribed evolution in the numerical experiments (black line). Observations are from the EC instrument at the tower over grass (TW, cyan circles), over short grass (G, magenta diamonds), over the edge between the long grass and the wheat (G–W, orange dots), over long grass (LG, black squares) and over wheat (W, red triangles).

3.3.2   Numerical experiments: MLM and DALES

Two numerical models of different complexity are used to study the evolution of the convective boundary layer during the selected day: DALES (Heus et al., 2010) and an MLM (Tennekes and Driedonks, 1981), which are described in detail in Sections 1.3.1 and 1.3.2, respectively. Both models are initialized and driven by observations.

For all the numerical experiments performed, the prescribed surface heat fluxes are based on the observations made by these 5 EC-stations over different land uses located at Supersite 1 where most of radio soundings were launched. Figure 3.1 shows the 1 July 2011 observed temporal evolution of sensible and latent heat fluxes and the prescribed evolution to drive DALES numerical experiments. Additionally, MLM is driven by the same evolution of surface heat fluxes, but starting at 11:00 UTC. The version of the MLM used here does not include the RL in its vertical profile. Consequently, it can only be used for developed convective boundary layers.

The domain chosen for the DALES numerical experiments was $12.8 \times 12.8 \times 3.056$ km^3, and we define 256 points in each direction (50 and 12 m resolution in the horizontal and vertical directions, respectively). This setup has a similar horizontal domain to the campaign site, having also enough vertical resolution to study entrainment processes (Pino et al., 2003, 2006a; Sullivan and Edward, 2011). Our DALES numerical experiments ran for 12.5 hours, starting at 07:30 UTC in order to include the morning transition in the simulations.

To analyze the role played by the RL in the morning evolution of the convective boundary layer, two different vertical profiles of potential temperature (θ),
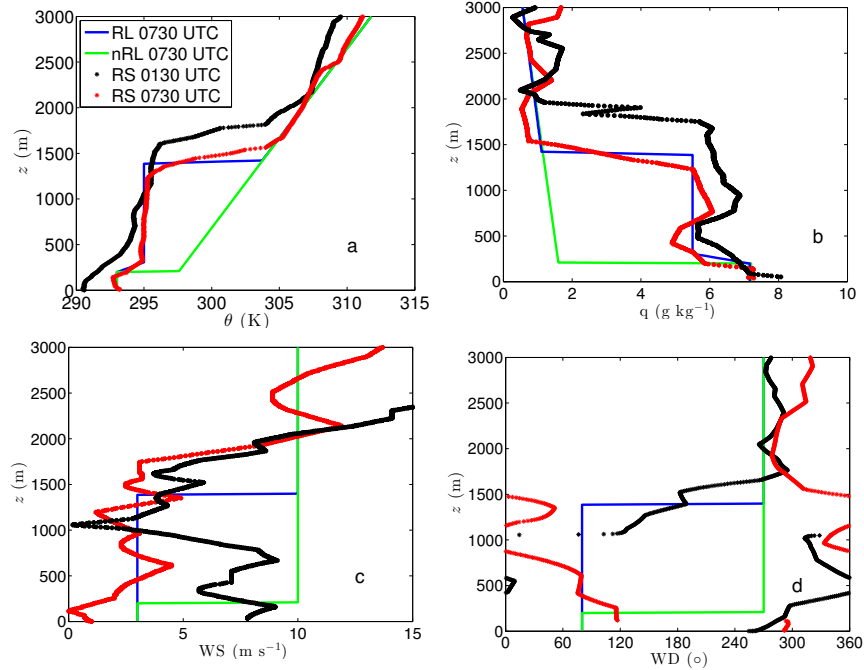
Figure 3.2: Vertical profile of (a) potential temperature, (b) specific humidity, (c) wind speed and (d) wind direction observed by the radio soundings launched at 01:30 (black dots) and at 07:30 UTC (red dots) on 1 July 2011. Additionally, the vertical profiles based in the observations for initializing the DALES RL numerical experiments (solid blue) and nRL numerical experiments (solid green) are shown. Table 1 shows the values which characterize the initial profiles of θ, q, u and v.

specific humidity (q) and wind are considered to initialize DALES. To include the residual layer in DALES (RL numerical experiments), we initialize it following the observations taken by the radio sounding launched at 07:30 UTC. We select this initialization method to obtain realistic simulation results based on BLLAST field campaign measurements. Figure 3.2 shows the vertical profiles of θ, q, and wind speed and direction observed at 01:30 and 07:30 UTC, and the prescribed vertical profiles used for initializing DALES RL and no-RL numerical experiments.

Table 3.1 shows the values of the θ, q and horizontal wind components that define the initial profiles of the DALES and MLM runs. For the RL numerical experiments (blue line in Fig. 3.2), the initial vertical profiles of θ and q are divided into three different layers: CBL from surface to $z_{1,0}$, $z_{1,0}$ being the initial boundary-layer depth; RL from $z_{1,0}$ to $z_{RL,0}$, $z_{RL,0}$ being the initial residual layer depth; and FA above $z_{RL,0}$. The potential temperature (specific humidity) in the CBL and in the RL are, respectively, $\theta_{1,0}$ ($q_{1,0}$) and $\theta_{RL,0}$ ($q_{RL,0}$). The

Table 3.1: Based on the observations taken at the BLLAST campaign on 1 July 2011, initial and prescribed values used for DALES (RL and nRL numerical experiments) and MLM of the boundary-layer depth, mixed layer and residual layer values of the scalars ($\theta_{1,0}$, $\theta_{\mathrm{RL},0}$ and $q_{1,0}$, $q_{\mathrm{RL},0}$) and their corresponding jump at the inversion ($\Delta\theta_{1,0}$, $\Delta\theta_{\mathrm{RL},0}$, $\Delta q_{1,0}$ and $\Delta q_{\mathrm{RL},0}$). γ_i is the FA lapse rate of each variable i. Initial ($u_{1,0}$, $u_{RL,0}$, $v_{1,0}$, $v_{RL,0}$), and geostrophic (u_g, v_g) wind components are also indicated Surface fluxes ($\overline{\omega'\theta'}|_\mathrm{s}$ and $\overline{\omega'q'}|_\mathrm{s}$) are prescribed as $0.1668\,\sin(\pi(t-5)/12.5)$ and $0.1032\,\sin(\pi(t-5.5)/13.5)$ respectively. Time t goes from 0 (07:30 UTC) to 45000 s (20:00 UTC).

	RL	nRL	MLM (11:00 UTC)
$\theta_{1,0}$ (K)	293	293	295.5
$\Delta\theta_{1,0}$ (K)	2	5	8
$z_{1,0}$ (m)	210	210	1300
$\theta_{\mathrm{RL},0}$ (K)	295	–	–
$\Delta\theta_{\mathrm{RL},0}$ (K)	9	–	–
$z_{\mathrm{RL},0}$ (m)	1422	–	–
γ_θ (K m^{-1})	0.005	0.005	0.005
$q_{1,0}$ (g kg^{-1})	7.16	7.16	8
$\Delta q_{1,0}$ (g kg^{-1})	−1.66	−5.66	−5
$q_{\mathrm{RL},0}$ (g kg^{-1})	5.50	–	–
$\Delta q_{\mathrm{RL},0}$ (g kg^{-1})	−4.41	–	–
γ_q (g (kg m)$^{-1}$)	−0.00035	−0.00035	−0.00035
$u_{1,0}$ (m s^{-1})	−2.95	−2.95	−2.95
$v_{1,0}$ (m s^{-1})	0.52	0.52	0.52
$u_{RL,0}$ (m s^{-1})	−2.95	–	–
$v_{RL,0}$ (m s^{-1})	0.52	–	–
u_g (m s^{-1})	10	10	10
v_g (m s^{-1})	0	0	0

inversion jumps at the two boundaries are $\Delta\theta_{1,0}$ ($\Delta q_{1,0}$) and $\Delta\theta_{\mathrm{RL},0}$ ($\Delta q_{\mathrm{RL},0}$). In the FA, the potential temperature (specific humidity) lapse rate is γ_θ (γ_q).

For the numerical experiments without the residual layer (nRL), the initial vertical profiles for running DALES (green lines in Fig. 3.2) are divided into two layers as the scheme shown in Fig. 1.6: CBL and FA. The same notation is used for the CBL values ($\theta_{1,0}$ and $q_{1,0}$) and FA lapse rates (γ_θ and γ_q).

LeMone et al. (1999); Pino et al. (2003); Conzemius and Fedorovich (2006), among others, showed that shear at the inversion influences entrainment fluxes. Consequently, initial and geostrophic vertical profiles are defined for all the DALES numerical experiments based on the radio sounding observations at 07:30 UTC (see Figs. 3.2c, d). In contrast to the previous variables, the initialization of wind is more complex because the observations show that the wind is not as well mixed inside the ML. We decide to initialize wind profile using constant values at a height below the FA, with $u = -2.95$ and $v = 0.52$ m s^{-1}

being equal to the geostrophic wind in the FA. Regarding the geostrophic wind, we use the radio soundings launched during the whole day to prescribe $u_g = 10$ and $v_g = 0$ m s^{-1}, constant with height. The roughness length, z_0, is 0.1 m and the latitude is $\phi=43°$. Despite the selection of the initial wind profile based on observations, DALES results are not able to fit the wind observations. This is mainly because on 1 July 2011 the atmospheric dynamics were mainly driven by the orography, and mountain-valley breezes appeared. DALES numerical experiments consider a flat terrain and do not include any advection of momentum.

To study the role of subsidence, additional simulations are performed. The value of subsidence to be included in DALES and MLM numerical experiments are obtained, in accordance with Yi et al. (2001), by analyzing the observed vertical profile of the potential temperature at 01:30 and 07:30 UTC on 1 July 2011 (see Fig. 3.2). The depth of the residual layer (z_{RL}) decreases by 215 m within 6 hours (01:30 − 07:30 UTC). This represents a subsidence velocity of 9.95×10^{-3} m s^{-1}. Subsidence is included in two DALES numerical experiments as follows. The subsidence vertical profile increases linearly from 0 at the surface to 9.95×10^{-3} m s^{-1} at $z_{RL,0}$ in both numerical experiments (RL and nRL numerical experiments). In FA, we defined a constant subsidence equal to 9.95×10^{-3} m s^{-1}. Despite the fact that subsidence may evolve during the day, we prescribe a constant subsidence profile, because the main objective of the paper is not to fit the observations exactly, but to analyze the role of RL and subsidence. For the same reason, and taking into account the low winds recorded during the selected IOP, heat and moisture advection are not considered. Nevertheless, heat and moisture advection may have an important role in other days of the campaign as it is shown in Pietersen et al. (2014).

(Pietersen et al., 2014) analyzes the influence of subsidence and advection on another day of the campaign (IOP5, 25 June 2011). In contrast to our study, they run DALES with a prescribed subsidence which evolves during the simulation. They observed an overestimated boundary-layer depth when they ran the DALES model without subsidence compared with UHF, Lidar, radio soundings, RPAs and aircraft measurements. Therefore, their prescribed subsidence in the model was defined from the difference between the entrainment velocity of DALES run without subsidence and the entrainment velocity of the observations. The structure of the subsidence vertical profile introduced in DALES is the same as in our study: zero at the ground, with a linear increase up to the top of the CBL, until the subsidence is constant in height above the CBL. They compared the estimated subsidence with the ECMWF model at 12:00 UTC, and both acceptably fit for these few points. From that point, subsidence followed an evolution close to the entrainment velocity. The final quantified values for subsidence and advection were determined iteratively, using the observations as a constraint.

MLM is used to create a fast and simple characterization of the CBL, and the results can be compared with the results of the DALES numerical experiments to verify if a simpler model can also simulate the evolution of the CBL from midday while considering subsidence. To initialize MLM, we used the information of the

first radio sounding, which shows a completely developed CBL: the one launched at 11:00 UTC. Table 3.1 shows the values which characterize the MLM initial profile of θ and q. We prescribed in MLM a divergence at $z_{1,0}$, being equal to 7.65×10^{-6} s^{-1}, which was obtained by considering a subsidence velocity equal to 9.95×10^{-3} m s^{-1} and the initial depth of the boundary layer for MLM ($z_{1,0}$= 1300 m).

3.4   Results

In the next sections, we demonstrate the importance of the RL during the morning transition and of subsidence during the afternoon on 1 July 2011 by analyzing the observed and simulated evolution of the boundary-layer depth, potential temperature, turbulent kinetic energy budget and its influence on the evolution of CO_2.

3.4.1   Potential temperature vertical profile

Figure 3.3 shows the vertical profile of potential temperature observed with the radio soundings, which were obtained by MLM with subsidence included, and which were also obtained by DALES using numerical experiments at different hours on 1 July 2011. The figure illustrates the importance of the morning conditions for the evolution of the boundary-layer depth and of the potential temperature during the whole day. At 08:30 UTC (Fig. 3.3a), when the RL has not been already incorporated into the boundary layer, the mixed-layer potential temperature in the numerical experiments (which consider the RL) are 1.7 K lower than nRL numerical experiments, even though the boundary-layer depth is similar. This is due to the larger potential temperature inversion jump, simulated by the nRL numerical experiments, which increases entrainment heat flux (see Eq. 1.2).

As the day progresses, the difference of mixed-layer θ increases between nRL and RL numerical experiments; RL numerical experiments become approximately 4 K colder than nRL numerical experiments (see Fig. 3.3b), which fits the observations. As the nRL presents a lower depth of the CBL during a longer period of time, its temperature increases faster, reaching higher values during this period. However, after 13:00 UTC, when the boundary-layer depth simulated by the nRL numerical experiments reaches around 1300 m, the difference in the mixed-layer potential temperature between RL and nRL numerical experiments is maintained (see Figs. 3.3c, d), due to the similar values of entrainment heat flux and boundary-layer depth simulated for all the numerical experiments. Moreover, the influence of subsidence in the boundary-layer depth and potential temperature is noticeable from midday. RLns and nRLns clearly overestimate the observed boundary-layer depth by several hundred meters, and the potential temperature is 0.5 K colder (see Figs. 3.3c, d).
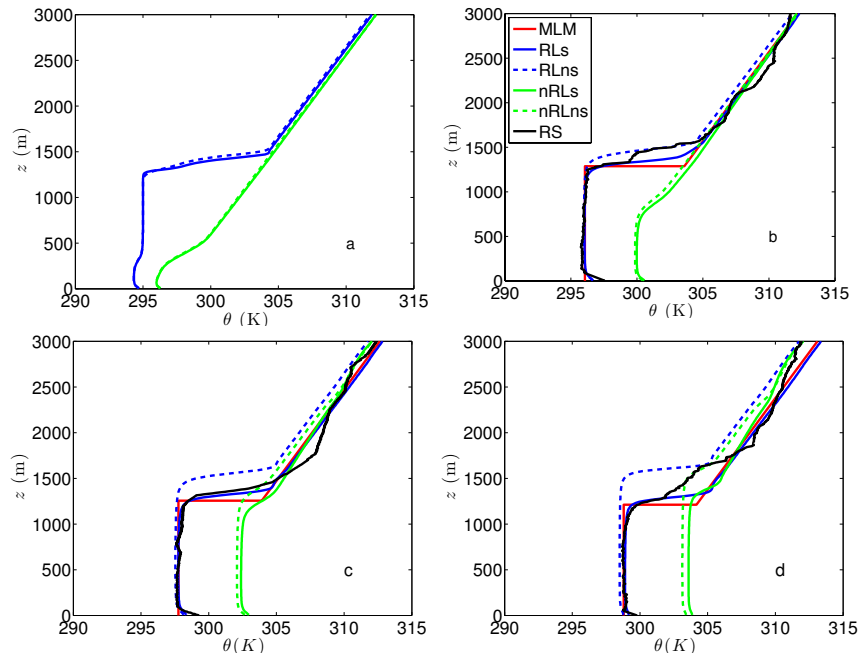
Figure 3.3: Profile of the 30-minutes averaged potential temperature at (a) 08:30, (b) 11:00, (c) 14:00 and (d) 17:00 UTC on 1 July 2011 observed by the radio soundings (solid black) and obtained by MLM (solid red) and DALES runs (RLs, solid blue; RLns, dash blue; nRLs, solid green; and nRLns, dash green line).

3.4.2   Mixed-layer temperature temporal evolution

Figure 3.4 shows the observed temporal evolution of the 2 m potential temperature over different land uses during 1 July 2011. Differences between potential temperature measurements are below 1 K, except for the potential temperature measured over wheat. As already pointed out by previous studies (Nadeau et al. (2011), among others), the surface heat flux over wheat is larger (Fig. 3.1), yielding to higher 2 m potential temperature. The figure also shows the temporal evolution of potential temperature, obtained by the MLM with subsidence and by the four DALES numerical experiments at the middle point between the surface and the height when the heat flux becomes 0 Wm^{-2} below z_1. Notice that measurement height is different from the height where the DALES results are considered (the measurement height varies with z_1), which may produce some discrepancies .

If the residual layer is not considered (nRLs and nRLns numerical experiments), the simulated potential temperature increases rapidly, due to the initially prescribed large potential temperature jump, which increases the entrainment heat flux. Moreover, the CBL is shallow during the morning, which enhances the CBL-heating rate (see Eqs. 1.1 and 1.2 and Figs 3.3a, b). Consequently, these DALES runs do not fit the observations.

In contrast, if the residual layer is included in the initial profile of the DALES numerical experiments, the temporal evolution of the simulated potential temperature presents two different regimes. For approximately the first 1.5 hours of the simulation, the boundary layer is shallow but the inversion layer jump is moderate when compared with the nRL numerical experiments. Consequently, the entrainment heat flux is smaller and the simulated potential temperature increases smoothly, approximately fitting the observations. At 09:00 UTC, when the simulated potential temperature in the mixed layer and in the residual layer are the same, the boundary-layer depth increases to approximately 1300 m. Although, the new potential temperature inversion jump is larger, the heating rate is lower when compared with the first 1.5 hours of simulation, due to the large z_1 simulated at this moment. Thus, the DALES RL numerical experiments fit the observations better. Taking into account that prescribed fluxes are similar to the ones measured short over grass (micro-scale surface heterogeneity site), the model is able to fit the observed temperature measured over grass except during a short period in the early morning and the during the late afternoon.

Once the mixed layer has incorporated the residual layer, the MLM starts at at 11:00 UTC, considering subsidence, and it simulates correctly the evolution of the potential temperature; i.e., it is close to the observed values and to the results of DALES runs that take into account the residual layer.

The role played by subsidence in the evolution of the potential temperature can only be appreciated at the end of the afternoon. This is for several reasons. Taking into account how subsidence is prescribed, its effects are very small if $z_1 < z_{RL,0}$, that is, before 10:00 UTC or 16:00 UTC for the RL and nRL numerical experiments, respectively. Moreover, in the afternoon, the surface and (consequently) the entrainment flux become largely reduced, decreasing the

boundary-layer growth. However, none of the numerical experiments are able to simulate the decrease in potential temperature observed from 17:00 UTC, which is likely produced by a weak negative temperature advection as a consequence of the start of the change of wind direction produced by the slope flows.
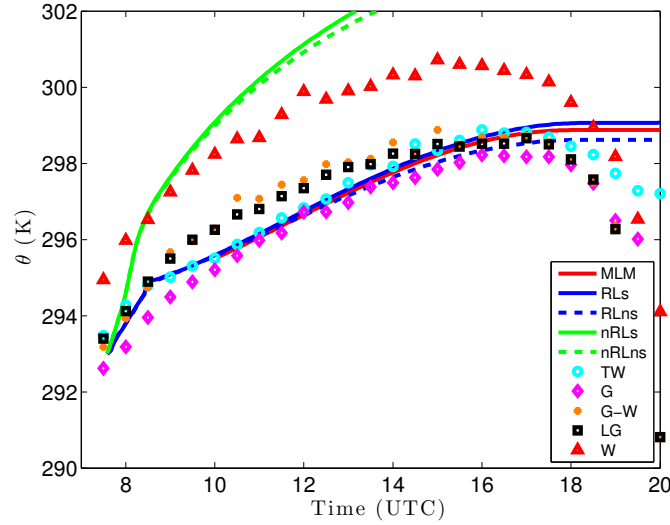

Figure 3.4: Temporal evolution of potential temperature on 1 July 2011 observed by different instruments at 2 m (symbols) and obtained (lines) by MLM with subsidence (red) and DALES (RLs, solid blue; RL, dash blue; nRLs, solid green; and nRL, dash green). Observations are from EC instrument at the tower over grass (TW, cyan circles), over short grass (G, magenta diamonds), over the edge between long grass and wheat (G–W, orange dots), over long grass (LG, black squares) and over wheat (W, red triangles).

3.4.3   Boundary-layer depth temporal evolution

Figure 3.5 shows the time evolution of the refractive structure coefficient (observed by the UHF wind profiler) and the boundary-layer depth (estimated from the radio soundings), launched at 07:30, 11:00, 14:00, 17:00, and 20:00 UTC. It was obtained by MLM with subsidence and by DALES numerical experiments (RLs, RL, nRLs and nRL). z_1 is defined by using UHF measurements as the height of the maximum refractive structure coefficient. This maximum means that the larger gradients of humidity and/or shear are located there. z_1 for MLM and DALES is defined as the height where the minimum buoyancy flux occurs (Seibert et al., 2000). z_1 estimated from the radio sounding data is defined as the height where the maximum virtual potential temperature vertical gradient occurs. The reliability of using isolated radio soundings to obtain the depth of the boundary layer has been sometimes criticized (e.g. Stull 1988). Never-

theless, radio sounding measurements in this study fit correctly with the UHF measurements, and the small dissimilarities can be attributed to the different procedures used to obtain z_1 (Sullivan et al., 1998).
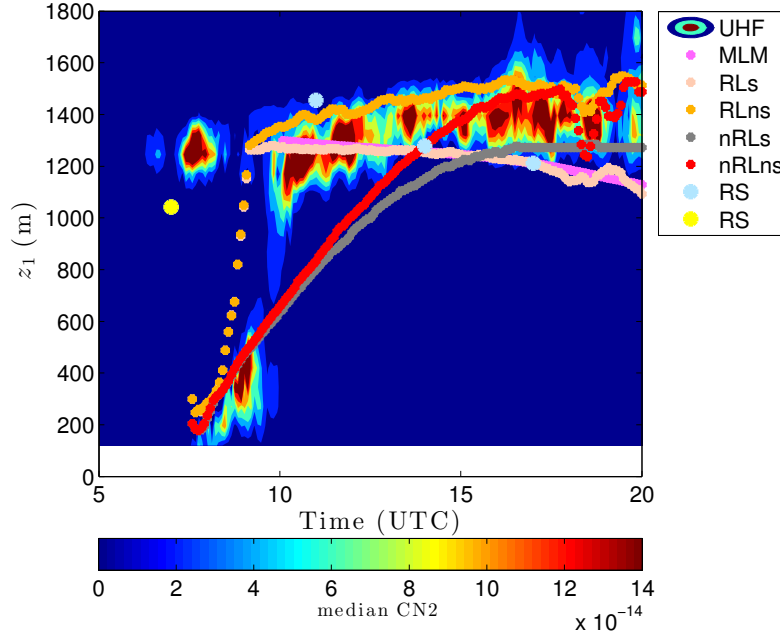
Figure 3.5: Temporal evolution during 1 July 2011 of the refractive structure coefficient measured by UHF wind profiler (color contour), and boundary-layer depth estimated from radio soundings (light blue dots), and obtained by MLM (magenta line), and DALES runs (RLs, pink; RLns, orange; nRLs, grey; and nRLns, red lines). Yellow dot represents the residual layer depth estimated from a radio sounding.

UHF wind profiler measurements show the existence of a residual layer during the early morning. At around 09:00 UTC we can see that the mixed layer merges with the RL from the previous night, producing a sudden increase in the boundary-layer depth (see Fig. 3). From this moment on, the observed boundary-layer depth remains approximately constant during 7 hours. Taking into account that the surface heat flux is still positive for several hours, this might be explained by the existence of subsidence that prevents the mixed layer from growing. During the afternoon, due to subsidence and the decrease in surface fluxes, UHF and radio sounding measurements show a slight decrease in the boundary-layer depth from 17:00 UTC. By analyzing the mean wind vertical structure from UHF wind profiler, the sudden increase of z_1 is also observed (not shown).

The DALES numerical experiments, including the residual layer in its initial profile, fit correctly with the observations, simulating the sudden increase in

the boundary-layer depth during the morning transition. On the other hand, the DALES nRL numerical experiments simulate a progressive increase in the boundary-layer depth, and it underestimates by several hundred meters the observations during the whole morning until 13:00 UTC. In all DALES results, small fluctuations in z_1 are observed at the end of the day (around 18:00 UTC), due to ceasing of the surface heat flux, which produces fluctuations in the buoyancy heat flux vertical profile (Pino et al., 2006b).

Previous studies, such as Fedorovich (1995); Vilà-Guerau de Arellano et al. (2009) or Ouwersloot et al. (2012), demonstrate that zero-order models can be useful and valid also for studies of the evolution of the boundary layer. In our study, the boundary-layer depth obtained with MLM has almost the same value as from the DALES numerical experiments that include both the residual layer and subsidence, confirming the studies previously performed.

Regarding the role of subsidence , it can be observed that the numerical experiments that include subsidence (RLs, nRLs, MLM) fit better with the observations, but they slightly underestimate the observed boundary-layer depth (less than 100 m with respect to UHF measurements). This may be due to subsidence diurnal variability. The numerical experiments that do not consider subsidence overestimate the observed z_1 by less than 200 m at the end of the day. Long-term observations of the boundary layer show the importance of considering subsidence to obtain realistic approximations (Yi et al., 2001).

3.4.4 Entrainment heat flux and momentum fluxes

As the surface heat fluxes are the same, and advection is not considered, to understand the differences in the boundary-layer evolution during the morning between the numerical experiments, this section will focus our analysis on the entrainment fluxes, keeping in mind the evolution of z_1, as shown in Fig. 3.5 (see Eq. 1.1).

Figure 3.6a shows the temporal evolution of heat flux at z_1 for the nRLns and RLns numerical experiments (dashed and solid lines, respectively). During early morning, there are clear differences between nRLns and RLns numerical experiments, but from 14:00 UTC to the end of the simulation, the entrainment heat flux for both DALES numerical experiments is similar because in both cases z_1 is large.

To analyze the morning transition, Fig. 3.6.b shows a zoom from 8:30 to 10:00 UTC of Fig. 3.6.a. Moreover, we include the entrainment heat flux at the top of the RL (dotted line) to compare the entrainment heat flux at z_1 and z_{RL}, before the inclusion of the RL. Before 09:00 UTC, z_1-growth is similar in both simulations. Consequently, the difference in the entrainment heat flux between the numerical experiments is due to the potential temperature inversion jump (see Eq. 1.2); $\Delta\theta_1$ is 2 K larger for nRLns than for RLns at 08:30 UTC (see Fig. 3.3a). Therefore, a larger entrainment heat flux is obtained for the nRLns numerical experiment, and the mixed-layer potential temperature increases more for this numerical experiment.

Just when the residual layer is incorporated into the boundary layer in the

RLns numerical experiment, the entrainment heat flux must be nearly zero, because the temperature jump is zero at z_1 (see Eq. 1.2). Then the residual layer is incorporated into the boundary layer, and the entrainment heat flux increases from -0.02 to -0.045 K m s^{-1}, introducing more air from the FA. This is mainly due to the increase in the potential temperature inversion jump (from nearly 0 to 1 K), and also to the large increase in the z_1-growth (see in Figs. 3.3a, b).
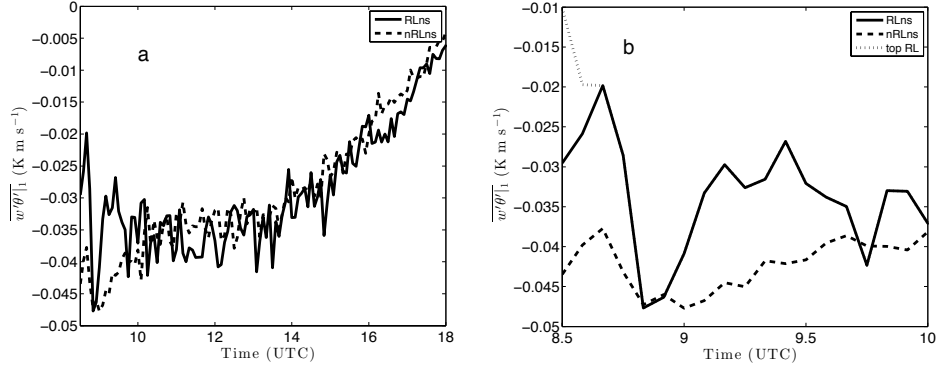
Figure 3.6: (a) Temporal evolution of the entrainment heat flux for the RLns (solid line), and nRLns (dashed line) DALES numerical experiments. (b) Temporal evolution of the entrainment heat flux during the morning including also the entrainment heat flux at the top of the RL (pointed line)
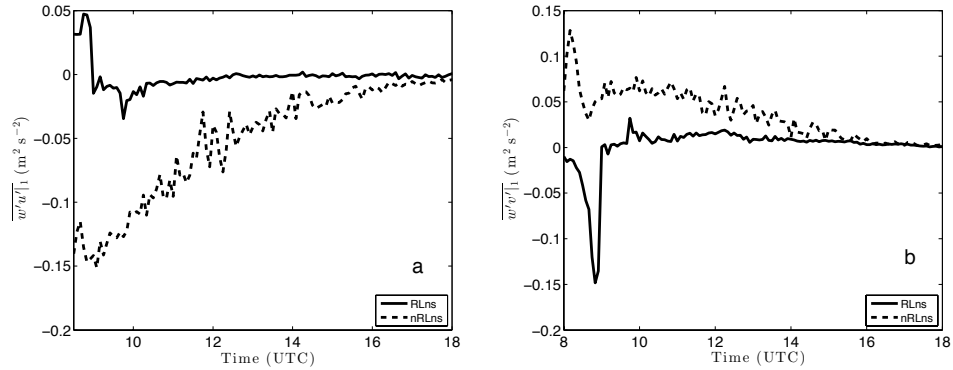
Figure 3.7: Temporal evolution of the momentum fluxes at the top of the BL for the RLns (solid line), and nRLns (dashed line) DALES numerical experiments for (a) u direction and (b) v direction

Figure 3.7 shows the temporal evolution of momentum flux at z_1 for the nRLns and RLns numerical experiments (shown in Table 3.1). At 8:30 UTC,

larger momentum fluxes at z_1 are simulated for nRL due to the different setup in wind characteristics. The nRL numerical experiments have a larger jump on the horizontal velocities at z_1, as shown in Fig. 3.2.c. On the other hand, the RL numerical experiments have a weaker wind shear at the top of the BL, because the same wind conditions were defined inside the boundary layer and in the residual layer. This fact can also be observed in the observations made by the UHF wind profiler (not shown). After the residual layer is incorporated into the boundary-layer, the momentum flux at z_1 decreases in both cases, as the wind inversion jump at z_1 increases as well as the z_1-growth. As the IOP progresses, the momentum fluxes in both numerical experiments get similar.

3.4.5 Turbulent kinetic energy budget

Under horizontally homogeneous conditions, the turbulent kinetic energy (TKE) budget reads (Stull, 1988):

$$
\begin{aligned}
\frac{\partial \overline{e}}{\partial t} &= -\left[\overline{w'u'}\frac{\partial \overline{u}}{\partial z} + \overline{w'v'}\frac{\partial \overline{v}}{\partial z}\right] + \frac{g}{\theta_{vr}}\overline{w'\theta_v'} - \\
&\quad - \frac{\partial \overline{w'e'}}{\partial z} - \frac{1}{\rho_0}\frac{\partial \overline{w'p'}}{\partial z} - \varepsilon
\end{aligned}
\tag{3.1}
$$

where u', v', w' are the turbulent fluctuations of the velocity components, p is the pressure, ρ_0 is a reference density, θ_{vr} is a reference virtual potential temperature, $\overline{e} = 0.5(\overline{u'^2 + v'^2 + w'^2})$ is the mean turbulent kinetic energy, and ϵ is the viscous dissipation of TKE. The term on the left-hand side represents storage (STO) of TKE, and the terms on the right-hand side represent: shear (S), buoyancy production (B), turbulent transport (T), pressure correlation (P), and viscous dissipation (D).

Figure 3.8 shows the vertical profile of the averaged 30-min profile of the different resolved TKE terms at (top) 08:30, (middle) 09:00, and (bottom) 14:00 UTC, for all the numerical experiments. The left panels show the numerical experiments where the residual layer is considered, whereas the right panels show those without the residual layer prescribed in the initial profile. The horizontal dashed lines mark z_1 for each numerical experiment. Notice the different range of the horizontal axis of Figs. 3.8c and d. Turbulent transport and the pressure correlation terms are plotted together as the convergence of the turbulence kinetic energy flux (Driedonks, 1982).

At 08:30 UTC (Figs. 3.8a, d), when the boundary layer is shallow for all the numerical experiments, we obtain larger values of all the TKE-terms in the entrainment zone for the nRL numerical experiments, but values are similar near the surface. At this moment, larger entrainment heat flux is simulated for the nRL numerical experiments (see Fig. 3.6). Moreover, nRL presents larger momentum fluxes at z_1 (see Fig. 3.7), due to the different setup in wind characteristics (see Table 3.1). To balance the budget, the pressure-transport term and the dissipation term are also larger for the nRL numerical experiments,
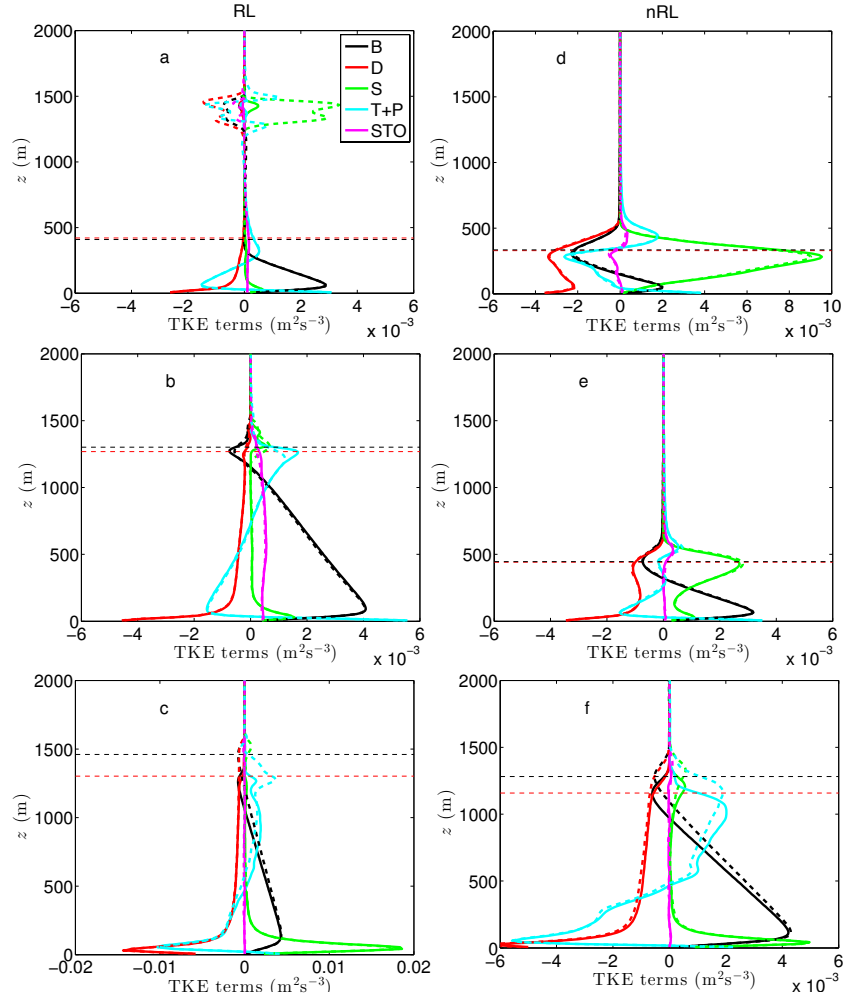
Figure 3.8: Vertical profiles of the 30-minutes averaged TKE–terms for the (left) RLns (dashed lines) and RLs (solid lines) and (right) nRLs (solid lines) and nRLns (dashed lines) numerical experiments at (top) 08:30, (middle) 09:00 and (bottom) 14:00 UTC. Buoyancy production (black line), dissipation (red line), shear production (green line), turbulent transport and pressure (cyan line) and storage (magenta line) are shown. The red and black dashed lines mark for the subsidence and no–subsidence cases z_1 averaged every 30 min.

especially in the entrainment zone (compare Figs. 3.8a, d). As expected, the influence of subsidence cannot be noticed at this early hour because subsidence was prescribed as increasing at the surface, being maximum at z_{RL}. The TKE distribution of Figs. 3.8a and d was previously observed in the LES morning transition analysis by Beare (2008).

Focusing on Fig. 3.8a, at the top of the RL, turbulence exists due to the interaction between this layer and the FA, which have different thermodynamic conditions. Smaller turbulence (S, T+P) and consequently dissipation are simulated at the top of the RL for the RLs numerical experiment (solid lines), because subsidence reduces turbulent movements.

The effect of including the residual layer into the mixed layer between 08:30 and 09:00 UTC can be clearly seen by comparing Figs. 3.8a and b, where the TKE terms of both RL numerical experiments are represented. Shear and dissipation terms become approximately constant in the middle of the mixed layer, being larger at the inversion due to the larger potential temperature inversion jump. Consequently, the pressure-transport term increases in this zone. In Fig. 3.8b, the subsidence effect can be already observed to produce a difference in z_1 of around 50 m between the RLns and RLs numerical experiments (compare red and black horizontal dashed lines). This fact can be compared with the nRL cases shown in Fig. 3.8e. In this figure the effect of subsidence is hardly observable, due to the lower z_1 simulated at this hour for the nRL numerical experiments.

From 08:30 to 09:00 UTC, the value of the different TKE terms for the nRL numerical experiments decreases (see Figs. 3.8d, e). This is due to the increase in the boundary-layer depth and the reduction of the inversion strength at z_1, which primarily reduces buoyancy and shear terms at the inversion and, to balance the budget the other terms.

At 14:00 UTC (Figs. 3.8c, f), similar z_1 is simulated for the nRL and RL numerical experiments having the same subsidence conditions. Notice the differences due to subsidence in z_1 around 200 m between the numerical experiments. At this moment, STO, B and T+P terms are approximately similar for all numerical experiments (note the different range of the x-axis between these two figures). However, larger S and, consequently, D terms are found for the RL numerical experiments near the surface. This is due to the fact that, from midday, when the boundary layer is similar for both numerical experiments, stronger winds at the mixed layer are simulated for the RL numerical experiments due to its initial wind profiles.

In Fig. 3.8f the effect of subsidence in the different TKE-terms can be analyzed. No differences between nRLs and nRLns can be observed in the lower part of the mixed layer. Additionally, subsidence plays an important role only in some of the TKE-processes. In the mixed-layer, subsidence hardly affects the terms of D, STO (very small) and S; and the main differences appear in the B and T+P terms. Subsidence decreases buoyancy production in the upper mixed layer, and consequently increases the T+P term. In the entrainment zone above z_1, comparing the areas of the TKE terms can lead to the conclusion that similar values are obtained for the two numerical experiments.

Figure 3.9 shows the evolution every 5 min of the vertical integration from 0 to z_1 of each TKE-term normalized by z_1. By using this normalization, the differences observed in Fig. 3.9 between the different numerical experiments cannot be attributed to a smaller vertical integration domain. For the three presented cases (RLns, nRLns and nRLs), the STO and T+P terms remain small when compared with the other terms during the whole evolution, becoming negligible after the morning transition.

In Fig. 3.9a the effect of including the residual layer in the initial profile can be analyzed. Until approximately 10:00 UTC, nRLns (dashed lines) presents a larger shear, occurring mainly in the entrainment zone (see Fig. 3.8d), due to the prescribed initial wind profile (see Table 1, and Fig. 3.2c); but it then reduces continuously, because the mixed-layer wind speed in the nRLns experiment increases and reaches values close to the geostrophic wind. The increase in surface shear does not compensate for this fact. Before including the RL, which can be clearly seen by the maximum of the B-integrated term around 09:00 UTC, the RLns numerical experiment (solid lines) presents very a small integrated-S term due to the initial prescribed wind profile (see Table 3.1, and Fig. 3.1c), which produces small wind shear at the surface and at the inversion zone during the first hours of the simulation. When the RL is incorporated, entrainment shear increases, but the normalized integrated-TKE is similar. Keep in mind that the integration depends on z_1 and, as a consequence, the shear above this height is not considered in the integration (see Figs. 3.8a, b, c). Afterwards, the integrated-S term in RLns increases mainly due to the increase in surface shear caused by the growth of mixed-layer wind speed. Entrainment shear for nRLns is reduced.

Regarding the integrated-B, during the first hours of the simulation it is larger for RLns than for nRLns (see Fig. 3.9a), because nRLns simulates much larger negative entrainment heat flux, producing smaller vertically integrated-B (see Figs. 3.6, 3.8a, d). Until 11:00 UTC, the integrated-B term increases for both numerical experiments (surface and entrainment heat fluxes increase), becoming similar.

Before 11:00 UTC, the integrated-D is slightly smaller for the RLns numerical experiment (solid lines). Later, integrated-D remains almost constant for nRLns, but increases for RLns until 11:00 UTC. At this time, the vertically integrated-S and D terms are similar for both numerical experiments.

From midday, the vertically integrated-B term is similar for both numerical experiments. This is because its integration produces similar values, despite the fact that z_1 is different until 15:00 UTC (see Fig. 3.5) and larger positive and negative heat fluxes are simulated for the nRLns numerical experiment (see Figs. 3.8c, f). However, the vertically integrated-S term decreases for the nRLns numerical experiment, although for the reasons mentioned above it continuously increases until 15:00 UTC for RLns. Consequently, to balance the TKE budget, a larger vertically integrated-D is also obtained for the RLns numerical experiment. From 15:00 UTC, surface and entrainment heat fluxes as well as entrainment momentum fluxes are quite low, and consequently the integration of all the TKE terms decreases.

The influence of subsidence in the integrated TKE is analyzed for the nRL cases by observing Fig. 3.9b. It can be concluded that differences can be noticed only in the normalized integrated B-term and, to a lesser extent, in the dissipation. Larger integrated buoyancy is simulated when subsidence is not considered (dashed black line). This difference is mainly related to entrainment processes, because if the same surface heat fluxes are prescribed for both numerical experiments, the buoyancy flux is similar in the lower mixed layer for nRLs and nRLns. That is, the positive buoyancy flux is similar for nRLs and nRLns. Consequently, the lower the boundary-layer depth is, the larger the integrated buoyancy flux that is obtained. This is because the entrainment buoyancy flux (negative flux) is smaller.

3.4.6   Influence of the residual layer on the observed evolution of the CO_2 mixing ratio

In this section, we analyze the importance of entrainment and surface CO_2 fluxes measured over different land uses in the evolution of the CO_2 mixing ratio and the effect of RL during morning transition. Some authors (de Arellano et al., 2004; Casso-Torralba et al.) have analyzed the importance of entrainment CO_2 fluxes, which are especially relevant during early morning, but over homogenous terrains. Moreover, Moncrieff et al. (1997), Baldocchi and Meyers (1998) and Soegaard (1999) analyzed the evolution of the CO_2 mixing ratio over heterogeneous terrains during daily and longer periods of time. Here, we deal with CO_2 surface fluxes measured over different land uses and their degree of influence on the CO_2 mixing ratio in an evolving convective boundary layer.

Figure 3.10 shows the observed temporal evolution from 14:00 UTC on 30 June 2011 to 14:00 UTC on 1 July 2011 of the CO_2 mixing ratio and CO_2 flux measured at 2 m over different land uses (moor, corn and grass) and we also include the measurements taken by the EC sensor located at 30 m on the 60 m tower over grass. Differences between CO_2 mixing ratio measurements over different land uses on 1 July 2011 are below 2 ppm during daytime, and below 10 ppm during nighttime. By comparing 2 and 30 m measurements, differences in the CO_2 mixing ratio are below 2 ppm at nighttime and below 12 ppm during daytime. During the night in general, a larger CO_2 mixing ratio is observed near the surface than at 30 m over the same land use.

Between 05:00 and 09:00 UTC, a remarkable decrease in the CO_2 mixing ratio is observed at 2 m. At 30 m the decrease in CO_2 is less pronounced. Before 09:00 UTC, the boundary layer is shallow (see Fig. 3.5), and the RL has not yet been incorporated into the mixed layer. During these hours, surface uptake and mainly CO_2 entrainment flux drive the decrease in the CO_2 mixing ratio (de Arellano et al., 2004; Casso-Torralba et al.). Additionally, during early morning, advection may also play a role. When entrainment flux mainly drives the decrease in CO_2 mixing ratio (around 06:00 UTC), the decrease is similar at both heights (2 and 30 m). Later on, when CO_2 surface fluxes become larger, differences appear between the CO_2 mixing ratio at 2 m and at 30 m. At 30 m, as expected, the CO_2 surface flux is smaller and, consequently, there is a
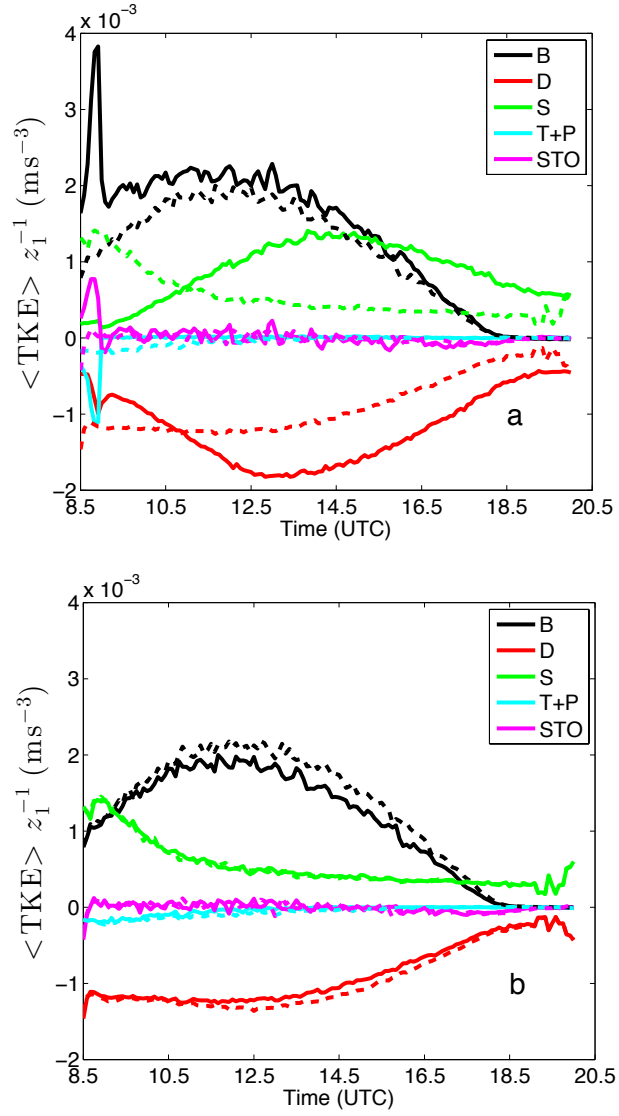
Figure 3.9: Temporal evolution of each vertically averaged (from 0 to z1) TKE–term normalized by z1. In (a) the influence of the RL is shown for (solid) RLns and (dashed) nRLns numerical experiments. In (b) the influence of subsidence for (dashed) nRLns and (solid) nRLs numerical experiments can be analyzed.
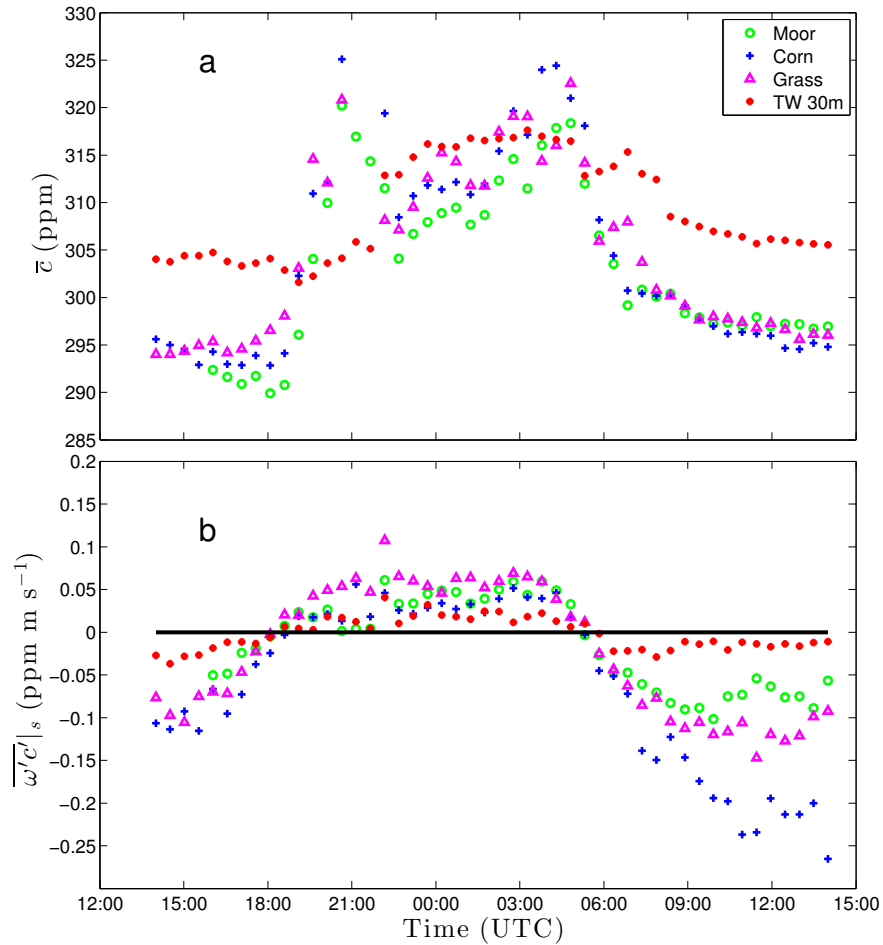
Figure 3.10: Temporal evolution from 30 June 2011 at 14:00 UTC to 1 July 2011 at 14:00 UTC of the observed (a) CO_2 mixing ratio and (b) CO_2 surface flux measured at 2 m over moor (green circles), over corn (blue crosses), over long grass (magenta triangles) and at 30 m over grass (red asterisks).

smoother decrease in the CO_2 mixing ratio.

During this IOP, no measurements of CO_2 entrainment flux were taken. However, we can estimate the CO_2 entrainment flux, since we have measurements of the CO_2 surface flux, of the boundary-layer depth and of the temporal evolution of the CO_2 mixing ratio in convective conditions. By using the general Eq. 1.1, we obtained a CO_2 entrainment flux which is 3 times larger than the CO_2 surface flux before 09:00 UTC. We cannot verify these results because CO_2 fluxes were only measured at the entrainment zone by the Sky Arrow and this aircraft only participated in the campaign from June 14 to June 26.

Once the RL is incorporated into the mixed layer, the boundary-layer depth increases suddenly to values close to 1300 m (see Fig. 3.5). As was shown in Section 3.3, the boundary-layer growth is almost zero from that time. Therefore, also the CO_2 entrainment flux is almost negligible (Yi et al., 2001). After 09:00 UTC, it can be observed in Fig. 3.10a that over 3 hours the CO_2 mixing ratio is around 297 ppm over all the surfaces, only varying by 1 and 1.5 ppm, depending on the land use. However, clearer differences in the CO_2 surface fluxes are observed (see Fig. 3.10b). The CO_2 mixing ratio presents only small variations because the observed z_1 from 09:00 UTC is large, and consequently $\overline{\omega'c'}|_{\mathrm{s}}/z_1$ is small. For the land uses shown in Fig. 3.10, $\partial \overline{c}/\partial t$ is around 0.3 ppm h^{-1} for moor and wheat, and close to 0.5 ppm h^{-1} for corn. Therefore, the mixing ratio is controlled mainly by mixed-layer growth, with the surface flux playing a less important role (Culf et al., 1997; Pino et al., 2012).

From this analysis, we conclude that on 1 July 2011, before the merging of CBL and RL, the CO_2 mixing ratio decreases from the high values of CO_2 observed during the night to the CO_2 mixing ratio of RL (CO_2 mixing ratio of the previous day), mainly due to CO_2 entrainment flux. This CO_2 mixing ratio is almost constant during the rest of the day, due to the large and constant value of z_1.

3.5   Conclusions

The impact of the residual layer and subsidence on the evolution of a CBL is studied by means of observations taken during the BLLAST campaign, DALES numerical experiments and by applying the mixed-layer theory. In contrast with previous analyses of the morning transition (Angevine et al., 2001; LeMone et al., 2002; Lapworth, 2006; Beare, 2008), we use a sensitivity analysis of the numerical experiments to study the influence of the two processes in the evolution of the convective boundary layer.

Depending on whether or not the residual layer is considered in the DALES numerical experiments, different evolutions of the boundary layer are simulated. The potential temperature (simulated by the numerical experiments that include the residual layer) fits correctly with the observations, which contrasts the numerical experiments without the residual layer (nRL) because it simulates a too high mixed-layer heating rate during the early morning. By using mixed-layer theory, we conclude that the difference in the evolution of the potential tem-

perature is due to entrainment heat flux, because the same surface fluxes are prescribed for all the numerical experiments and the z_1 growth is similar before the morning transition. After the merge of residual layer and CBL, larger entrainment heat flux is simulated in the numerical experiments with residual layer, because $\Delta\theta_1$ and $\partial z_1/\partial t$ also increase.

For the DALES numerical experiments including the residual layer, a rapid increase in boundary-layer depth is obtained (similar to observations) when the residual layer is incorporated into the mixed layer. In contrast, the boundary-layer depth for the numerical experiments without residual layer grows at a lower rate, underestimating the observed z_1 by several hundred meters until 13:00 UTC.

Subsidence also plays an important role in the evolution of the CBL. Without subsidence included in the simulations, the simulated boundary-layer depth continues to grow, reaching higher values than those observed. Moreover, different initializations of subsidence are compared: DALES with a simple vertical profile and MLM with a subsidence value defined at the top of the CBL. The evolution of the boundary-layer depths are similar with both initializations, and in agreement with the observations, verifying the practicality and effectiveness of simpler models.

DALES allows us to evaluate the influence of the residual layer in the TKE budget during the morning (08:30–09:00 UTC). When the residual layer is taken into account, buoyancy, transport-pressure and dissipation are the largest terms before including the residual layer. When it is incorporated into the mixed layer, buoyancy and shear increases at the inversion and near the surface. On the contrary, if the residual layer is not considered, TKE terms present the typical evolution during boundary-layer growth (Pino and Vilà-Guerau de Arellano, 2008).

The effect of subsidence in the evolution of the TKE terms is less pronounced. Subsidence influence is restricted to the upper part of the mixed layer and to the entrainment zone. In this region the effect of subsidence can be clearly observed in the buoyancy and pressure-transport terms. Subsidence decreases the turbulence production, leading to a decrease in buoyancy in the upper mixed layer, but it increases the contribution of the pressure-transport term.

Regarding the vertical integration of the TKE-terms, the differences between the numerical experiments with or without residual layer are mainly due to the shear term. During the first hours of the simulations, the difference in the shear term (larger for nRL numerical experiments) is related to the different prescription of the initial wind profile. Afterwards, the normalized integrated S-term decreases for nRL, mainly because entrainment shear decreases. On the contrary, the S-term increases in the RL because larger surface shear is simulated as the wind speed in the boundary layer increases due to its initial wind profiles.

We also analyze the influence of the residual layer in the evolution of the CO_2 mixing ratio by using the observations. Before 09:00 UTC, CO_2 surface fluxes are small, the boundary layer is shallow, and the CO_2 mixing ratio decrease is mainly driven by CO_2 entrainment flux. After the inclusion of the residual layer into the mixed layer, the boundary-layer depth is almost constant during the

rest of the day. Therefore CO_2 entrainment flux is very small and, despite the larger observed CO_2 surface flux observed over some surfaces, the CO_2 mixing ratio is very similar over the different land uses. This is because the storage term is below 0.5 ppm h^{-1} over all the surfaces, due to the large value of z_1.

We can conclude that a precise definition of the characteristics of the residual layer is fundamental, even though it is complex because the evolution of the main variables in the residual layer during the previous night depends on different factors, such as advection or subsidence, which can change over time.

Chapter 4

Countergradient heat flux observations during the evening transition period

[1]

  Gradient-based turbulence models generally assume that the buoyancy flux in the surface layer of the atmospheric boundary layer ceases at the same time the local virtual potential temperature gradient changes sign. Here, we hypothesize that during the evening transition a delay exists between the instant when the buoyancy flux goes to zero and the time when the local gradient of the virtual potential temperature changes sign. This phenomenon is studied using a range of data collected over several IOPs during the BLLAST field campaign. The focus is mainly on the lower part of the surface layer using a tower instrumented with high-speed temperature and velocity sensors.

  The results from this work confirm and quantify a flux-gradient delay. Specifically, the observed values of the delay are ∼30 to 80 min. The existence of the delay and its duration can be explained by considering the convective time and the competition of forces associated with the classical Rayleigh-Bénard problem. This combined theory predicts that the last eddy formed should produce a delay when the sensible heat flux changes sign during the evening transition. It appears that this last eddy is decelerated through the action of turbulent momentum and thermal diffusivity, and that the delay is related to the convective turnover time. Observations indicate that, as horizontal shear becomes more important, the delay time apparently increases to values greater than the convective turnover time.

4.1   Introduction

The general behavior of the diurnal cycle of the ABL under clear sky fair weather conditions is well-known (Stull, 1988). During the day, a convective boundary layer driven by surface and entrainment fluxes exists (Moeng and Sullivan, 1994; Sorbjan, 1996; Sullivan et al., 1998; Pino et al., 2003; Fedorovich et al., 2001). Late in the afternoon, due to radiative cooling of the ground, an SBL, where turbulence may be suppressed, is created adjacent to the earth's surface (Nieuwstadt, 1984; Mahrt, 1998; Beare et al., 2006a). An RL of weak turbulence exists above this SBL. The RL occupies a similar space as the mixed layer of that day's CBL. However, the details of certain processes, particularly those associated with non-stationary transitional periods, are not as well understood. The transition occurring after the peak in solar insulation can be divided into distinct periods (see Section 1.4): the *afternoon transition*, when the surface sensible heat flux starts to decrease from its midday maximum, and the *evening transition*, when the surface sensible heat flux becomes negative (Nadeau et al., 2011).

This chapter focuses on the behavior of the buoyancy flux and temperature gradient in the surface layer during the early and late evening transition periods by analyzing measurements obtained during the BLLAST field campaign (Lothon and Lenschow, 2010; Lothon et al., 2014).

The hypothesis of this chapter is that during the evening transition, a delay exists between the instant when the buoyancy flux goes to zero and the time when the local gradient of the virtual potential temperature changes sign. Ghan (1981) and Franchitto and Rao (2003) attempted to find a relationship between the temperature gradient and the heat flux, considering the complete cycle. They analyzed the correlation between temperature gradient at 1000 hPa and heat flux in the northern and southern hemispheres.They observed a high and positive correlation in the northern hemisphere. Moreover, non-local model studies were used to develop different theories about the eddy diffusivity and countergradient transport, which can affect this relation (Deardorff, 1972; Holtslag and Moeng, 1991). Nonetheless, it is normally assumed that the buoyancy flux ceases to introduce heat into the ABL at the same instant that the gradient of the virtual potential temperature reflects this phenomenon. Most simulation models work using this basic concept. A good knowledge of the phenomenon and evolution of the afternoon/evening transition is crucial for developing more realistic models and creating better approximations (Sorbjan, 1997; Cole and Fernando, 1998; Edwards et al., 2006; Angevine, 2008; Nadeau et al., 2011).

Some investigations (Grimsdell and Angevine, 2002; Pino et al., 2006b), reflect a continuation of heating after the sensible heat flux becomes negative from the upper part of the atmosphere via entrainment process. However, no other in-depth studies focusing on the reaction of the surface layer during this transition has ever been reported.

The objective of this chapter is to investigate this phenomenon using a range of data collected over several days, focusing mainly on the lower surface layer, using a tower instrumented with a fast response of fine wire thermocouple (FW)

and sonic anemometers (SA). Moreover, the hypothesis will be supported by theories that can explain this phenomenon, such as the inverse Rayleigh-Bénard problem, the effect of convective time or the definition of convection characteristics with the help of the Monin-Obukhov length.

4.2   Background theory

The hypothesis, which was described in the introduction, can be related to the well-known Rayleigh-Bénard (R-B) problem (thermal instability) associated with the heating of a quiescent layer of fluid, from below which ultimately results turbulent free convection (Kundu and Cohen, 2010). The standard R-B problem is based on the idea that there is a layer of fluid heated from below. However, the upper part of the layer is heavy enough to stifle the convective movements. Both viscosity and thermal diffusivity make it difficult for convection movements to happen. Therefore, large temperature gradients are required to create the instability that makes movement possible. Here we consider similar physics, but in the opposite sense because during LAT the CBL is cooled from below. The idea was previously introduced and experimentally studied by Cole and Fernando (1998), who designed a laboratory water tank experiment to observe the decay of temperature and velocity fluctuations in the CBL in response to cooling of the surface. They observed discrepancy between their laboratory results and atmospheric observations mainly due to the presence of stratication.

In both the classical R-B problem and the phenomena studied in this chapter, a delay exists that is related with the buoyancy flux at the surface and convective movements. When the buoyancy flux ceases, the convective movements continue for some time. This delay can be similarly produced from the same factors that drive the classical R-B problem. In other words, the viscosity and the thermal diffusivity make it possible for this transition to happen in a smoother way. The dimensionless parameter, which compares the destabilizing forces (buoyancy forces) with the stabilizing forces (viscosity and thermal diffusivity), is the Rayleigh number,

$$Ra = \frac{g\Delta\overline{\theta_v}d^3}{\overline{\theta_v}\kappa\nu}, \tag{4.1}$$

where g is the gravitational constant, $\Delta\overline{\theta_v}$ is the average virtual potential temperature difference over the layer depth d (assumed here equal to the height of the atmospheric near-surface layer), κ is the molecular thermal diffusivity, and ν is the molecular kinematic viscosity. For the classical R-B problem with heating from below, when the Rayleigh number reaches a critical value, Ra_{cr}, convective movements start. In this chapter, we provide preliminary evidence for a transitional turbulent Rayleigh number at which convective motions cease.

4.3 Methodology

4.3.1 Observations

This study was performed within the framework of the BLLAST field campaign. Amongst the wide range of instruments deployed during the campaign, a relatively short (10 m), but highly instrumented mast was selected to be used in this study. The main characteristics of this mast are described in Table 2.3. The sensors deployed on the mast included SA and FWs. The instrument-deployment strategy placed many sensors close to the ground in order to observe small and fast changes in temperature and wind. Figure 4.1a shows the vertical location of the instruments on the 10 m mast, and Fig. 4.1b shows an aerial view of the site where the mast was located.

Four Campbell Scientific sonic anemometer thermometers (CSAT3, Logan, UT) –fitted with 12.7 μm diameter Campbell Scientific E-TYPE model FW05 fine-wire thermocouples– were mounted at the following heights: 2.23, 3.23, 5.27 and 8.22 m above ground. Closer to the ground, there were four additional FW05 sensors mounted at 0.091, 0.131, 0.191, and 0.569 m above ground. The lowest sensor was placed just in the grass canopy. The grass around this sensor was regularly trimmed to maintain a canopy height of approximately 7-9 cm. Sensors collected data from 1 June 2011 to 6 July 2011. During the IOPs, the lowest FWs were installed in the afternoon to provide an expanded dataset. All instruments recorded data at 20 Hz. However, 5-min block-averaged data are presented in the analysis here. All data were processed using the software package *EC-pack* (Van Dijk et al., 2004).

4.3.2 IOP analysis procedure

This study focuses on the analysis of the following group of IOP days (when the 10 m mast was completely instrumented) during the BLLAST campaign: 24, 25, 27, 30 June and 1, 2 July 2011. Table 4.1 summarizes the information used to characterize the IOPs, including the daily maximum kinematic heat flux, the duration of the diurnal cycle (positive surface heat flux period), and the days from the last rainfall.

The primary goal is to characterize and understand the observed time delay between the instant when the buoyancy flux is zero and when the virtual potential temperature gradient changes sign. To illustrate the change of gradient sign of the virtual potential temperature, Fig. 4.2 shows the temporal evolution of the vertical profile of potential temperature measured by the FWs located at the 10 m mast during the evening of 1 July 2011. We can observe how, at the lowest levels, the gradient of potential temperature changes sign from negative to positive.

The instrumentation used in the campaign included fewer SA than FW thermocouples, so the instruments were not always collocated. However, to include the effects of humidity, we use the measurements made by the SA located at 2.23 and 3.23 m, because these are the lowest sensors which can be used to
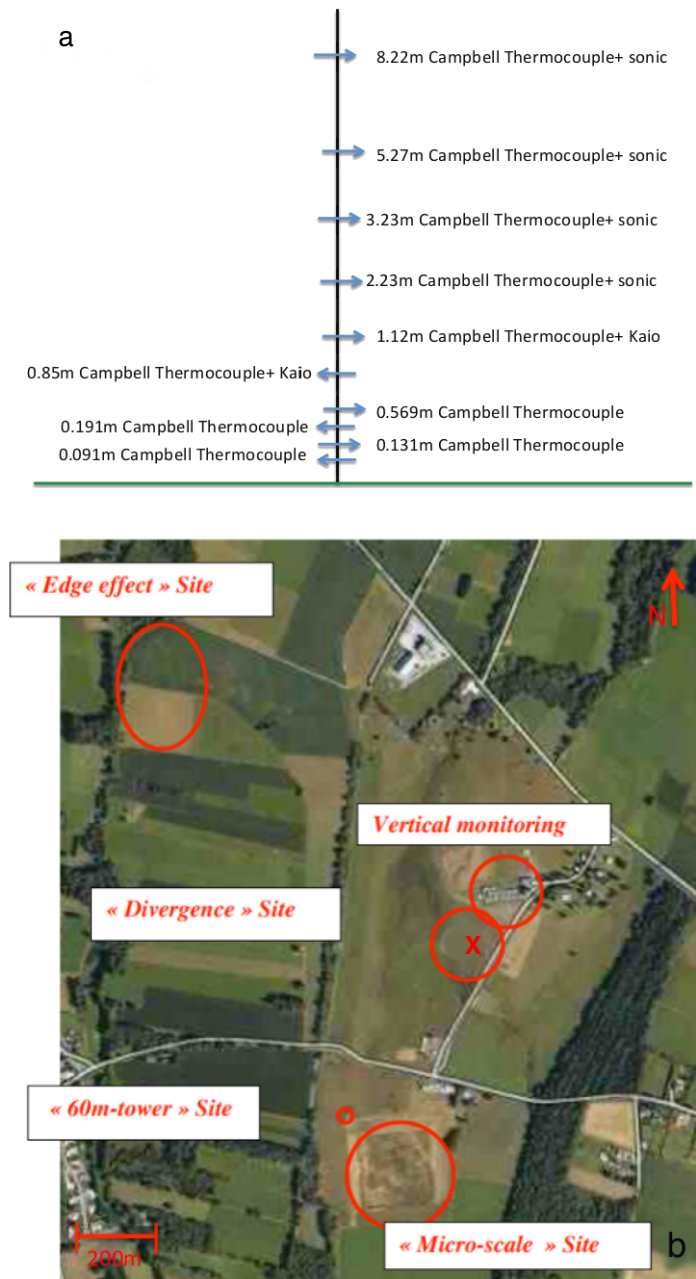
Figure 4.1: (a) Sketch of the distribution of sensors that were deployed on the 10 m mast during BLLAST and (b) an aerial view of the site (the red X indicates the location of the 10 m mast). Kaijo-Denki data had some errors and we did not use the measurements of this sensor in the development of this thesis.

Table 4.1: Based on the observations taken at BLLAST campaign: IOP date, kinematic heat flux (H), length of the day, sunset time, days from last rainfall, delay time (DT), convective time (t_*), convective intensity, transitional turbulent Rayleigh number (Ra_{t}) and temporal difference between the time when Ra and buoyancy flux change signs (Ra_t−BF).

Day (IOP)	H_{max} (K m s^{-1})	Diurnal cycle (h)	Sunset (UTC)	Days from last rainfall	DT (min)	t_* (min)	$-z/L$	Convective intensity	Ra_t	Ra_t-BF (min)
24 June (IOP4)	0.18	13.3	19:42	1	38	36	0.297	Strong	9.89	49
25 June (IOP5)	0.158	12.8	19:42	2	48	26.37	0.102	Weak	1.097	90
27 June (IOP7)	0.1	10.25	19:42	4	72	42	0.1205	Weak	3.62	95
30 June (IOP8)	0.11	12.16	19:42	1	30	27	0.289	Strong	10.32	34
1 July (IOP9)	0.138	12.8	19:41	2	40	33	0.22	Moderate	5.01	55
2 July (IOP10)	0.14	11.3	19:41	3	42	55.8	0.24	Moderate	4.5	53
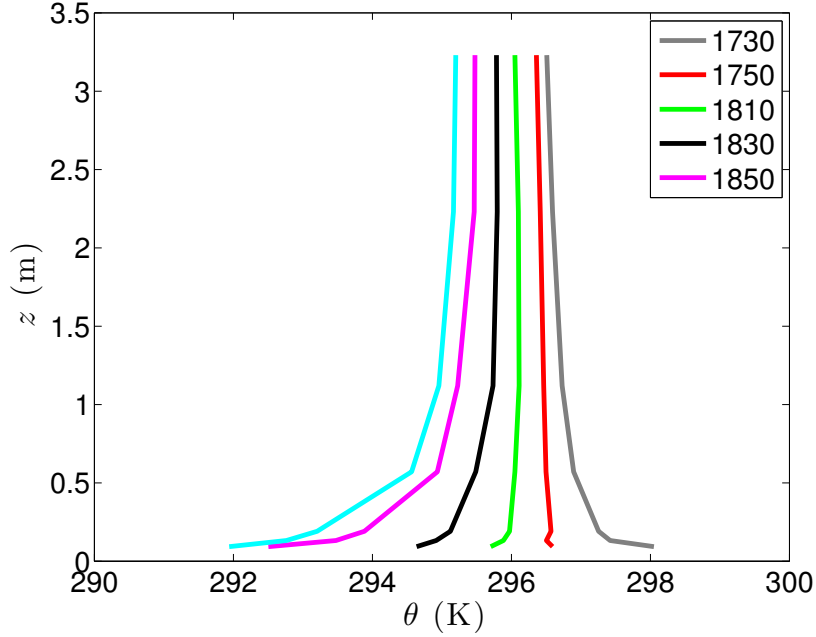
Figure 4.2: Observed 5–min averaged vertical profile of potential temperature during the evening transition on 1 July 2011 from FW measurements.

simultaneously measure virtual potential temperature gradients and buoyancy flux.

To estimate the virtual potential temperature (θ_v), we assume that the virtual temperature (T_v) can be approximated by the sonic temperature. The virtual potential temperature is then estimated using the adiabatic lapse rate (Γ) as follows: $\theta_v = T_v + \Gamma z$. Gradients are then computed using finite differences (Chapra and Canale, 1998).

The following paragraphs describe how this delay is determined. Figures 4.3a and b show the observed temporal evolution of θ_v at 2.23 and 3.23 m during two IOPs, and they illustrate the time when the change in sign occurs in the difference between the virtual potential temperature at the two levels. The change in sign of the gradient first occurs at 18:36 UTC for 30 June 2011, and again at 18:51 UTC on 1 July 2011.

The buoyancy flux was computed using:

$$BF = \frac{g}{T_v}\overline{\omega'\theta'_v}. \tag{4.2}$$

Here, $\overline{\omega'\theta'_v}$ is the vertical kinematic flux of virtual potential temperature. The lowest sensor measuring temperature and the vertical component of the wind (2.23 m) is used to define when the buoyancy flux ceases; in other words, when there is no more heat coming from the ground being measured by that probe.
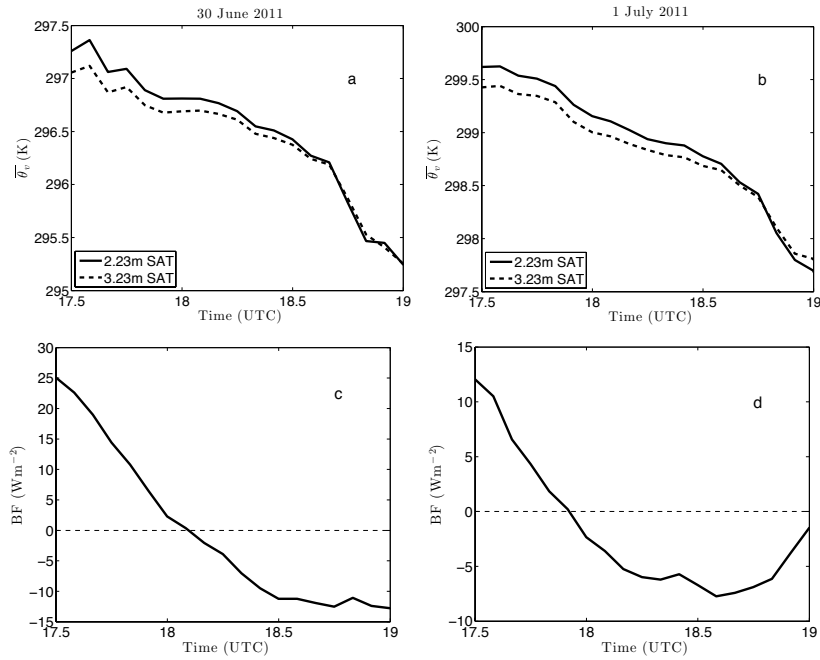
Figure 4.3: Observed temporal evolution of the virtual potential temperature at 2.23 m (solid line) and 3.23 m (dashed line) during the evening transition on (a) 30 June and (b) 1 July 2011, and the observed temporal evolution of the buoyancy flux at 2.23 m during the evening transition on (c) 30 June and (d) 1 July 2011.

Figures 4.3c and d show the temporal evolution of the buoyancy flux from 17:30 UTC to 19:00 UTC on 30 June 2011 and on 1 July 2011, respectively. For these two IOPs, the lower sensor shows that the flux ceases at ≈18:18 UTC and 17:54 UTC. The delay time between when temperature gradient and buoyancy flux change signs is then simply the difference between the two times.

To develop the theory for the inverse R-B problem, the area selected is the lower surface layer, specifically from 2.23 to 8.2 m, which is the area with an evolution closer to the idea proposed by Bénard that we could obtain by using the instruments deployed at the campaign sites. First, we calculate the turbulent thermal diffusivity (K_H) and the turbulent viscosity (K_M). These two parameters can be estimated using the following equations:

$$K_H = \overline{\omega'\theta_v'}/\frac{\partial\overline{\theta_v}}{\partial z}, \tag{4.3}$$

$$K_M = -u_*^2/\frac{\partial\overline{s}}{\partial z}, \tag{4.4}$$

where u_* is the friction velocity, calculated by using the momentum fluxes measured at 2.23 m, and $\overline{s}$ is the mean wind speed. There is relatively little variability in these parameters before buoyancy flux ceases (not shown). Therefore, they are estimated when the maximum buoyancy flux occurs, in order to avoid possible influences of the skin flow close to the afternoon transition as well as to be consistent during all IOPs.

4.4 Results and discussion

4.4.1 Delay time analysis

Using the procedure described above, the delay time (DT) was computed for all IOPs. The results are summarized in Fig. 4.4, where the instants when the buoyancy flux and the virtual potential temperature gradient change signs are shown. As is shown in the figure, this delay was present on all days analyzed. The delay varies from around 30 to 80 minutes . The numerical values for the delay time for all IOPs are given in Table 4.1.

A possible explanation for the occurrence of this delay can be related to eddy movements associated with warm air plumes that form at the surface. The moment that the buoyancy flux transitions from positive to negative values indicates that no more heat is being introduced to the atmosphere from the ground. Additionally, the upward movement due to warming of the air next to the ground (formation of new thermal plumes) also stops. However, these movements are not instantaneous movements. Quite the opposite, these movements start at the ground, mix through the surface layer and potentially move upward, crossing the entire boundary layer up to the entrainment zone and then descend with the warm air introduced by the overshoots of the eddies in the free atmosphere (i.e., the movements act over an eddy turnover period of time). When
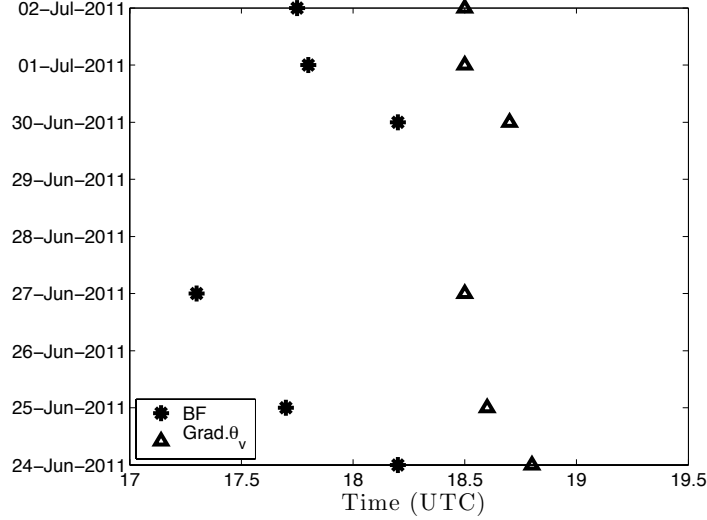
Figure 4.4: For each IOP, instant when buoyancy flux (asterisks) and virtual potential temperature gradient (triangles) change sign.

the introduction of heat stops ($BF = 0$ W m^{-2}), the last eddy forms and continues to move through the boundary layer. This hypothesis is compatible with the existence of a neutral layer above the decoupled stable surface layer, where, due to entrainment, turbulence may still exists (demixing process) (Nieuwstadt and Brost, 1986; Grimsdell and Angevine, 2002; Pino et al., 2006b). During this eddy turnover time period, the surface layer cools, changing the sign of the temperature gradient. Consequently, the surface layer does not instantaneously respond when the surface flux stops, because the mixing (and heat transfer) continues during one eddy turnover time. This idea has been presented in different studies, for instance by Sorbjan (1997), although it focuses mainly on movements in the entrainment zone and not at the ground.

An analysis of the dimensionless temperature gradient (ϕ_h), as described by Monin-Obukhov Similarity Theory (MOST), was used to investigate the presence of this delay. The Monin-Obukhov length scale (L) can be used as a scaling parameter to define the convective characteristics of the atmospheric boundary layer. Using this parameter, the effects of buoyancy and mechanical production of turbulence can be compared close to the ground at 2.23 m. The surface layer scaling parameter ($-z/L$) provides a metric indicating the strength of the convective conditions during the IOP period and leading into the evening transition. We computed ϕ_h and $-z/L$ as follows:

$$\phi_h = \frac{kz}{\theta_{v*}^{SL}} \frac{\partial \theta_v}{\partial z} = \frac{kzu_*}{-\overline{w'\theta_v'}|_{\mathrm{s}}} \frac{\partial \theta_v}{\partial z}, \tag{4.5}$$

$$-\frac{z}{L} = \frac{kzg\,\overline{w'\theta_v'}|_s}{\overline{\theta_v}u_*^3}. \qquad (4.6)$$

where k is the von Karman constant, z is the analysis altitude (2.23 m).

Figure 4.5 shows every 5-min ϕ_h as a function of $-z/L$ at 2.23 m for 30 June 2011 and 1 July 2011. Clearly, there are points which break away from MOST (indicated by the dashed black line). Specifically, gradient-theory fails locally due to the countergradient observations that appear in the plots during near stable conditions. Taking into account our hypothesis as the buoyancy flux in the surface layer of the atmospheric boundary layer ceases at the different time as changes in sign of the local virtual potential temperature gradient some negative values of ϕ_h appear in the figure.
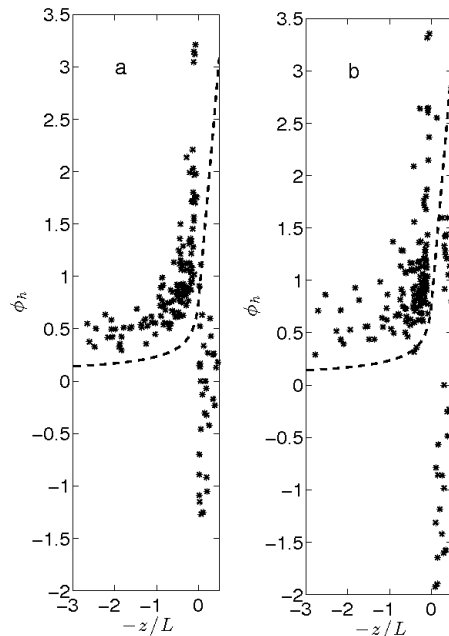
Figure 4.5: Dimensionless temperature gradient (ϕ_h) as a function of $-z/L$ at 2.23 m on (a) 30 June and (b) 1 July 2011. Dashed line is the approximation of Businger et al. (1971).

Formally, MOST should be valid in the stable layer. However, during the transition period, one can observe that the log surface layer locally disappears close to the ground, as there is a decoupling between the old log-layer and the newly forming stable layer, as shown in the transitioning temperature profile in Fig. 4.2. In the past, this phenomenon was mainly observed for the air-sea boundary layer (Sahlée et al., 2007). However, Smedman et al. (2007) also observed this behavior at a site over land, but for atmospheric conditions that were quite different from our study case. In particular, their case was for strong

winds between 7-10 m s^{-1}, in contrast with the calm BLLAST conditions.

4.4.2   Convective time analysis

To provide support to our delay hypothesis, the convective time is analyzed and compared to the delay time. The convective time can be defined as the approximate time that it takes one eddy to traverse the atmospheric boundary layer. The hypothesis described above should be supported if the value of the delay and the value of the convective time are similar. In other words, the delay exists as a result of the continued movement of the boundary layer due to the last eddy motions generated at the surface.

It should be noted that there is debate in the research community regarding the use of various times during the transition period. There is not a general agreement about which scaling time is the best option during afternoon/evening transition, as described in section 2.1 (Nieuwstadt and Brost, 1986; Lothon et al., 2014).

First, the convective time (t_*) is computed following (Deardorff, 1972):

$$ t_* = \frac{z_1}{w_*}, \quad \text{where } w_* = \left[\frac{g z_1}{\overline{\theta_v}} \overline{w'\theta'_v}|_s \right]^{\frac{1}{3}}, \tag{4.7} $$

with z_1 being the boundary-layer depth. These scales are then computed averaging the 5 min periods just before the buoyancy flux vanishes. The depth of the boundary layer was obtained from the BLLAST campaign's UHF profiler installed in Supersite 1. Specifically, we estimate the height of the ABL from the local maxima of the refractive index structure coefficient (see section 2.3.1.2).

The results from the calculation of the convective time for all IOPs are shown in Table 4.1 and Fig. 4.6. It is clear that the delay time and the convective time compare better on some IOPs than others. For some IOPs, such as 24 June 2011 and 30 June 2011, the delay time is nearly the same as the convective time. However, on other days, such as 25 or 27 June, the convective scale and delay time compare quite poorly.

These observed differences between the time could be a result of the characteristics of the boundary layer associated with the different IOPs that are not accounted for in the assumptions associated with the convective time. In other words, IOPs associated with very convective conditions seem to follow the theory better, while more synoptically forced atmospheric conditions fail.

4.4.3   Monin-Obukhov length analysis

In contrast to section 4.4.1, here we compute a characteristic surface layer scaling parameter ($-z/L$) for each of the IOPs by averaging it over the time period prior to the main evening transition (from 1200 UTC to 1645 UTC). We compute $-z/L$ during this period to avoid *BF=0 W m^{-2}* and to include the decay of the buoyancy flux the afternoon transition. From the results, we observe that each IOP can be classified as a strong, moderate or weakly convective day
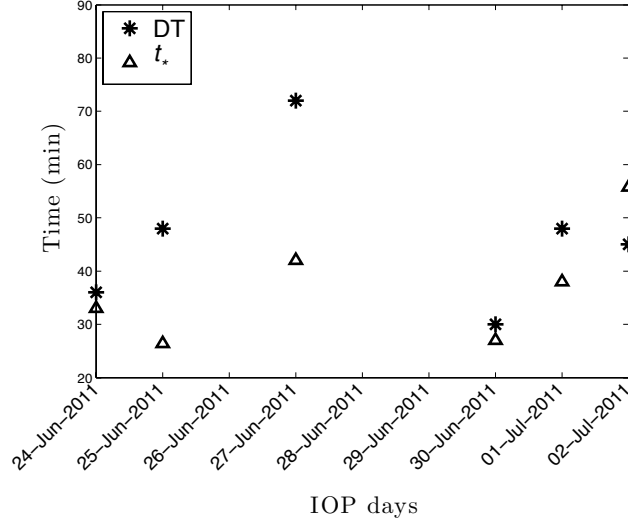
Figure 4.6: Delay time (asterisk) and convective time scale (triangles) for each IOP.

(see Table 4.1). The most convective IOPs were 24 and 30 June 2011 which are post-frontal days. These IOPs were also those with a better correlation between the delay time and the convective time (see Fig. 4.6 and Table 4.1). On the other hand, the weaker convective days (i.e., 25 and 27 July 2011) show greater differences between the delay and convective times (see Table 4.1). Less convective days have higher values of u_* as a result of increased mechanical turbulence being produced close to the ground. On these weakly convective days, proposed explanation can be that the delay time is increased as shear prevents the rapid onset of a stable boundary layer at the surface.

Figure 4.7 shows the difference between the two times as a function of $-z/L$. Evidently, the BLLAST data indicate an exponentially decreasing relationship between the differences of time and the Monin-Obukhov parameter. This relationship is likely to be a function of local effects, and should be investigated at other sites to see if a general relationship can be ascertained. BLLAST field campaign did not have any other site with a similar sensor distribution. Therefore, we encourage to take into account this phenomenon in the planification of future field campaigns. Regardless, Fig. 4.7 shows a potentially site-specific method for forecasting the delay time using data from 1200 UTC to 1645 UTC of the single-flux mast.

4.4.4 Turbulent Rayleigh number analysis

The turbulent Rayleigh number (Ra_{turb}) can be used to explain the behavior of the delay time. It is calculated with Eq. 5.2; but instead of using molecular
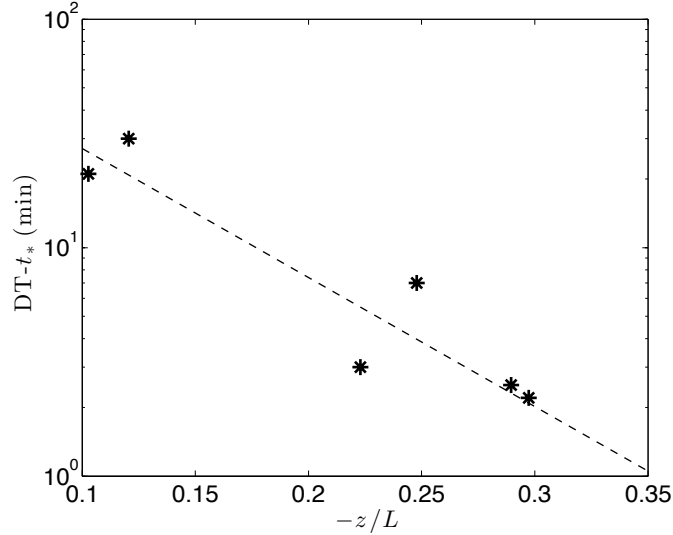
Figure 4.7: For all the IOPs, difference between the delay and convective times as a function of $-z/L$.

thermal diffusivity (κ) and molecular kinematic viscosity (ν), we use the turbulent thermal diffusivity (see Eq. 4.3) and turbulent viscosity (see Eq. 4.4). Therefore, Ra_{turb} reads:

$$Ra_{turb} = \frac{g}{\theta_v} \frac{\Delta\overline{\theta_v}d^3}{K_H K_M} = -\frac{g}{\theta_v} \frac{(\Delta\overline{\theta_v})^2 \Delta\overline{s}d}{\overline{w'\theta_v'}u_*^2}, \tag{4.8}$$

where d is the distance between the sensors (8.2-2.23 m), $\overline{\theta_v}$, $\overline{w'\theta_v'}$ and u_* are measured at 2.23 m, and all the differences are calculated by using the measurements recorded at the sensors located at those two heights. We select these two sensors because this area presents an evolution closer to the idea proposed by Bénard, as similar as possible to the surface layer. Turbulent thermal diffusivity and turbulent viscosity could play a role in the initiation or the ceasing of convection. We define the transitional turbulent Rayleigh number (Ra_t) as the value of Ra_{turb} when the buoyancy flux ceases (0 W m^{-1}). Figure 4.8 shows the temporal evolution of buoyancy flux and Ra_{turb} from 17:00 to 20:00 UTC on 30 June and 1 July 2011. As can be observed, Ra_{turb} becomes negative later on 1 July 2011 similarly to the changes in sign of the local virtual potential temperature gradient. Ra_{turb} remains smoothly positive around zero buoyancy flux because we apply a filter for really large numbers. For all the analyzed days, BF is negative several tens of minutes before Ra_{turb}. Table 4.1 shows this temporal difference and the value of Ra_t. As can be observed, this temporal difference is clearly related with DT being larger on the days with a larger temporal difference between Ra_t and BF.
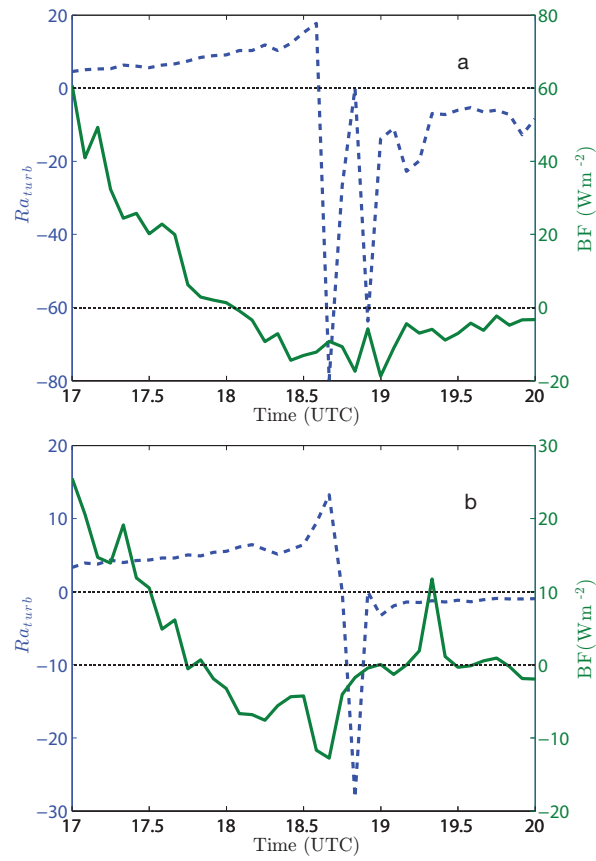
Figure 4.8: Temporal evolution of buoyancy flux at 2.23 m (green) and Ra_{turb} (blue) during the evening on (a) 30 June and (b) 1 July 2011.

We assume that, on each day, Ra_t corresponds to the critical Rayleigh number (Ra_{cr}). It is important to notice that during early morning, on those days with large values of Ra_{cr}, larger values of buoyancy flux are needed for the onset of convection (Stull, 1988). Additionally, during the evening transition on these days, convection stops quickly when the buoyancy flux ceases. By assuming $Ra_t \propto Ra_{cr}$, larger values of Ra_t have to be observed on these days. Figure 4.9 shows $DT-t_*$ as a function of Ra_t for all the studied days. There is an exponentially decreasing relationship between both parameters. IOPs with larger Ra_t have a smaller difference between the convective and the delay time, meaning convection stops quickly. In contrast, on those days with low values of Ra_t, their convection slowed down smoothly, which increased the delay time and, consequently, $DT-t_*$.
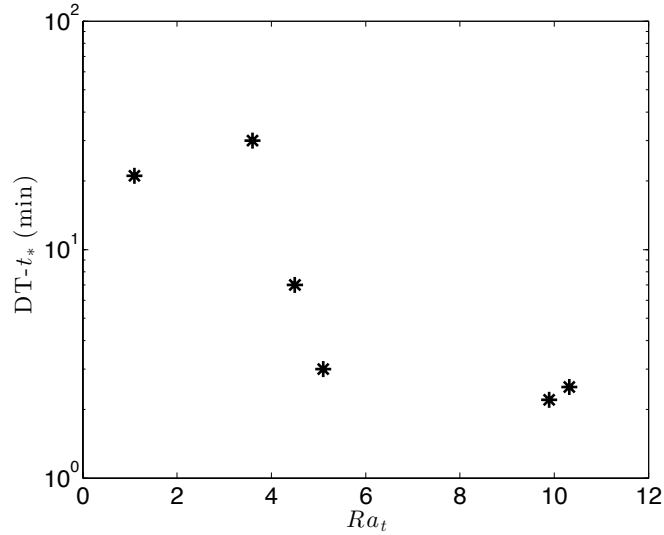
Figure 4.9: For all the IOPs, difference between the delay and convective times as a function of transitional turbulent Rayleigh number (Ra_t).

4.5 Conclusions

It has been shown that there is a clear failure of flux gradient theory during the evening transition period as a result of non-local processes. Analysis of the data obtained from a 10 m mast during the BLLAST campaign indicates that a delay time exists between the time when the buoyancy flux ceases and the change in sign of the vertical gradient of the virtual potential temperature. This was the case for all IOPs.

For strong to moderate convective days, the delay time is relatively short ($\sim$ 30-40 minutes), and it corresponds closely to the time associated with the last eddy movement. In other words, it is similar to the convective time. On the other hand, when midday convection is weaker, mechanical forces play a much larger role, resulting in greater friction velocity. In these cases, the delay time is greater, due to the increase in horizontal turbulence. The data show that the difference between the delay time and the convective time exponentially depends on the Monin-Obukhov parameter $-z/L$. If found to be generalizable, this relationship could be used to help forecast the delay time using midday measurements (for days where large scale forcing changes slowly).

Finally, we have defined a transitional turbulent Rayleigh number (Ra_t) associated with the buoyancy flux ceasing. We observe that higher values of Ra_t are related with faster decay in convection. Otherwise, turbulent viscosity and thermal diffusivity help to slow down the last eddy movement and increase the delay time when we observe low values of Ra_t.

Chapter 5

Lifted temperature minimum during evening transition

Lifted Temperature Minimum (LTM) was first reported by Ramdas and At-manathan (1932) during the night. It was defined by the existence of a tem-perature minimum some centimeters above the ground. During the following decades, several research studies analyzed this phenomenon, verifying its exis-tence and postulating different hypotheses about its origin.

The aim of this chapter is to study the existence and characteristics of LTM during the evening transition by using observations obtained during the BLLAST campaign. The data was obtained by: two masts instrumented with several ther-mocouples and wind sensors at different heights close to the ground; and a mast with radiometers for studying the role of mechanical turbulence and radiation in the development of LTM.

The study shows that LTM can be detected in calm conditions already dur-ing day–night transition, several hours earlier than the usual time of occurrence reported by previous works. These conditions are fulfilled when weak synoptic forcing exists and the local flow shifts from valley to mountain breeze in a rela-tively complex orography. Under these special conditions, turbulence becomes a crucial parameter to determine the ideal conditions for observing LTM.

Additionally, the correlation of long wave radiation measured at 0.8 m and estimated at the ground varies when the LTM is observed. Therefore, LTM is also related to a change in the atmospheric radiative characteristics under calm conditions.

5.1   Introduction

Lifted Temperature Minimum (LTM) is characterized by an elevated tempera-ture minimum close to the surface. Depending on the ground characteristics, it is typically located at levels between 0.1 and 0.5 m. After sunset, if cloudless and calm conditions exist and ground and air emissivities have close values, the

layer just above the ground can cool radiatively faster than the ground, and a minimum appears several centimeters above the surface. LTM has been studied by means of observations (Ramdas and Atmanathan, 1932; Lake, 1956; Raschke, 1957; Oke, 1970), numerical simulations (Zdunkowski, 1966; Vasudeva Murthy et al., 1993; Narasimha and Vasudeva Murthy, 1995; Vasudeva Murthy et al., 2005) and laboratory experiments (Mukund et al., 2010, 2013).

Ramdas and Atmanathan (1932) provided for the first time a detailed description of the unexpected temperature minimum neglecting advective effects and suggested some interesting problems regarding the role of radiation from the ground and the lower layer of the atmosphere. Several years later, Lake (1956) and Raschke (1957), used more complex instruments to confirm the results obtained by Ramdas and Atmanathan (1932), discarding instrumental errors. Raschke (1957) took measurements over different terrains to also verify that LTM was not produced by advection and defined three different profiles of temperature, distinguishing between profiles with the minimum temperature at the ground, LTM profiles and profiles with advection. Additionally, he made measurements at different latitudes to prove that the phenomenon was not restricted to the tropics. In contrast, Geiger (1957) showed some skepticism about the existence of LTM. Narasimha and Vasudeva Murthy (1995) considered the question why LTM is not overturned by convective instability, and he was also concerned about the precision of the measurements close to the ground. Later on, Zdunkowski (1966) suggested the existence of a haze layer near the ground to explain the appearance of the LTM. Nevertheless, this approach was discarded, because this layer was never observed, and the thermal diffusivity required for its explanation was not realistic (Narasimha and Vasudeva Murthy, 1995).

More recent studies have shown that LTM profiles are common over different natural (bare soil, snow and short grass) (Oke, 1970) as well as artificial surfaces (concrete or foam) (Mukund et al., 2010, 2013). Mukund et al. (2013) studied in detail the importance of surface characteristics for the appearance of LTM. They demonstrated, by studying LTM over different surfaces (aluminum, foam and concrete), that decreasing surface emissivity increases the intensity of LTM and the near-ground temperature gradient. Lower surface emissivity can help to change the temperature profile with the minimum temperature at the ground to an LTM profile. Therefore, terrains with an emissivity close to the air emissivity favor LTM appearance. Narasimha (1991) and Narasimha and Vasudeva Murthy (1995) summarized the main mechanisms related to the occurrence of LTM. Narasimha (1991) considered that radiative cooling depends on ground emissivity and the air emissivity gradient. When the air emissivity gradient is large, the temperature of the air close to the ground decreases faster than the temperature of the ground and LTM can be observed. Although the model presented a detailed solution for the air temperature evolution by considering surface emissivity, ground cooling and turbulence, it did not include a detailed discussion of the energy budget near the ground, which was introduced afterwards by Narasimha and Vasudeva Murthy (1995).

Aside from the ground characteristics, calm conditions with low mechanical turbulence are crucial for observing LTM. For instance, LTM intensity

was weaker when large roughness length exists, because it increases both tur-
bulence and emissivity (Oke, 1970). Moreover, field measurements (Ramdas
and Atmanathan, 1932; Lake, 1956; Raschke, 1957; Oke, 1970) and models
(Vasudeva Murthy et al., 1993; Narasimha and Vasudeva Murthy, 1995; Va-
sudeva Murthy et al., 2005) show that advection was weak when LTM was
observed. LTM has been reported only in a few particular cases for friction
velocities above 0.1 m s^{-1}, but it disappears quickly (Vasudeva Murthy et al.,
2005).

Vasudeva Murthy et al. (1993) were the first ones to propose a model which
appears to be in good agreement with observations. They analyzed the impor-
tance of radiative, conductive and convective fluxes during LTM. This model
was accepted until Mukund et al. (2010) and Ponnulakshmi et al. (2012) sug-
gested that the cooling obtained by Vasudeva Murthy et al. (1993) was wrong,
due to an error introduced by the radiative balance, and they presented a new
model based on the work done by Edwards (2009), including the importance of
suspended solid or liquid particles which enhance cooling processes.

Regarding the importance of radiation in the formation of LTM, Mukund
et al. (2010) confirmed that near the surface radiative cooling can be orders
of magnitude higher than values elsewhere in the boundary layer. With really
low winds, the role played by turbulence is nearly negligible compared with
radiation. Therefore, temperature evolution is mainly governed by the radiation
timescale (Vasudeva Murthy et al., 2005). Moreover, Mukund et al. (2013)
showed that a heterogeneous distribution of the aerosol concentration can cause
hyper-cooling close to the surface, which modifies the atmospheric radiative
cooling.

Near-surface temperature inversion during daytime has only been analyzed
in specific conditions over the open Arabian Sea during the summer monsoon
season (Bhat, 2006). However, the atmospheric conditions during that study,
characterized by strong surface winds and high levels of sea salt particle con-
centration in the boundary layer, are far away from the ones presented here.

In summary, previous studies have shown that LTM intensity varies depend-
ing on surface characteristics (emissivity and thermal inertia/soil conductivity),
prevailing wind conditions (turbulence) and atmospheric radiation.

5.1.1 Objectives

In contrast to previous studies, we analyze LTM occurrence during the evening
transition. Notice that the largest radiative cooling occurs during those hours
(Sun et al., 2003).

Specifically, our research objectives can be summarized as follows:

1. To investigate the existence of the LTM during the evening transition.

2. To study the relevance of wind characteristics driven by orography.

3. To analyze the importance of turbulence to observe LTM during evening
   transition.

4. To analyze the importance of radiation in the appearance of LTM.

5.2   Measurements

To investigate LTM during the evening transition, we analyze measurements recorded during the BLLAST field experiment (Lothon et al., 2014). This campaign was performed from 14 June to 8 July 2011 in southern France, near to the Pyrenees Mountains. The campaign site extended over an area of approximately 100 km^2 covered with heterogeneous vegetation, mainly grass, corn, moor and forest.

The most salient BLLAST objective was to obtain a detailed set of meteorological observations during the evening transition to better understand the physical processes that control it. For example, improved understanding of the effects of entrainment across the boundary layer top, surface heterogeneity, horizontal advection, clouds, radiation and gravity waves on the evening transition.

During intensive observational periods (IOPs), the atmosphere was heavily probed by in situ measurements from masts, towers, tethered balloons, radiosondes and manned and unmanned airplanes, as well as remote sensing instruments such as LIDAR and RADAR wind profilers. For this paper, the near surface temperature evolution is analyzed using two masts (T1 and T2) separated by approximately 468 m.

Figure 5.1 shows a plan view of T2 area and a side view of the T1 and T2 instruments. T1 was located at *43.1275^{o}N-0.36583^{o}E* and T2 at *43.1238^{o}N-0.36416^{o}E*. T1 was a 10-m mast instrumented with four Campbell Scientific CSAT3 Sonic Anemometer Thermometers and Campbell Scientific E-TYPE model FW05 (12.7 μm diameter) Fine Wire (FW) thermocouples at 2.23, 3.23, 5.2 and 8.2 m. Closer to the ground, there were four additional FW05 FWs at 0.091, 0.131, 0.191 and 0.569 m which were only installed during the IOPs. Temperature data at T1 were recorded at 20 Hz. T2 was a 2-m mast with eight FW3 (76.2 μm diameter) FWs located at 0.015, 0.045, 0.075, 0.14, 0.3, 0.515, 1.045 and 1.92 m recording temperature data at 10 Hz. Additionally, separated approximately 2 m from T2, there was also a Campbell Scientific CSAT3 at 1.95 m, recording data at 20 Hz. To unify the measurements taken by the different instruments, all the recorded data were averaged over 5 min intervals (De Coster and Pietersen, 2011). This information was complemented with an estimation of the skin temperature provided by an Infra-red Remote Temperature Sensor IR120 pointing towards surface. This infrared camera was measuring temperature with a sampling frequency of 3 Hz before 21 June 2011 and of 1 Hz after this day.

Near T2, one Kipp&Zonen CNR1 net radiometers was installed. The CNR1 sensor is able to measure upwelling and downwelling components of both the shortwave solar (0.305-2.8 μm) and terrestrial radiation (5-50 μm) separately. Kipp&Zonen CNR1 was installed at 0.8 m above the ground.

The ground characteristics below T1 and T2 were adequate for observing LTM (Mukund et al., 2013). The ground in both cases was covered by long grass
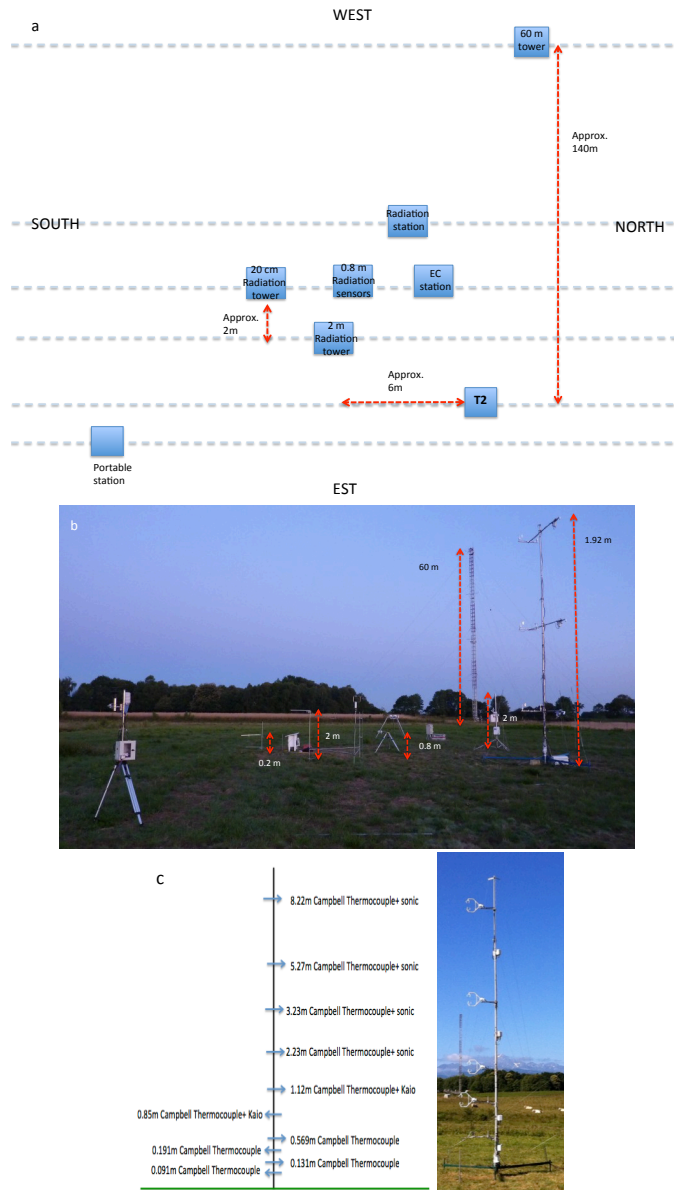
Figure 5.1: (a) Plan view of T2 area and side view of (b) T2 and (c) T1.

with an emissivity around 0.986 (Gayevsky, 1952). The grass cover had thermal conductivities of 1.1 W m^{-1} K^{-1} (Campbell and Norman, 1998). However, T2 surface had some cut grass over the terrain, which can produce some variation in the vertical profile of potential temperature.

Oke (1970) pointed out that, over grass-covered surfaces, the minimum temperature during the night can be found just above the grass instead of right at the surface. This phenomenon associated with the vegetative canopy is sometimes confused with LTM. He observed LTM at 0.02 m above the grass. In our case study, the grass height was short, around 0.03-0.07 m, and the observed LTM height occurred above 0.1 m from the ground.

From the three and a half weeks of the BLLAST campaign, we select different IOPs with data available from T1 and T2. The analysis is based on the observations taken on 24, 25, 27, 30 June and 1 and 2 July 2011. See the general description of these IOPs in Section 2.6.

5.3   Observed LTM characteristics

In general, the LTM, when it occurred, was detected and observed by both T1 and T2. Figures 5.2 and 5.3 show the lower 2 m vertical profile of potential temperature recorded at T1 (left) and T2 (right) on 24, 25, 27, 30 June and 1 and 2 July 2011.

As illustrated in Figure 5.4, three sensors on each tower were used to detect and characterize LTM profiles. First, the location of the minimum temperature was identified (base); second, the sensor located closest to the ground (LTM▼); and, finally, the sensor located just above the base sensor (LTM▲). LTM is observed if:

$$T_{\text{base}} - T_{\text{LTM▼}} < 0 \quad \text{and} \quad T_{\text{LTM▲}} - T_{\text{base}} > 0 \,. \qquad (5.1)$$

Additionally, LTM intensity is defined as:

$$\text{LTM}_{\text{intensity}} = T_{\text{base}} - T_{\text{LTM▼}} \,. \qquad (5.2)$$

Finally, LTM duration is defined as the period when the LTM conditions defined above are fulfilled. Table 5.1 shows the main characteristics of the LTM: height, intensity, and duration obtained by analyzing temperature recorded for all the IOPs at both masts.

LTM was observed during the evening transition for all the days except 27 June 2011. However, there are clear differences between the IOPs and also between the measurements at T1 and T2. LTM was detected by the sensor located at 0.131 m at T1, and between 0.075 m and 0.14 m (except on 25 June 2011) at T2. It is important to notice that, due to the vertical resolution of the measurements, the exact height of the LTM cannot be determined.

We can compare the different characteristics of each observed LTM. On 24 June 2011, LTM was reported during 20 min at T1 and during 40 min at T2. Greater LTM-intensity (0.7 K) was observed at T2 compared to T1 (0.35 K). On 25 June 2011, LTM was detected at T2 higher up, at around 0.3 m, with
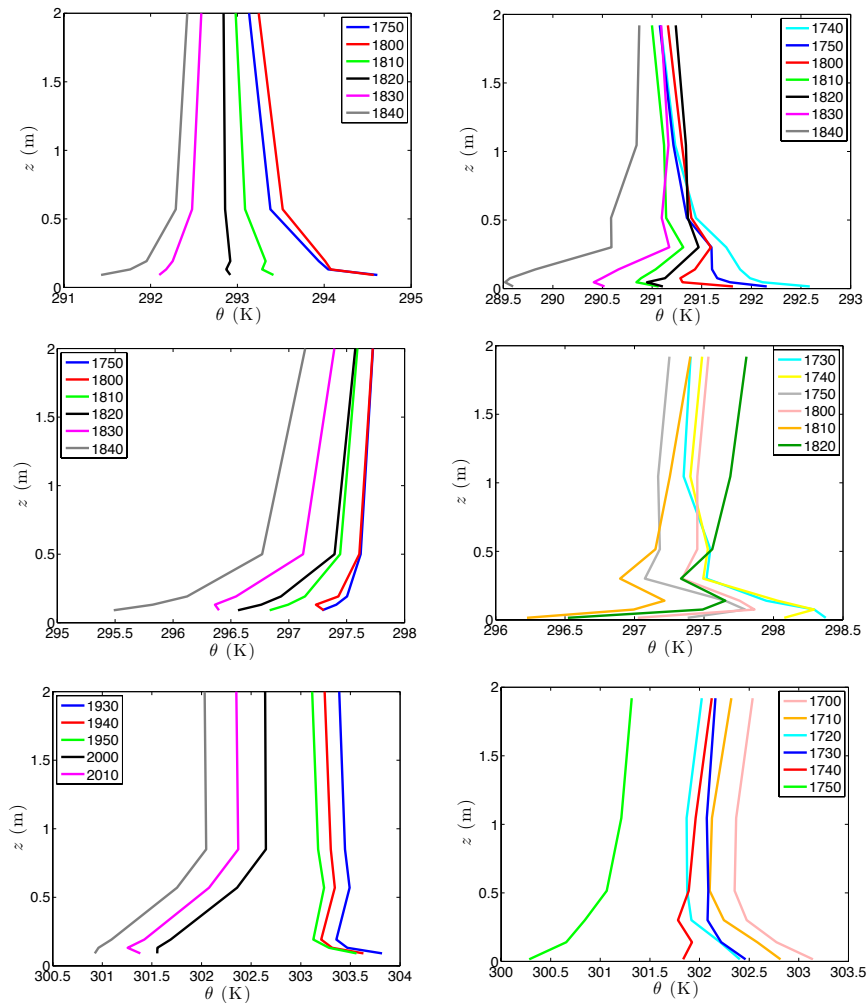
Figure 5.2: Temporal evolution of potential temperature profile on 24 June 2011 (top), 25 June 2011 (middle) 27 June (bottom) measured at T1 (left) and T2 (right).
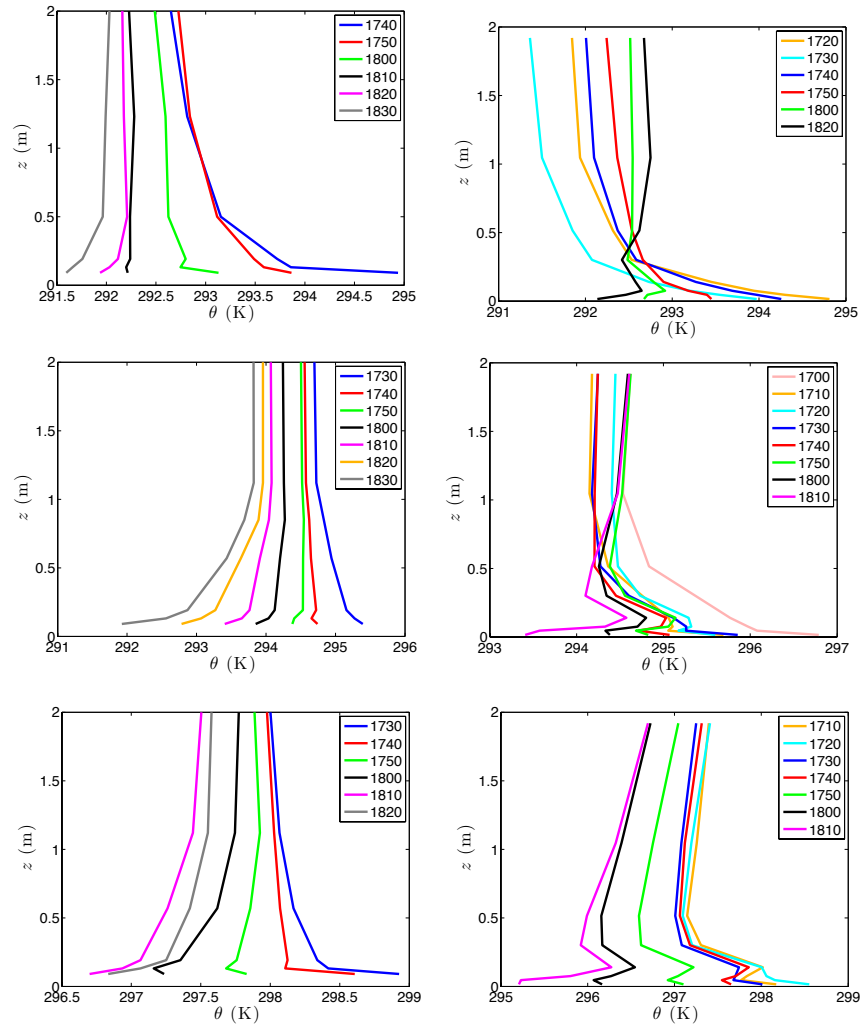
Figure 5.3: Same as Fig. 5.2 on 30 June 2011 (top), 1 July 2011 (middle) and 2 July 2011 (bottom).
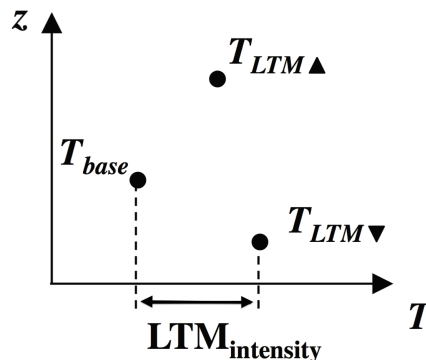
Figure 5.4: Illustration of the methodology used to identify LTM and quantify intensity..

an intensity of 0.5 K. This height is still in the range of LTM-heights reported by Raschke (1957). That day, FWs were not installed at T1 before 19:30 UTC. Therefore, we cannot contrast the presence of this higher LTM by measurements from T1.

A completely different situation was observed on 27 June 2011, with no clear LTM development. The T1-measurements showed a possible beginning of LTM, which did not progress.

On 30 June 2011, T1 showed a low-intensity (0.5 K) LTM at around 18:00 UTC, lasting less than 20 min. It was also observed at T2 with an intensity of 0.3 K. On 1 July 2011 a clearly marked (0.7 K) LTM was observed at T2 during one hour. On the other hand, T1 showed a less pronounced LTM (0.35 K), which persisted only 20 min. Moreover, there is a smaller local minimum at 0.5 m created by the evolution of the vertical profile of potential temperature forced by the presence of LTM. Finally, on 2 July 2011, T2 showed an LTM intensity of around 0.5 K during more than one hour. However, T1 showed a lower intensity (0.35 K) with a duration of 40 min.

IOP	LTM	LTM height T1 (m)	LTM height T2 (m)	LTM intensity T1 (K)	LTM intensity T2 (K)	LTM duration T1 (min)	LTM duration T2 (min)
24 June 2011	YES	0.131	0.07-0.14	0.35	0.7	20	40
25 June 2011	YES	0.131	0.3	-	0.5	-	40
27 June 2011	NO	-	-	-	-	-	-
30 June 2011	YES	0.131	0.07-0.14	0.5	0.3	20	40
1 July 2011	YES	0.131	0.07-0.14	0.35	0.7	20	60
2 July 2011	YES	0.131	0.07-0.14	0.3	0.5	40	70

Table 5.1: Characteristics of the observed LTM at T1 and T2 for all the studied IOPs.

5.4 Variables influencing LTM development

5.4.1 Wind characteristics

The analysis of wind conditions is crucial for studying the influence of mechanical turbulence in the appearance of LTM. Taking into account that all the studied days presented weak synoptic forcing, surface winds were driven mainly by mountain valley-flows (See Chapter 2, Nadeau et al., 2013).

Figure 5.5 shows the temporal evolution of the 2-m wind speed and direction observed at T1 and T2 avaraged over 5 minutes. The observed wind direction at T1 and T2 (Figs. 5.5a and b) clearly shows the typical mountain-valley circulation. Figures 5.5c, d show the temporal evolution of wind speed recorded at the two masts. The wind speed is lower at T2. This can be caused by the presence of several trees west of T2, or by the different surface cover. Before 17:30 UTC, winds of around 2.5 and 2 m s^{-1} were observed at T1 and T2, respectively. At 17:30 UTC, the wind speed started to decrease, except on 27 June 2011, indicating the beginning of the evening calm period. However, the decrease rate was not the same for all the IOPs, being faster on 24 June, 1 and 2 July 2011. Wind speed kept on decreasing until 18:30-19:00 UTC, when the wind speed was around 0.5 m s^{-1} at both masts. During this period, wind direction turned progressively from north to south (see Figs. 5.5a, b). After 19:00 UTC, surface downslope flow dominated and the wind speed increased (see Figs. 5.5c and d).

In stable conditions, Oke (1970) postulated that wind speed at 0.25 m has to be lower than 0.4 m s^{-1} in order for LTM to occur over short grass. Wind speed is measured at 2 m. Therefore, we need to extrapolate this value to 0.25 m to be able to compare it with previous results. For this purpose, we use the log-law approximation, which reads:

$$\text{WS} \approx \text{W}S_{ref} \frac{ln\,(z/z_0)}{ln\,(z_{ref}/z_0)} \; , \tag{5.3}$$

where WS is the velocity at height z, WS_{ref} is the velocity at height $z_{ref} = 2$ m, and z_0 is the roughness length (0.03 m in our case (Stull, 1988)). The results from this approximation show that, for all the analyzed days except 27 June 2011, the wind speed at 0.25 m was below 0.4 m s^{-1} (not shown).

5.4.2 Turbulence

The gradient Richardson number (Ri_g) is a crucial parameter for the study of LTM during stable night conditions. Oke (1970) postulated that a minimum Ri_g is needed to observe an LTM over different terrains in stable conditions. The gradient Richardson number is defined as (Stull, 1988):

$$Ri_g = \frac{g}{\overline{\theta_v}} \frac{\partial \overline{\theta_v}/\partial z}{\left(\partial \overline{u}/\partial z\right)^2 + \left(\partial \overline{v}/\partial z\right)^2} \; . \tag{5.4}$$
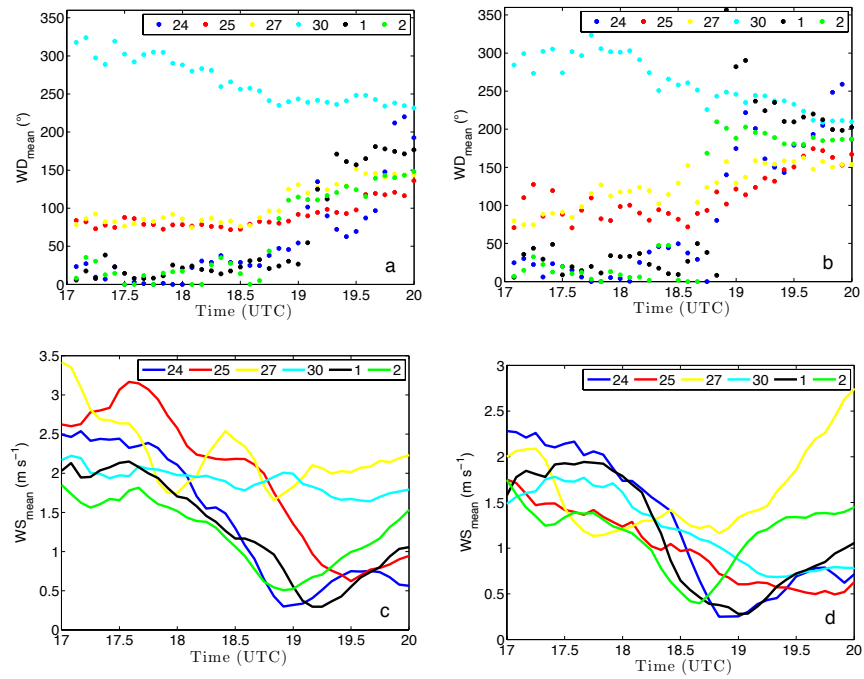
Figure 5.5: Temporal evolution, from 17:30 to 20:00 UTC, on all the studied days of the observed 2-m wind direction (top) and speed (bottom) at T1 (left) at 2.3 m and T2 (right) at 1.95 m averaged every 5 min.
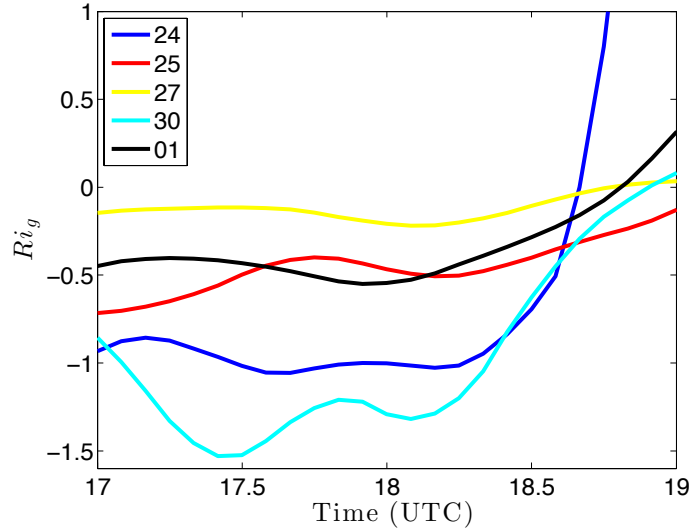
Figure 5.6: Temporal evolution of the observed gradient Richardson number at T1 from 17:30 UTC to 19:00 UTC on 24, 25 27 and 30 June 2011 and 1 July 2011.

We calculate the vertical gradients by using the lowest T1-sensors where the SAs were installed (at 2.23 and 3.23 m). Figure 5.6 shows the temporal evolution of the gradient Richardson number during the evening transition on all the studied days except 2 July 2011, which has some measurement error at 3.23m. Ri_g increased significantly for all the studied days during the evening, except for 27 June 2011, when Ri_g remains nearly constant and near zero. During this day, LTM was not observed (see Fig. 5.2), and large mechanical turbulence existed in the lower part of the boundary layer with weak convection.

An opposite situation occurred on 24 June 2011. On this day large negative Ri_g values were observed and weak turbulence and strong convection were also detected (see $-z/L$ in Table 4.1). 1 July 2011 had similar conditions to 24 June 2011 but being less convective day (see $-z/L$ in Table 4.1). On these two days LTM was clearly observed (see Figs. 5.2 and 5.3).

However, there are some days presenting large Ri_g and very large buoyancy and moderate horizontal turbulence that inhibits the occurrence of the LTM. This situation occurred for instance on 30 June 2011. This evening was characterized by moderate horizontal turbulence, but also still moderate convection (see $-z/L$ in Table 4.1). During the evening, Ri_g reached large values due to the relatively large buoyancy flux, which was more notable than the existing shear. This moderate wind shear caused a low LTM-intensity (see Fig. 5.3).

Oke (1970) defined in stable conditions $Ri_g = 0.1$ as the maximum value for observing LTM. During nighttime, when the main destabilizing force is mechanical turbulence, Ri_g can be used to define the best conditions for observing
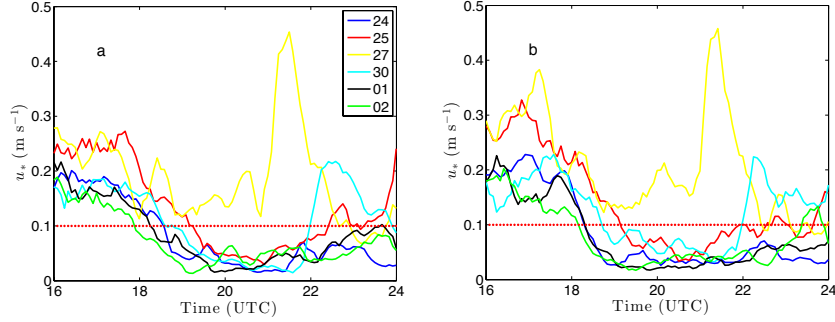
Figure 5.7: Temporal evolution of u_* from 16:00 UTC to 24:00 UTC on all the studied days at (a) T1 and (b) T2.

LTM. However, this Ri_g threshold cannot be compared with our results, because we observe LTM in unstable conditions. During the evening transition, Ri_g is not a reliable variable to describe the best conditions for observing LTM. During this period, buoyancy may still be an important force, and consequently large negative values of Ri_g can occur with significant horizontal turbulence.

Another variable which can show the decrease of turbulence during the afternoon transition is friction velocity (u_*). Figure 5.7 hows the temporal evolution of u_* during the evening transition for all the studied days with a 5 minute average. Due to the orography, during the afternoon, u_* decreased from around 0.25 m s^{-1} to values below 0.1 m s^{-1} (around 18:30 UTC at T1 and 18:00 UTC at T2). Afterwards it slightly increased but remaining at lower values. Vasudeva Murthy et al. (2005) define that with high turbulent transport (friction velocity approximately 0.1 m/s) the lifted minimum can occur but the layer slowly fades away. In our study case, for most of the IOPs the friction velocity was reduced to values lower than 0.1 m s^{-1} except on 27 June 2011, when friction velocity presented values higher than 0.1 m s^{-1} during the evening transition at both masts. Therefore, turbulence prevented the appearance LTM. Moreover, on 30 June 2011 u_* had low values but only during a short period and the LTM occurred also during a short period of time (see Figs. 5.7a, b).

Mukund et al. (2010) used wind speed fluctuations to analyze turbulence and its influence on LTM occurrence. Figure 5.8 shows the horizontal wind speed measured at 20 Hz and its running average every 500 s for all IOPs near T2. The LTM occurrence on 24 June 2011 (see Table 1) is associated with a clear decrease, not only of averaged wind speed but also of the turbulence (see Fig. 5.8a). A less pronounced decrease in both variables was observed (Figs. 5.8e and f) on 1 July and 2 July 2011. In contrast, on 27 June, when LTM was not observed, Fig. 5.8c shows that neither the averaged wind speed nor the turbulence decreased during the evening transition. Finally, Figs. 5.8b and d (25 and 30 June 2011) show a clear decrease in the averaged wind speed but the decrease in turbulence is lower. By comparing these facts with the parameters

described in Table 5.1, we can directly relate turbulence and averaged wind velocity with the intensity of the LTM. IOPs with a clear decrease on turbulence during evening transition, such as 24 June, 1 July or 2 July 2011, present larger LTM-intensity. Those days with a lower or non-existing decrease in wind speed fluctuations either have a less pronounced LTM or LTM is not present.

5.4.3 Radiation

Narasimha (1991); Vasudeva Murthy et al. (2005); Mukund et al. (2010, 2013) pointed out the radiative origin of LTM. For this reason, we also analyze the radiation measurements taken by the radiometers located near T2. Unfortunately, during all the days of the campaign a shadow produced by the 60-m tower located 160 m to the north-west of T2 affected the shortwave and net radiation measurements. Consequently, here we can only analyze the upwelling longwave radiation recorded by the Kipp&Zonen CNR1 net radiometer located at 0.8 m. However, we also estimate longwave radiation at LTM height by using the conservation of heat that reads (Stull, 1988):

$$\frac{\partial \overline{\theta}}{\partial t} + \overline{U_j}\frac{\partial \overline{\theta}}{\partial x_j} = \nu_\theta \frac{\partial^2 \overline{\theta}}{\partial x_j^2} - \frac{1}{\overline{\rho}C_p}\frac{\partial Q^*}{\partial x_j} - \frac{L_v E}{\overline{\rho}C_p} - \frac{\partial(\overline{u_j'\theta'})}{\partial x_j},\tag{5.5}$$

where x_j represents (x,y,z) for j=(1,2,3), ν_θ is the kinematic molecular diffusivity for heat in air, Q^* is the net radiation, L_v is the latent heat of vaporization of water, E is the phase change rate, ρ is density of the air, C_p is the specific heat at constant pressure for moist, air and u_j is the wind components (u,v,w) for j=(1,2,3).

The first term represents the tendency of the temperature, the second term describes the advection of heat by the mean wind. The third term is the mean molecular conduction of heat, the next term represents the net radiation flux divergence, and the fifth term describes the latent heat release, which is expected to be small in comparison with the other terms. The last term is the divergence of the turbulent heat flux.

If we consider very light winds, horizontal homogeneity and subsidence is neglected, the heat equation can be written as:

$$\frac{\partial \overline{\theta}}{\partial t} = \nu_\theta \frac{\partial^2 \overline{\theta}}{\partial z^2} - \frac{1}{\overline{\rho}C_p}\frac{\partial Q^*}{\partial z} - \frac{\partial(\overline{w'\theta'})}{\partial z}.\tag{5.6}$$

We integrate this equation from the ground to LTM height. If Eq. 5.6 is averaged every 5 min, $\frac{\partial \overline{\theta}}{\partial t} \approx 0$. Finally, by assuming constant ρC_p is constant, we obtain an approximation for the radiation at LTM height, which reads as:

$$\frac{Q^*}{\overline{\rho}C_p}\bigg|_{z=LTM} = -\nu_\theta \frac{\partial \overline{\theta}}{\partial z}\bigg|_{z=0m} + \frac{Q^*}{\overline{\rho}C_p}\bigg|_{z=0m} - \overline{w'\theta'}\big|_{z=2m}.\tag{5.7}$$

The second term of this equation is computed by using the temperature measured by the IR120 infrared camera and the lowest thermocouple located at
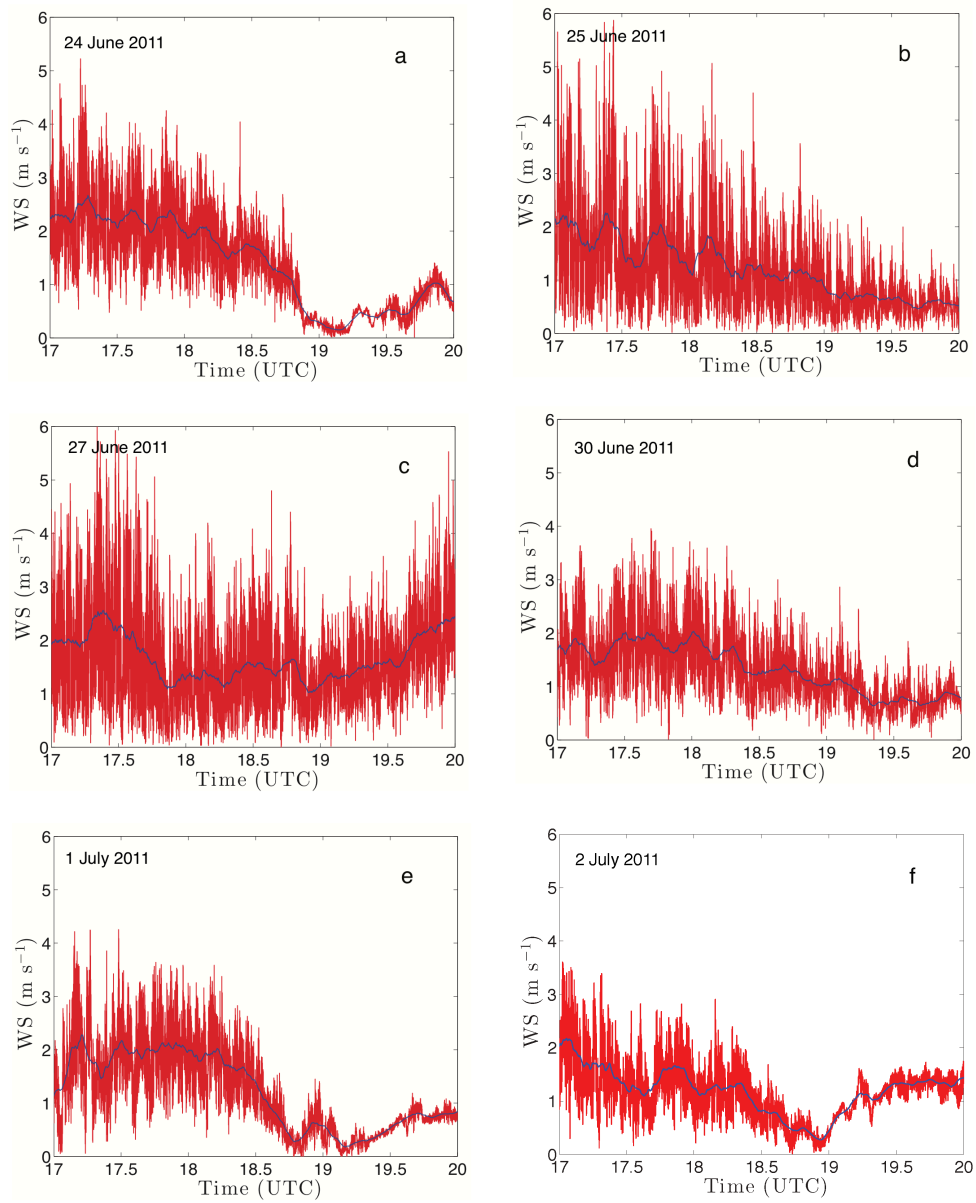
Figure 5.8: Temporal evolution of 2-m wind speed (red) and the wind speed moving average every 500 s (blue) on (a) 24 , (b) 25, (c) 27 and (d) 30 June and (e) 1 and (f) 2 July 2011 near T2.
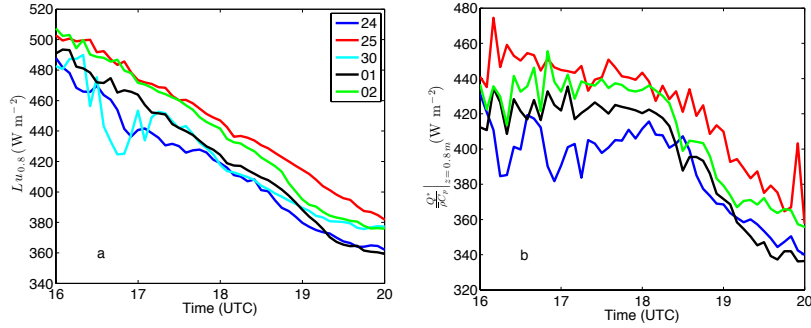
Figure 5.9: Temporal evolution of (a) upwards longwave radiation at 0.8 m on 24, 25 and 30 June 2011 and 1 and 2 July 2011 and (b) radiation estimated at LTM height on 24 and 25 June 2011 and 1 and 2 July 2011

0.015 and we approximate ν_θ to the ground molecular diffusion value. Moreover, to estimate the heat flux we use the measurement at lowest SA, located at 2 m, even though, it is outside the integration domain. During afternoon transition, most of $\left.\frac{Q^*}{\overline{\rho}C_p}\right|_{z=0m}$ and $\left.\frac{Q^*}{\overline{\rho}C_p}\right|_{z=LTM}$ corresponds to longwave radiation. Therefore, considering that the main contributor of the upwelling longwave radiation is the ground, we compute the longwave radiation emitted at the ground using the ground temperature (T_g) measured by the IR120 infrared camera as:

$$\left.\frac{Q^*}{\overline{\rho}C_p}\right|_{z=0m} \simeq \left. Lu\right|_{z=0} = \varepsilon\sigma_b T_g^4, \tag{5.8}$$

where ε is the emissivity of the ground (0.986) and σ_b is the Stefan–Boltzmann constant.

Figure 5.9a shows the temporal evolution of the upwelling longwave radiation measured by the Kipp&Zonen CNR1 net radiometer at 0.8 m. During afternoon transition, we observe a nearly constant decay rate for the upwelling longwave radiation at 0.8 m. Longwave radiation at the ground calculated by using Eq. 5.8 presents a similar evolution (not shown). However, we cannot correlate these two upwelling longwave radiations to analyze if there is any difference to explain the appearance of the LTM because the IR120 infrared camera and the radiation sensor have different response times (<1 s for the IR120 infrared camera and 18s for the Kipp&Zonen CNR1 net radiometer). Moreover, both sensors were not sampling using the same data logger. Consequently, we focus on analyzing the differences in the decay rate of upwelling longwave radiation at 0.8 m and the longwave radiation at LTM height calculated by using Eq. 5.7.

Figure 5.9b shows the temporal evolution of the longwave radiation at the LTM height estimated by using Eq. 5.7. In contrast to Fig. 5.9a, the longwave radiation decay rate is not constant and it changes around 17:30–18:30 UTC, when the LTM appears for some IOPs. The increase in the longwave radiation decay rate can be due to variation in the radiative cooling, which can accelerate

the descend of the temperature showing a minimum at LTM height.

Mukund et al. (2010) reported that LTM-intensity decreases when clouds were present, also suggesting the importance of radiation in the phenomenon. By analyzing the ceilometer measurements obtained during BLLAST (see Fig. 5.10), a completely clear sky is reported for all IOPs evening transition except on 30 June 2011. From the previous section, we know that during this day even though the conditions of turbulence were acceptable to observe LTM, its intensity was very low and its duration was short. These LTM-characteristics can be caused by the presence of clouds apart from wind conditions.

5.5   Conclusions

The presence of a Lifted Temperature Minimum during the evening transition is studied by means of observations taken during the BLLAST campaign. The campaign site presented ground characteristics suitable for observing LTM with moderate ground emissivity and thermal inertia. During this period of the day, LTM was observed at different heights, and with different intensity and duration for all IOPs except on 27 June 2011.

By studying the wind conditions characterized by a mountain-valley flow, we conclude that the days with a more marked decrease in mean wind speed and wind speed fluctuations (24 June or 1 July 2011) have a more intense LTM. On the other hand, on the days without a reduction in wind speed, such as 27 June 2011, LTM cannot be observed.

The gradient Richardson number has been previously used as a parameter to describe the best conditions for observing LTM in the stable boundary layer, when buoyancy forces are very small and they stabilize the atmosphere (Oke, 1970). However, during the evening transition, convective movements may still be important. Consequently, during this period of the day, Ri_g is not a suitable parameter to be used to identify the best conditions for the occurrence of LTM, because the very low mechanical turbulence needed for LTM can occur in relation to high and low Ri_g (see for instance LTM characteristics on 30 June 2011).

Finally, the longwave–radiative conditions are analyzed. We study the differences in the decay rate of the upwelling longwave radiation at 0.8 m and the longwave radiation at LTM height. Longwave radiation at LTM height decay in two different rates in contrast to the upwelling longwave radiation decay at 0.8 m which is constant in time. This change in the radiative conditions can modify the radiative cooling creating the LTM.

To conclude, it is possible to observe a Lifted Temperature Minimum during evening transition over a terrain with moderate emissivity and thermal inertia. In this case study, really calm conditions were observed during evening transition, due to the presence of the Pyrenees Mountains, which produce an early evening calm period that is easily defined by a change in wind velocity and turbulence. Moreover, a change in the radiative conditions was observed during the LTM period, which confirms its radiative origin.
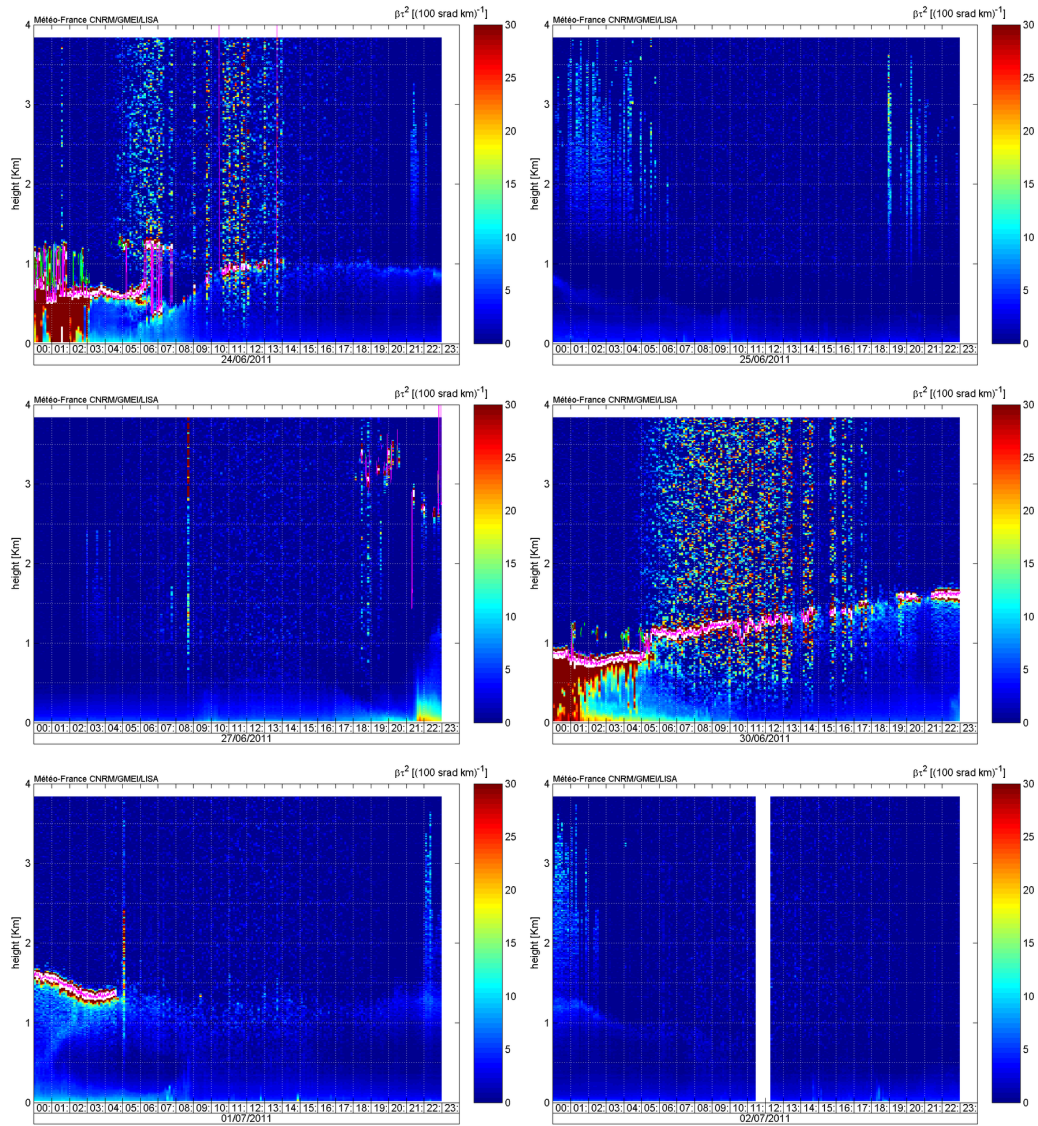
Figure 5.10: CT25K backscatter from a ceilometer located at Supersite 1 (see Chapter 2) on 24, 25, 27 and 30 June and 1 and 2 July 2011

Chapter 6

Summary and outlook

In this chapter, we present a summary of the most relevant results obtained in this thesis. Moreover, we include a section describing current and future research mainly regarding the afternoon transition period.

6.1   Summary

The transitional periods of the atmospheric boundary layer present some unknowns due to its complexity and rapid variability. The main objective of this thesis is to recognize and study some of these unresolved issues that affect the diurnal evolution of the atmospheric boundary layer. The research strategy followed to develop this thesis includes the use of measurements obtained in the BLLAST field campaign and two different numerical models to develop the analysis of Chatper 3: MLM and DALES. The main conclusions and contributions obtained from this research are described in the following paragraphs.

In Chapter 2, we describe the main characteristics of the BLLAST field campaign that are devoted to studying some of the unknowns related to the afternoon transition of the ABL. The observations from the BLLAST field campaign are the main tool used to develop this thesis. They have been and will be used to develop and combine several observational and numerical studies of the ABL during this period (Reuder et al., 2012; Garai et al., 2013; Graf et al., 2013; Blay-Carreras et al., 2014b; Angevine et al., 2014; Blay-Carreras et al., 2014a; Pietersen et al., 2014).

In Chapter 3, concerning the morning transitional periods, we show the importance of a precise definition of the characteristics of the residual layer and subsidence the development and evolution of a convective boundary layer. We simulate with DALES and MLM the same IOP, with and without considering the residual layer in the initial profile (only with DALES) and subsidence. Analyzing the DALES results, we observe a completely different behavior in potential temperature, boundary-layer depth and the turbulent kinetic energy evolution during the first part of the day. Numerical experiments consider-

116

ing the residual layer fit correctly with the observed potential temperature and the boundary-layer depth, due to a better approximation of the entrainment heat flux. In the numerical experiments without the residual layer, the growth rate of the boundary-layer depth is lower until approximately midday, and the boundary-layer depth is underestimated by several hundred meters. Additionally, we analyze the influence of the residual layer in the evolution of the TKE budget. Comparing RL and nRL numerical experiments, we show that larger buoyancy, transport-pressure and dissipation terms exist before including the residual layer in the mixed layer (in the numerical experiments with the residual layer). After merging the residual layer and the mixed layer, buoyancy and shear terms increase at the inversion and near the surface. We observe differences in the shear term between the numerical experiments with and without RL in the initial vertical profiles. They are mainly due to a different prescription of the initial wind profile. By using surface and tower observations, we also analyze the influence of the residual layer in the evolution of the CO_2 mixing ratio. Before merging the residual layer and the mixed layer, the CO_2 mixing ratio is mainly driven by the CO_2 entrainment flux. However, as the day progresses, the CO_2 entrainment flux becomes very small, as the boundary layer depth is almost constant during the rest of the day; and the CO_2 mixing ratio is very similar over the different land uses, because the storage term is below 0.5 ppm h^{-1} over all the surfaces due to the large value of z_1. Finally, we study the role of subsidence, which is important when z_1 is large. We determine the effect of subsidence in the evolution of the TKE terms, mainly restricted to the upper part of the mixed layer and to the entrainment zone. Subsidence decreases the turbulence production by buoyancy in the upper mixed layer, but it increases the contribution of the pressure-transport term.

In Chapter 4, we analyze the failure of the flux gradient theory during the evening transition (see Section 1.3.3). In all the days analyzed, we observe a delay of $\sim$ 30-80 min between the time when the buoyancy flux ceases and when the sign changes for the vertical gradient of the virtual potential temperature. We observe that, in near stable conditions, gradient–theory fails to locally analyze the relation between the dimensionless temperature gradient and the Monin-Obukhov parameter ($-z/L$). We also observe in some of the IOPs that the duration of the delay time is similar to the time scale associated with the last eddy movement (convective time). Analyzing the evolution of $-z/L$, we observe that IOPs with strong convective conditions, convective time and delay time are similar. However, the differences are larger if midday convection is weaker, because the delay time is larger due to the increase in horizontal turbulence. Moreover, we define a transitional turbulent Rayleigh number, which helps us to describe the decay of the convection. Lower values of the transitional turbulent Rayleigh number are related with higher turbulent viscosity and thermal diffusivity, which help to slow down the last eddy movement and to increase the delay time.

In Chapter 5, we study the existence of a lifted temperature minimum (LTM) during the evening transition (see Section 1.3.3). LTM existence was previously observed during the night, when the stable boundary layer is completely de-

veloped. Due to the orography of the area where the BLLAST campaign took place, the dynamics of the atmosphere in IOPs was usually driven by mountain-valley flows, presenting a calm period during the evening transition. During the early evening calm period, LTM is detected in all the IOPs of the BLLAST campaign except for 27 June 2011. On this day, wind speed during the early evening calm period was not sufficiently reduced. Moreover, IOPs with a larger decrease rate of mean wind speed and turbulence present a more intense LTM. Unlike previous studies, the Richardson number (Ri) could not be used as a parameter to describe the best conditions for observing LTM during the evening period because, at this moment, positive and negative values of Ri may exist. For this reason, we use the correlation between the upward longwave radiation measured at 0.8 m and the calculated longwave radiation at the ground in order to justify the appearance of LTM. We observe a high correlation between them during the afternoon transition, but the correlation decreases when LTM appears. Therefore, LTM is related with a change in the radiative conditions close to the ground, showing the importance of the competing forces during the afternoon transition.

In this thesis, we increase the knowledge of three specific issues of atmospheric transitional periods which had remained poorly explored. Eventhough, there is lot of unknowns unexplored which have to be solved and the measurements of BLLAST field campaign are and will be a crucial to clarify some of them.

6.2 Outlook

The results obtained in this thesis clarify some of the unknowns relevant to the transitional periods. However, there are still many areas not covered that would help to understand the transitional periods of the atmospheric boundary layer (see Section 1.3.3).

Some of the areas which are interesting to be analyzed are the ones suggested by the BLLAST project (Lothon et al., 2014). Here we summarize some of the ongoing studies related to this subject, and we also point out additional studies that would be interesting for increasing knowledge about the ABL transitions.

- *TKE decay.* ABL turbulence decay in relation with buoyancy conditions over different surfaces is currently analyzed by a group of researchers from Laboratoire d'Aérologie (France) using observations and LES numerical experiments (Darbieu et al., 2012b). They observe that TKE decays at three different rates, but it follows the same pattern in all different terrains. It shows that the TKE decay near the surface is strongly governed by buoyancy effects during BLLAST IOP days.

- *Competing forces during the afternoon transition.* There are several competing forces during the afternoon transition, such as radiation, advection, divergence, entrainment and wind shear. In this thesis, some of them are analyzed (see Section 1.3.3).

One of the processes to be analyzed is entrainment during the afternoon transition (Pino et al., 2006b; Canut et al., 2012). Additional comparisons of numerical experiments with observations are needed to understand the influence of the entrainment fluxes on the evolution of the ABL during the afternoon transition. A group of researchers from Wageningen University is studying the entrainment influences on surface layer measurements (Van de Boer et al., 2014). They show that surface layer observations can be used to identify days with a predominance of entrainment. From an analysis of the Monin–Obukhov similarity relationships for the variance of humidity, they observe that on some days the variance of humidity deviates from the documented values, due to high entrainment ratios.

A general study of another competing force, the divergence of the radiative processes, that focuses not just on the presence of lifted minimum temperature, will make a significant contribution as afternoon transition has high radiative cooling (Sun et al., 2003). Another group from Wageningen University is performing an analysis of radiative divergence (G. J. Steeneveld, personal communication). An analysis of the surface energy budget is being performed by researchers at the University of Bergen (Norway) in collaboration with the Physikalisch-Meteorologisches Observatorium Davos and World Radiation Center (Switzerland) (J. Reuder, personal communication).

- *The evolution of length scales.* Regarding the evolution of the length scales during the afternoon transition, several studies found different results (Sorbjan, 1997; Pino et al., 2006b; Nadeau et al., 2011). A study of how to represent the transition using non-dimensional analysis or new scalings is needed to define, for instance, whether the scales in the mixed and then residual layer increase or decrease during the afternoon transition. A group of scientists from Laboratoire d'Aérologie (France) is analyzing the vertical and temporal evolution of turbulence spectra in the late afternoon transition in order to study the evolution of the scaling of the vertical velocity (Darbieu et al., 2014). They observe that during the afternoon transition the surface layer with a decreasing lower scale decouples from the overlying layer with a larger scale.

- *Importance of surface heterogeneity.* The influence of surface heterogeneity on the dynamics of the decaying mixed layer is not covered in this thesis. It is relevant during daytime and nighttime conditions, but it has been only partially studied during transitional periods (Nadeau et al., 2011; Ouwersloot et al., 2011). A group of researchers from Universitat de les Illes Balears (Spain) in collaboration with researchers form Hochschule Ostwestfalen-Lippe (Germany), University of Bergen (Norway) and Universität Tübingen (Germany) are analyzing the effect of the sub-kilometric scale terrain heterogeneities in the surface energy budget through observations and numerical modeling (Cuxart et al., 2014). They observe that the advection term depends on the scale over which it is computed. Moreover,

they notice that large surface heterogeneities in their specific situation come partly from the variability at small scales of the soil water contents, which reflects on the surface temperature.

Moreover, as Mukund et al. (2013) did during nighttime, a study of LTM over different artificial and natural surfaces can provide truly relevant inputs to LTM analysis during the evening transition, as the surface characteristics (emissivity and thermal conductivity) cause differences in LTM structure.

- *Cloud cover and low level nocturnal jet.* It would also be interesting to study the importance of clouds during the afternoon transition and the relevance of the afternoon transition characteristics in the appearance of the nocturnal jet. In Chapter 5, we show the importance of cloud coverage when observing a more marked LTM, as cloud coverage directly affects radiation, which is one of the competing forces during the afternoon transition. There are no deep studies of how cloud coverage can affect the competing forces involved in the afternoon transition. Moreover, even though the nocturnal jet was studied (Stensrud, 1996; Banta et al., 2002), the role of the afternoon transition is not clear regarding the development of suitable conditions for the appearance of the nocturnal jet.

- *Evolution of compounds during the afternoon transition.* In this thesis the evolution of the CO_2 mixing ratio is studied during the morning transition, but the afternoon transition is not addressed. Therefore, study of the evolution of compounds during the afternoon transition can improve knowledge of how they are transported at a larger scale due to their incorporation in the residual layer. A group of researchers from Université du Littoral Côte D'Opale – Laboratoire de Physico-Chimie de l'Atmosphère (France) is studying submicronic aerosols during the BLLAST campaign (P. Flament, personal communication). Preliminary results show that sulfate formation is related to local nucleation/growing processes, but distant sources have also affected the aerosol chemistry in the boundary layer.

- *Parameterizations for numerical weather prediction models.* It would be interesting to propose new parameterizations to be included in the weather forecast models, as these types of models do not forecast well some phenomena appearing during the transition periods, such as fog onset/dissipation or the onset of the low level jet. A group of researchers from Météo-France (France), in collaboration with Laboratoire d'Aérologie (France), are analyzing the representation of the afternoon transition in numerical weather prediction models (Couvreux et al., 2014). They use two models (AROME and ARPEGE), and they observe a cold bias in both of them. Moreover, they found that the high-resolution model, AROME, resolves the vertical structures better, and it is also capable of capturing both subsidence and the maximum water vapor mixing ratio in the upper part of the RL.

Bibliography

Acevedo, O. and Fitzjarrald, D. R.: The early evening surface-layer transition: Temporal and spatial variability, J. Atmos. Sci., 58, 2650–2667, 2001.

Anfossi, D., Schayes, G., Degrazia, G., and Goulart, A.: Atmospheric turbulence decay during the solar total eclipse of 11 August 1999, Bound.-Lay. Meteorol., 111, 301–301, 2004.

Angevine, W. M.: Transitional, entraining, cloudy, and coastal boundary layers, Acta Geophys., 56, 2–20, 2008.

Angevine, W. M., White, A. B., and Avery, S. K.: Boundary-layer depth and entrainment zone characterization with a boundary-layer profiler, Bound.-Lay. Meteorol., 68, 375–385, 1994.

Angevine, W. M., Baltink, H. K., and Bosveld, F. C.: Observations of the morning transition of the convective boundary layer, Bound.-Lay. Meteorol., 101, 209–227, 2001.

Angevine, W. M., Bazile, E., Legain, D., and Pino, D.: Land surface spinup for episodic modeling, Atmos. Chem. Phys. Discuss., 14, 4723–4744, 2014.

Baldocchi, D. and Meyers, T.: On using eco-physiological, micrometeorological and biogeochemical theory to evaluate carbon 780 dioxide, water vapor and trace gas fluxes over vegetation, Agr. Forest Meteorol., 90, 1–25, 1998.

Balin, I., Parlange, M., Calpini, B., Simeonov, V., and van den Bergh, H.: Elevated Atmospheric Boundary Layer Over the Swiss Alps during the August 2003 Heat Wave, 22nd Internation Laser Radar Conference (ILRC 2004), Proceedings of the Conference held 12-16 July, 2004 in Matera, Italy. Edit, 561, 2004.

Balsley, B. B., Svensson, G., and Tjernström, M.: On the scale-dependence of the gradient Richardson number in the residual layer, Bound.-Lay. Meteorol., 127, 57–72, 2008.

Bange, J., Spieβ, T., and van den Kroonenberg, A.: Characteristics of the early-morning shallow convective boundary layer from Helipod Flights during STINHO-2, Theor. Appl. Climatol., 90, 113–126, 2007.

Banta, R., Newsom, R. K., Lundquist, J. K., Pichugina, Y. L., Coulter, R. L., and Mahrt, L.: Nocturnal Low-Level Jet Characteristics Over Kansas During Cases-99, Bound.-Lay. Meteorol., 105, 221–252, 2002.

Batchelor, G. K.: An Introduction to Fluid Mechanics, Cambridge University Press, London, 1967.

Batchelor, G. K.: The Theory of Homogeneous Turbulence, Cambridge University Press, London, 1982.

Beare, R. J.: The Role of Shear in the Morning Transition Boundary Layer, Bound.-Lay. Meteorol., 129, 395–410, 2008.

Beare, R. J., Edwards, J. M., and Lapworth, A. J.: Simulation of the observed evening transition and nocturnal boundary layers: large-eddy modelling, Q. J. Roy. Meteor. Soc., 132, 81–99, 2006a.

Beare, R. J., Macvean, M., Holtslag, A. A. M., Cuxart, J., Esau, I., Golaz, J. C., Jímenez, M. A., Khairoutdinov, M. F., Kosovic, B., Lewellen, D. C., Lund, T. S., Lundquist, J. K. McCabe, A., Moene, A., Noh, Y., Raasch, S., and Sullivan, P. P.: An intercomparison of large-eddy simulations of the stable boundary-layer, Bound.-Lay. Meteorol., 118, 247–272, 2006b.

Bhat, G. S.: Near-surface temperature inversion over the Arabian Sea due to natural aerosols, Geophys. Res. Lett., 33, L02 802, 2006.

Biferale, L., Boffeta, G., Celani, A., Lanotte, A., Toschi, F., and Vergassola, M.: The decay of homogeneous anisotropic turbulence, Phys. Fluid., 8, 2105–2112, 2003.

Blay-Carreras, E., Pardyjak, E., Pino, D., Lohou, F., and Lothon, M.: Counter-gradient heat flux observations during the evening transition period, Atmos. Chem. Phys. Discuss., 14, 7711–7737, 2014a.

Blay-Carreras, E., Pino, D., Van de Boer, A., De Coster, O., Darbieu, C., Hartogensis, O., Lohou, F., Lothon, M., Pietersen, H., and Vilà-Guerau de Arellano, J.: Role of the residual layer and large-scale subsidence on the development and evolution of the convective boundary layer, Atmos. Chem. Phys., 14, 4515–4530, 2014b.

Boeing: Statistical Summary of Commercial Jet Airplane Accidents Worldwide Operations 1959 - 2008, Tech. rep., Aviation Safety, Boeing Commercial Airplanes, United States of America, 2009.

Boer, A. v. d., Moene, A., Graf, A., Schüttemeyer, D., and Hartogensis, O.: Quantification of the effect of surface heterogeneity on scalar variance similarity, in: 20th Symposium on Boundary Layers and Turbulence/18th Conference on Air-Sea Interaction, American Meteorological Society, Boston (USA), 2012.

Businger, J. A., Wyngaard, J. C., Izumi, Y., and Bradley, E. F.: Flux-Profile Relationships in the Atmospheric Surface Layer, J. Atmos. Sci., 28, 181–189, 1971.

Campbell, G. S. and Norman, J.: An Introduction to Enviromental Biophysics, Springer, 2 ed., 1998.

Canut, G., Couvreux, F., Lothon, M., Pino, D., and Sad´id, F.: Observations and Large-Eddy Simulations of Entrainment in the Sheared Sahelian Boundary Layer, Bound.-Lay. Meteorol., 142, 79–101, 2012.

Carlson, M. A. and Stull, R.: Subsidence in the Nocturnal Boundary Layer, J. Clim. Appl. Meteorol., 25, 1088–1099, 1986.

Carson, D. J.: The development of a dry inversion-capped convectively unstable boundary layer, Q. J. R. Meteorol. Soc., 99, 450–467, 1973.

Casso-Torralba, P., Vilà-Guerau de Arellano, J., Bosveld, F. C., Soler, M. R., Vermeulen, A., Werner, C., and Moors, E.: J. Geophys. Res., p. D12119, doi:10.1029/2007JD009583.

Caughey, S. J. and Kaimal, J. C.: Vertical Heat Flux in the Convective Boundary Layer, Q. J. R. Meteorol. Soc., 103, 811–815, 1977.

Chapra, S. C. and Canale, R. P.: Numerical Methods for Engineers, Boston: McGraw-Hill Companies, 3 ed., 1998.

Cohn, S. A. and Angevine, W. M.: Boundary Layer Height and Entrainment Zone Thickness Measured by Lidars and Wind-Profiling Radars, J. Appl. Meteorol., 39, 1233–1247, 2000.

Cole, G. S. and Fernando, H. J. S.: Some aspects of the decay of convective turbulence, Fluid Dyn. Res., 23, 161–176, 1998.

Conzemius, R. J. and Fedorovich, E.: Dynamics of Sheared Convective Boundary Layer Entrainment. Part I: Methodological Background and Large-Eddy Simulations, J. Atmos. Sci., 63, 1151–1178, 2006.

Couvreux, F., Bazile, E., Seity, Y., Lothon, M., Guichard, F., Canut, G., Lohou, F., Pietersen, H., and Legain, D.: Representation of the afternoon transition in Numerical Weather Prediction models: evaluation with BLLAST data, in: EGU General Assembly 2014, American Meteorological Society, Vienna, Austria, 2014.

Cuijpers, J. W. M. and Duynkerke, P. G.: Large Eddy Simulation of Trade Wind Cumulus Clouds, J. Atmos. Sci., 50, 3894–3908, 1993.

Cuijpers, J. W. M. and Holtslag, A. A. M.: Impact of skewness and nonlocal effects on scalar and buoyancy fluxes in convective boundary layers, J. Atmos. Sci., 55, 151–162, 1998.

Culf, A. D., Fisch, G., Malhi, Y., and Nobre, C. A.: The influence of the atmospheric boundary layer on carbon dioxide concentrations over a tropical forest, Agr. Forest Meteorol., 85, 149–158, 1997.

Cuxart, J., Yague, C., Morales, G., Terradellas, E., Orbe, J., Calvo, J., Fernandez, A., Soler, M. R., Infante, C., Buenestado, P., Espinalt, A., Joergensen, H. E., Rees, J. M., Vilá, J., Redondo, J. M., Cantalapiedra, I. R., and Conangla, L.: Stable Atmospheric Boundary-Layer Experiment in Spain (SABLES 98): A Report, Bound.-Lay. Meteorol., 96, 337–370, 2000.

Cuxart, J., Wrenger, B., Jímenez, M., Dünnermann, J., Reuder, J., Jonassen, M., Martínez, D., Conangla, L., and Lothon, M.: Evaluation of the effect of the sub-kilometric scale terrain heterogeneities in the surface energy budget through observations and numerical modelling, in: EGU General Assembly 2014, American Meteorological Society, Vienna, Austria, 2014.

Darbieu, C., Lohou, F., Couvreux, F., Lothon, M., Durand, P., Guichard, F., and Patton, N.: Large eddy simulations of convective boundary layer during late afternoon transition, in: 20th Symposium on Boundary Layers and Turbulence/18th Conference on Air-Sea Interaction, American Meteorological Society, Boston (USA), 2012a.

Darbieu, C., Lohou, F., Lothon, M., Alexander, D., de Coster, O., Durand, P., Legain, D., Traulle, O., Pietersen, H., and Pique, E.: Turbulence kinetic energy decay in the late afternoon over heterogeneous surface: BLLAST experiment, in: 20th Symposium on Boundary Layers and Turbulence/18th Conference on Air-Sea Interaction, American Meteorological Society, Boston (USA), 2012b.

Darbieu, C., Lohou, F., Lothon, M., Pino, D., Durand, P., Blay-Carreras, E., and Vilà-Guerau de Arellano, J.: Evolution of the turbulence during the afternoon transition of the convective boundary layer: a spectral analysis, in: 21th Symposium on Boundary Layers and Turbulence, American Meteorological Society, Leeds, United Kingdom, 2014.

de Arellano, J. V.-G., Gioli, B., Miglietta, F., Jonker, H. J. J.and Baltink, H. K., Hutjes, R. W. A., and Holtslag, A. A. M.: The entrainment process of carbon dioxide in the atmospheric boundary layer, J. Geophys. Res., 109, D18 110, doi:10.1029/2004JD004725, 2004.

De Coster, O. M. Y. and Pietersen, H. P.: BLLAST uniform processing of Eddy–Covariance data, Tech. rep., Wageningen University and Research Center, The Netherlands, URL `http://bllast.sedoo.fr/documents/reports/H-Pietersen Ode-Coster BLLAST-surf flx-uniform-processing.pdf`, 2011.

Deardorff, J. W.: Theoretical expression for the countergradient vertical heat flux, J. Geophys. Res., 77, 5900–5904, 1972.

Deardorff, J. W., Willis, G. E., and Stockton, B. H.: Laboratory studies of the entrainment zone of a convectively mixed layer, J. Fluid Mech., 100, 41–64, 1980.

Derbyshire, S. H.: Stable boundary layer revisited, Q. J. Roy. Meteorol. Soc., 116, 127–158, 1990.

Doran, J. C., Berkowitz, C. M., Coulter, R. L., Shaw, W. J., and Spicer, C. W.: The 2001 Phoenix Sunrise experiment: vertical mixing and chemistry during the morning transition in Phoenix, Atmos. Environ., 37, 2365–2377, 2003.

Driedonks, A. G. M.: Models and observations of the growth of the atmospheric boundary layer, Bound.-Lay. Meteorol., 23, 283–306, 1982.

Edwards, J.: Radiative Processes in the Stable Boundary Layer: Part I. Radiative Aspects, Bound.-Lay. Meteorol., 131(2), 105–126, 2009.

Edwards, J. M., Beare, R. J., and Lapworth, A. J.: Simulation of the observed evening transition and nocturnal boundary layers: Single-column modelling, Q. J. R. Meteorol. Soc., 132, 61–80, 2006.

Emeis, S. and Schäfer, K.: Remote Sensing Methods to Investigate Boundary-layer Structures relevant to Air Pollution in Cities, Bound.-Lay. Meteorol., 121, 377–385, 2006.

Fedorovich, E.: Modeling the Atmospheric Convective Boundary Layer within a Zero-Order Jump Approach: An Extended Theoretical Framework, J. Appl. Meteorol., 34, 1916–1928, 1995.

Fedorovich, E., Kaiser, R., Rau, M., and Plate, E.: Wind Tunnel Study of Turbulent Flow Structure in the Convective Boundary Layer Capped by a Temperature Inversion, J. Atmos. Sci., 53, 1273–1289, 1996.

Fedorovich, E., Nieuwstadt, F. T. M., and Kaiser, R.: Numerical and laboratory study of horizontally evolving convective boundary layer. Part II: Effects of elevated wind shear and surface roughness, J. Atmos. Sci., 58(3), 546–560, 2001.

Ferziger, J. H. and Peric, M.: Computational Methods for Fluid Dynamics, Springer, 3 ed., 2002.

Fitzjarrald, D. R., Freedman., J. M., Czikowskyand, M. J., Sakai, R. K., Acevedo, O. C., and Moraes, O.: Momentum and scalar transport during the decay of CBL turbulence., in: Proc. of the 16th Symposium on Boundary Layers and Turbulence, Portland (ME), EUA, 2004.

Fochesatto, G. J., Drobinski, P., Flamant, C., Guedalia, D., Sarrat, C., Flamant, P. H., and Pelon, J.: Evidence of dynamical coupling between the residual layer and the developing convective boundary layer, vol. 99, pp. 451–464, 2001.

Franchitto, S. H. and Rao, V. B.: The correlation between temperature gradient and eddy heat flux in the northern and southern hemispheres, J. Meteorol. Soc. Japan. Ser. II, 81(1), 163–168, 2003.

Garai, A., Pardyjak, E. R., Steeneveld, G.-J., and Kleissl, J.: Surface Temperature and Surface-Layer Turbulence in a Convective Boundary Layer, Bound.-Lay. Meteorol., 148, 51–72, 2013.

Garratt, J. R.: The Atmospheric Boundary Layer, Cambridge University Press, London, 1994.

Gayevsky, U.: Surface temperature of large territories, Proc. Main Geophys. Obs., 26, 291–310, 1952.

Geiger, R.: The Climate Near the Ground, Harvard University Press, 1957.

George, W. K.: The decay of homogeneous isotropic turbulence, Phys. Fluid., 4, 1492–1509, 1992.

Ghan, S. J.: Modelling the synoptic scale relationship between eddy heat flux and the meridional temperature gradient, Massachusetts Institute of Technology, 1981.

Gibert, F., Arnault, N., Cuesta, J., Plougonven, R., and Flamant, P. H.: Internal gravity waves convectively forced in the atmospheric residual layer during the morning transition, Q. J. R. Meteorol. Soc., 137, 1610–1624, 2011.

Gioli, B., Miglietta, F., Vaccari, F. P., Zaldei, A., and De Martino, B.: The Sky Arrow ERA, an innovative airborne platform to monitor mass, momentum and energy exchange of ecosystems, Annals Geophysicae, 49, 109–116, 2009.

Goulart, A., Degrazia, G., Rizza, U., and Anfossi, D.: A theoretical model for the study of convective turbulence decay and comparison with Large-Eddy Simulation data, Bound.-Lay. Meteorol., 107, 143–155, 2003.

Goulart, A. G., Bodmann, B. E. J., de Vilhena, M. T. M. B., Soares, P. M. M., and Moreira, D. M.: On the Time Evolution of the Turbulent Kinetic Energy Spectrum for Decaying Turbulence in the Convective Boundary Layer, Bound.-Lay. Meteorol., 138, 61–75, 2011.

Graf, A., Werner, J., Langensiepen, M., van de Boer, A., Schmidt, M., Kupisch, M., and Vereecken, H.: Validation of a minimum microclimate disturbance chamber for net ecosystem flux measurements, Agric. For. Meteorol., 174–175, 1–14, 2013.

Graf, K., Schumann, U., Mannstein, H., and Mayer, B.: Aviation induced diurnal North Atlantic cirrus cover cycle, Geophys. Res. Lett., 39, L16 804, doi:10.1029/2012GL052590, 2012.

Grant, A. L. M.: An observational study of the evening transition boundary layer, Q. J. Roy. Meteor. Soc., 123, 657–677, 1997.

Grimsdell, A. W. and Angevine, W. M.: Observations of the afternoon transition of the convectiveboundary layer, Q. J. Roy. Meteor. Soc., 41, 3–11, 2002.

Haeffelin, M., Angelini, F., Morille, Y., Martucci, G., Frey, S., Gobbi, G., Lolli, S., Dowd, C. O. ., Sauvage, L., Xueref-Rémy, I., Wastine, B., and Feist, D.: Evaluation of mixing-height retrievals from automatic profiling lidars and ceilometers in view of future integrated networks in Europe, Bound.-Lay. Meteorol., 143(1), 49–75, 2012.

Han, B., Lü, S., and Ao, Y.: Development of the convective boundary layer capping with a thick neutral layer in Badanjilin: Observations and simulations, Adv. Atmos. Sci., 29, 177–192, 2011.

Heo, B. H., Jacoby-Koaly, S., Kim, K., Campistron, B., Benech, B., and Jung, E.: Use of the Doppler Spectral Width to Improve the Estimation of the Convective Boundary Layer Height from UHF Wind Profiler Observations, J. Atmos. Oceanic Technol., 20, 408–424, 2003.

Hess, G. D., Hicks, B. B., and Yamada, T.: The impact of the Wangara experiment, Bound.-Lay. Meteorol., 20, 135–174, 1981.

Heus, T., van Heerwaarden, C. C., Jonker, H. J. J., Siebesma, A. P., Axelsen, S., van den Dries, K., Geoffroy, O., Moene, A. F., Pino, D., de Roode, S. R., and Vilà-Guerau de Arellano, J.: Formulation of and numerical studies with the Dutch Atmospheric Large-Eddy Simulation (DALES), Geosci. Model Dev., 3, 415–444, 2010.

Holtslag, A. A. M. and Moeng, C.: Eddy diffusivity and countergradient transport in the convective atmospheric boundary layer, Bound.-Lay. Meteorol., 48(14), 1690–1698, 1991.

Jacobson, M. Z.: Fundamentals of Atmospheric Modeling, Cambridge University Press, London, 2005.

Jonker, H. J. J., Duynkerke, P. G., and Cuijpers, J. W. M.: Mesoscale fluctuations in scalars generated by boundary layer convection, J. Atmos. Sci., 56, 801–808, 1999.

Kaimal, J. C. and Wyngaard, J. C.: The Kansas and Minnesota experiments, Bound.-Lay. Meteorol., 50, 31–47, 1990.

Kaimal, J. C., Wyngaard, J. C., Haugen, D. A., Coté, O. R., Izumi, Y., Caughey, S. J., and Readings, C. J.: Turbulence Structure in the Convective Boundary Layer, J. Atmos. Sci., 33, 2152–2169, 1976.

Kundu, P. J. and Cohen, I. M.: Fluid Mechanics, Academic Press, Waltham (MA), USA, 904 pp., 2010.

Lake, J. V.: The temperature profile above bare soil on clear nights, Q. J. R. Meteorol. Soc., 82, 187–197, 1956.

Lapworth, A.: The Morning Transition of the Nocturnal Boundary Layer, Bound.-Lay. Meteorol., 119, 501–526, 2006.

Legain, D., Bousquet, O., Douffet, T., Tzanos, D., Moulin, E., Barrie, J., and Renard, J.-B.: High-frequency boundary layer profiling with reusable radiosondes, Atmos. Meas. Tech., 6, 2195–2205, 2013.

LeMone, M. A., Zhou, M., Moeng, C.-H., Lenschow, D. H., Miller, L. J., and Grossman, R. L.: An observational study of wind proÞles in the baroclinic convective mixed layer, Bound.-Lay. Meteorol., 90, 47–82, 1999.

LeMone, M. A., Grossman, R. L., Mcmillen, R. T., Liou, K.-N., Ou, S., Mckeen, S., Angevine, W., Ikeda, K., and Chen, F.: Cases-97: Late-Morning Warming And Moistening Of The Convective Boundary Layer Over The Walnut River Watershed, Bound.-Lay. Meteorol., 104, 1–52, 2002.

Lenschow, D. H.: Model of the height variation of the turbulence kinetic energy budget in the unstable planetary boundary layer, J. Atmos. Sci., 31, 465–474, 1974.

Lesieur, M., Metais, O., and Comte, P.: Large-Eddy Simulations of Turbulence, Cambridge University Press, 2005.

Lilly, D. K.: The representation of small-scale turbulence in numerical simulation experiments, National center for atmospheric research, 1966a.

Lilly, D. K.: The representation of small-scale turbulence in numerical simulation experiments, 281, 1966b.

Lilly, D. K.: Models of cloud-topped mixed layers under a strong inversion, Q. J. R. Meteorol. Soc., 94, 292–309, 1968.

Lothon, M. and Lenschow, D.: Studying the afternoon transition of the planetary boundary layer, Eos Trans. AGU, 91(29), 253–260, 2010.

Lothon, M., Couvreux, F., Durand, P., Hartogensis, O., Legain, D., Lohou, F., Pardyjak, E. R., Pino, D., Reuder, J., Vilà-Guerau de Arellano, J., Alexander, D., Augustin, P.and Bargain, E., Barrié, J., Bazile, E., Bezombes, Y., Blay-Carreras, E., van de Boer, A., Boichard, J. L., de Coster, O., Cuxart, J., Dabas, A., Darbieu, C., Deboudt, K., Delbarre, H., Derrien, S., Faloona, I., Flamant, P., Fourmentin, M., Garai, A., Gibert, F., Gioli, B., Graf, A., Groebner, J., Guichard, F., Jonassen, A., von Kroonenbeerg, M., Lenschow, D., Martin, S., Martinez, D., Mastrorillo, L., Moene, A., Molinos, F., Moulin, E., Pietersen, H., Piguet, B., Pique, E., Román-Gascón, C., Saï d, F., Sastre, M., Seity, Y., Steeneveld, G. J., Toscano, P., Traullé, O., Tzanos, D., Yagüe, C., Wacker, S., Wildmann, N., and Zaldei, A.: The BLLAST field experiment: Boundary-Layer Late Afternoon and Sunset Turbulence, Submitted to Atmos. Chem. Phys, 2014.

Lozano Sánchez, M.: WRF simulation of the atmospheric conditions in some aircraft accidents, Tech. rep., Universitat Politècnica de Catalunya · BarcelonaTech, Spain, 2013.

Luers, J. and Haines, P.: Heavy rain influence on airplane accidents, J. Aircra., 20, 187–191, 1983.

Mahrt, L.: Nocturnal boundary-layer regimes, Bound.-Lay. Meteorol., 88, 255–278, 1998.

Mahrt, L. and Lenschow, D. H.: Growth dynamics of the convectively mixed layer, J. Atmos. Sci., 33, 41–51, 1976.

Martin, S., Bange, J., and Beyrich, F.: Meteorological profiling of the lower troposphere using the research UAV M^{2}AV Carolo, Atmos. Mes., 4, 705–716, 2011.

Moeng, C. H.: A Large-Eddy-Simulation Model for the Study of Planetary Boundary-Layer Turbulence, J. Atmos. Sci., 41, 2052–2062, 1984.

Moeng, C.-H. and Sullivan, P. P.: A comparison of shear- and buoyancy-driven planetary boundary layer flows, J. Atmos. Sci., 51, 999–1022, 1994.

Moncrieff, J., Monteny, B., Verhoef, A., Friborg, T., Elbers, J., Kabat, P., de Bruin, H., Soegaard, H., and Taupin, J. D.: Spatial and temporal variations in net carbon flux during HAPEX-Sahel, J. Hydrol., 188-189, 563–588, 1997.

Monin, A. S., Yaglom, A. M., and Lumley, J. L.: Statistical Fluid Dynamics, The MIT Press, Massachusetts, USA, 1975.

Morris, G. A., Ford, B., Rappenglück, B., Thompson, A. M., Mefferd, A., Ngan, F., and Lefer, B.: An evaluation of the interaction of morning residual layer and afternoon mixed layer ozone in Houston using ozonesonde data, Atmos. Environ., 44, 4024–4034, 2010.

Mukund, V., Ponnulakshmi, V. K., Singh, D. K., Subramanian, G., and Sreenivas, K. R.: Hyper-cooling in the nocturnal boundary layer: the Ramdas paradox, Phys. Scripta, doi:10.1088/0031-8949/2010/T142/014041, 2010.

Mukund, V., Singh, D. K., Ponnulakshmi, V. K., Subramanian, G., and Sreenivas, K. R.: Field and laboratory experiments on aerosol-induced cooling in the nocturnal boundary layer, Q. J. R. Meteorol. Soc., 140, 151–169, 2013.

Nadeau, D. F., Pardyjak, E. R., Higgins, C. W., Fernando, H. J. S., and Parlange, M. B.: A simple model for the afternoon and early evening decay of convective turbulence over different land surfaces, Bound.-Lay. Meteorol., 141, 301–324, 2011.

Nadeau, D. F., Pardyjak, E. R., Higgins, C. W., Huwald, H., and Parlange, M. B.: Flow during the evening transition over steep Alpine slopes, Q. J. R. Meteorol. Soc., 139, 607–624, 2013.

Narasimha, R.: When and why air can be cooler than ground just below: A theory for the Ramdas effect, J. Indran. Inst. Sci., 71, 475–483, 1991.

Narasimha, R. and Vasudeva Murthy, A. S.: The energy balance in the Ramdas layer, Bound.-Lay. Meteorol., 76, 307–321, 1995.

Nieuwstadt, F. T. M.: The turbulent structure of the stable, nocturnal boundary layer, J. Atmos. Sci., 41, 2202–2216, 1984.

Nieuwstadt, F. T. M. and Brost, R. A.: The Decay of Convective Turbulence, J. Atmos. Sci., 43, 532–546, 1986.

Nunes, A. B., Campos Velho, H. F., Satyamurty, P., Degrazia, G., Goulart, A., and Rizza, U.: Morning Boundary-Layer Turbulent Kinetic Energy by Theoretical Models, Bound.-Lay. Meteorol., 134, 23–39, 2010.

Oke, T. R.: The temperature profile near the ground on calm clear nights, Q. J. R. Meteorol. Soc., 96, 14–23, 1970.

Ouwersloot, H. G., Vilà-Guerau de Arellano, J., van Heerwaarden, C. C., Ganzeveld, L. N., Krol, M. C., and Lelieveld, J.: On the segregation of chemical species in a clear boundary layer over heterogeneous land surfaces, Atmos. Chem. Phys, 11, 10 681–10 704, 2011.

Ouwersloot, H. G., Vilà-Guerau de Arellano, J., Nölscher, A. C., Krol, M. C., Ganzeveld, L. N., Breitenberger, C., Mammarella, I., Williams, J., and Lelieveld, J.: Characterization of a boreal convective boundary layer and its impact on atmospheric chemistry during HUMPPA-COPEC-2010, Atmos. Chem. Phys, 12, 9335–9353, 2012.

Pielke, R. A.: Mesoscale Meteorological Modeling, Academic Press, 2002.

Pietersen, H., Vilà-Guerau de Arellano, J., Augustin, P., de Coster, O., Durand, P., Gioli, B., Hartogensis, O., Lothon, M., Lohou, F., Pino, D., Ouwersloot, H. G., Reuder, J., and van de Boer, A.: Study of a prototypical convective boundary layer observed during BLLAST: contributions by large-scale forcing. , Submitted to Atmos. Chem. Phys, 2014.

Pike, W. S.: UK Weather-Related Civil Aircraft Accidents 1977-1986, Weather, 43, 214–220, 1988.

Pino, D. and Vilà-Guerau de Arellano, J.: Effects of shear in the convective boundary layer: analysis of the turbulent kinetic energy budget, Acta Geophys., 56, 167–193, 2008.

Pino, D., Vilà-Guerau de Arellano, J., and Duynkerke, P. G.: The Contribution of Shear to the Evolution of a Convective Boundary Layer, J. Atmos. Sci., 60, 1913–1926, 2003.

Pino, D., Jonker, H. J. J., Vilà-Guerau de Arellano, J., and Dosio, A.: Role of Shear and the Inversion Strength During Sunset Turbulence Over Land: Characteristic Length Scales, Bound.-Lay. Meteorol., 121, 537–556, 2006a.

Pino, D., Vilà-Guerau de Arellano, J., and Kim, S. W.: Representing Sheared Convective Boundary Layer by Zeroth- and First-Order-Jump Mixed-Layer Models: Large-Eddy Simulation Verification, J. Appl. Meteorol. Climatol., 45, 1224–1243, 2006b.

Pino, D., Vilà-Guerau de Arellano, J., Peters, W., Schröter, J., van Heerwaarden, C. C., and Krol, M. C.: A conceptual framework to quantify the influence of convective boundary layer development on carbon dioxide mixing ratio., Atmos. Chem. Phys., 12, 2969–2985, 2012.

Ponnulakshmi, V. K., Mukund, V., Singh, D. K., Sreenivas, K. R., and Subramanian, G.: Hypercooling in the Nocturnal Boundary Layer: Broadband Emissivity Schemes, J. Atmos. Sci., 69, 2892–2905, 2012.

Pope, S. B.: Turbulent Flows, Cambridge University Press, Cambridge, 2000.

Poulos, G. S., Blumen, W., Fritts, D. C., Lundquist, J. K., Sun, J., Burns, S. P., Nappo, C., Banta, R., Newsom, R., Cuxart, J., Terradellas, E., Balsley, B., and Jensen, M.: CASES-99: A comprehensive investigation of the stable nocturnal boundary layer, Bull. Amer. Meteor. Soc., 83, 555–581, 2002.

Ramdas, L. and Atmanathan, S.: The vertical distribution of air temperature near the ground at night, Beitr. Geophys, 37, 116–117, 1932.

Raschke, K.: Über das nächtliche temperaturminimum über nackten boden in Poona, Meteorol. Rundsch., 27, 1–11, 1957.

Reuder, J., Jonassen, M. O., and Olafsson, H.: The Small Unmanned Meteorological Observer SUMO: Recent developments and applications of a micro-UAS for atmospheric boundary layer researche, Acta Geophys., 60, 1454–1473, 2012.

Rizza, U., Miglietta, M. M., Degrazia, G. A., Acevedo, O. C., and Marques, E. P.: Sunset decay of the convective turbulence with Large-Eddy Simulation under realistic conditions, Physica A., 392, 4481–4490, 2013.

Román-Gascón, C., Yagüe, C., Sastre, M., Maqueda, G., Reuder, J., Lothon, M., Saïd, F., Cuxart, J., Martinez, D., and Molinos, F.: Wave-like Events detected from Microbarometers Measurements during BLLAST campaign, in: 20th Symposium on Boundary Layers and Turbulence/18th Conference on Air-Sea Interaction, American Meteorological Society, Boston (USA), 2012.

Sahlée, E., Smedman, A., Rutgersson, A., and Högström, U.: Influence of a new turbulence regime on the global air-sea heat fluxes, J. Climate, 121, 5925–5941, 2007.

Saïd, F., Corsmeier, U., Kalthoff, N., Kottmeier, C., Lothon, M., Wieser, A., Hofherr, I., and Pascal, P.: ESCOMPTE experiment: intercomparison of four aircraft dynamical, Atmos. Mes., 74, 217–252, 2005.

Sastre, M., Yagüe, C., Román-Gascón, C., Maqueda, G., Lothon, M., and Saïd, F.: Pressure perturbations and multi-scale analysis in the atmospheric boundary layer at the afternoon and evening transition during the BLLAST campaign, in: 20th Symposium on Boundary Layers and Turbulence/18th Conference on Air-Sea Interaction, American Meteorological Society, Boston (USA), 2012.

Seibert, P., Beyrich, F., Gryning, S. E., Joffre, S., Rasmussen, A., and Tercier, P.: Review and intercomparison of operational methods for the determination of the mixing height, Atmos. Environ, 34, 1001–1027, 2000.

Shao, P., Chang, Y., and Chen, H.: Analysis of an aircraft accident model in Taiwan, J. Air Trans. Manag., 27, 34–38, 2013.

Smedman, A., Högström, U., Hunt, J., and Sahlée, E.: Heat/mass transfer in the slightly unstable atmospheric surface layer, Q. J. R. Meteorol. Soc., 133, 37–51, 2007.

Soegaard, H.: Fluxes of carbon dioxide, water vapour and sensible heat in a boreal agricultural area of Sweden scaled from canopy to landscape level, Agr. Forest Meteorol., 98–99, 463–478, 1999.

Sokol, P., Stachlewska, I. S., Ungureanu, I., and Stefan, S.: Evaluation of the Boundary Layer Morning Transition Using the CL-31 Ceilometer Signals, Acta Geophys., 62, 367–380, 2014.

Sorbjan, Z.: Effects Caused by Varying the Strength of the Capping Inversion Based on a Large Eddy Simulation Model of the Shear-Free Convective Boundary Layer, J. Atmos. Sci., 53, 2015–2024, 1996.

Sorbjan, Z.: Decay of convective turbulence revisited, Bound.-Lay. Meteorol., 82, 501–515, 1997.

Sorbjan, Z.: A numerical study of daily transitions in the convective boundary layer, Bound.-Lay. Meteorol., 123, 365–383, 2007.

Sorbjan, Z.: Gradient-based scales and similarity laws in the stable boundary layer, Q. J. Roy. Meteorol. Soc., 136, 1243–1254, 2010.

Sorbjan, Z.: The Height Correction of Similarity Functions in the Stable Boundary Layer, Bound.-Lay. Meteorol., 142, 21–31, 2012.

Stensrud, D. J.: Elevated Residual Layers and Their Influence on Surface Boundary-Layer Evolution, J. Atmos. Sci., 50, 2284–2293, 1993.

Stensrud, D. J.: Importance of Low-Level Jets to Climate: A Review, J. Climate, 9, 1698–1711, 1996.

Stillinger, D. C., Helland, K. N., and Van Atta, C. W.: Experiments on the transition of homogeneous turbulence to internal waves in a stratified fluid, J. Fluid Mech., 131, 91–122, 1983.

Stull, R. B.: The Energetics of entrainment across a density interface, J. Atmos. Sci., 33, 1260–1267, 1976.

Stull, R. B.: An Introduction to Boundary Layer Meteorology, Springer Netherlands, Dordrecht, 1988.

Sullivan, P. P. and Edward, G. P.: The Effect of Mesh Resolution on Convective Boundary Layer Statistics and Structures Generated by Large-Eddy Simulation, J. Atmos. Sci., 68, 2395–2415, 2011.

Sullivan, P. P., Moeng, C.-H., Stevens, B., Lenschow, D. H., and Mayor, S. D.: Structure of the Entrainment Zone Capping the Convective Atmospheric Boundary Layer, J. Atmos. Sci., 55, 3042–3064, 1998.

Sun, J., Burns, S., Delany, A., Oncley, S., Horst, T., and Lenschow, D.: Heat balance in the nocturnal boundary layer during CASES-99, J. Appl. Meteorol., 42, 1649–1666, 2003.

Svensson, G., Holtslag, A. A. M., Kumar, V., Mauritsen, T., Steeneveld, G. J., Angevine, W. M., Bazile, E., Beljaars, A., Bruijn, E. I. F., Cheng, A., Conangla, L., Cuxart, J., Ek, M., Falk, M. J., Freedman, F., Kitagawa, H., Larson, V. E., Lock, A., Mailhot, J., Masson, V., Park, S., Pleim, J., Söderberg, S., Weng, W., and Zampieri, M.: Evaluation of the Diurnal Cycle in the Atmospheric Boundary Layer Over Land as Represented by a Variety of Single-Column Models: The Second GABLS Experiment, Bound.-Lay. Meteorol., 140, 177–206, 2011.

Tennekes, H.: A Model for the Dynamics of the Inversion Above a Convective Boundary Layer, J. Atmos. Sci., 30, 558–567, 1973.

Tennekes, H. and Driedonks, A. G. M.: Basic entrainment equations for the atmospheric boundary layer, Bound.-Lay. Meteorol., 20, 515–531, 1981.

Touil, H., Bertoglio, J. P., and Shao, L.: The decay of turbulence in a bounded domain, J. Turbul., 3, 049, 2002.

Van de Boer, A., Moene, A. F., Graf, A., Schüttemeyer, D., and Simmer, C.: Detection of Entrainment Influences on Surface-Layer Measurements and Extension of Monin-Obukhov Similarity Theory, Bound.-Lay. Meteorol., doi: 10.1007/s10546-014-9920-8, 2014.

Van den Kroonenberg, A. C., Martin, S., Beyrich, F., and Bange, J.: Spatially-Averaged Temperature Structure Parameter Over a Heterogeneous Surface Measured by an Unmanned Aerial Vehicle, Bound.-Lay. Meteorol., 142, 55–77, 2012.

Van Dijk, A., Moene, A. F., and De Bruin, H. A. R.: The principles of surface flux physics: theory, practice and description of the ECPACK library, Tech. rep., Internal Report 2004/1, Meteorology and Air Quality Group, Wageningen University, Wageningen, The Netherlands, 2004.

Van Driel, R. and Jonker, H. J. J.: Convective Boundary Layers Driven by Nonstationary Surface Heat Fluxes, J. Atmos. Sci., 68, 727–738, 2011.

Van Heerwaarden, C. C. and Vilà-Guerau de Arellano, J.: Relative Humidity as an Indicator for Cloud Formation over Heterogeneous Land Surfaces, J. Atmos. Sci., 65, 3263–3277, 2008.

Van Ulden, A. P. and Wieringa, J.: Atmospheric boundary layer research at Cabauw, Bound.-Lay. Meteorol., 78, 39–69, 1996.

Vasudeva Murthy, A. S., Srinivasan, J., and Narasimha, R.: Theory of the lifted temperature minimum on calm clear nights, Philos. T. R. Soc. A, 344, 183–206, 1993.

Vasudeva Murthy, A. S., Narasimha, R., and Varghese, S.: An asymptotic analysis of a simple model for the structure and dynamics of the Ramdas layer, Pure Appl. Geophys., 162, 1831–1857, 2005.

Vilà-Guerau de Arellano, J.: Role of nocturnal turbulence and advection in the formation of shallow cumulus over land, Q. J. R. Meteorol. Soc., 133, 1615–1627, 2007.

Vilà-Guerau de Arellano, J. and van Heerwaarden, C. C.: Atmospheric boundary layer: integrating chemistry and land interactions, to be published by Cambridge University Press, 2014.

Vilà-Guerau de Arellano, J., van den Dries, K., and Pino, D.: On inferring isoprene emission surface flux from atmospheric boundary layer concentration measurements, Atmos. Chem. Phys., 9(11), 3629–3640, 2009.

Wehner, B., Siebert, H., Ansmann, A., Ditas, F., Seifert, P., Stratmann, F., Wiedensohler, A., Apituley, A., Shaw, R. A., Manninen, H. E., and Kulmala, M.: Observations of turbulence-induced new particle formation in the residual layer, Atmos. Chem. Phys., 10, 327–360, 2010.

Yi, C., Davis, K. J., Berger, B. W., and S., B. P.: Long-Term Observations of the Dynamics of the Continental Planetary Boundary Layer, J. Atmos. Sci., 58, 1288–1299, 2001.

Zdunkowski, W.: The nocturnal temperature minimum above the ground, Beitr. Phys. Atmos., 39, 247–253, 1966.

Zulueta, R. C., Oechel, W. C., Verfaillie, J. G., Hastings, S. J., Gioli, B., Lawrence, W. T., and Paw U, K. T.: Aircraft Regional–Scale Flux Measurements over Complex Landscapes of Mangroves, Desert, and Marine Ecosystems of Magdalena Bay, Mexico, J. Atmos. Oceab Tech., 30, 1266–1294, 2013.

Acknowledgements

Un dia em van dir que fer una tesis doctoral era com pujar a una muntanya russa que es un període de la teva vida ple de satisfaccions i moments difícils. Durant aquest quatre anys han passat per la meva vida moltes persones que han deixat la seva empremta i que han estat molt importants per a poder recórrer aquest camí.

Primerament, m'agradaria agrair el meu director el Dr. David Pino per donar-me la oportunitat de poder realitzar aquesta tesi. El seus coneixements i la seva gran dedicació han estat crucials perquè aquest projecte arribés a bon port. A més, voldria agrair-li la seva paciència i el seu tracte proper durant els moments més durs.

I would like to thank Dr. Eric Pardyjak for the opportunity to do a stay in his group at the University of Utah. His knowledge in observational meteorology was really valuable to develop this thesis. Moreover, I would like to emphasize his friendly and positive attitude which encouraged me during my stay.

I would like to acknowledge all BLLAST participants for their effort to develop this successful field campaign without which I would not have been able to carry out this thesis. Specifically, I would like to thank Dr. Marie Lothon for her organizational skills and her enthusiasm in the BLLAST Project. Moreover, I would like to thank Dr. Jordi Vilà, Dr. Joachim Reuder, Dr. Joan Cuxart, Dr. Daniel Martinez, Dr. Fabienne Lohou, Dr. Oscar Hartogensis, Anneke van de Boer, Olivier De Coster, Clara Darbieu, Henk Pietersen and Daniel Alexander for sharing their observations and for giving me their opinions and advice during the development of the scientific papers.

M'agradaria agrair als meus companys de despatx, l'Araceli, l'Anna, la Gabriela, la Maria, la Ruxandra, el Shervin, el Chaoren, el Fuqiang, el Milad, el Fran, la Thirza, el Roger, la Isa, el Víctor i la Jazmin el seu suport i l'ajut durant el dia a dia. Voldria dir que en el "fondo sur" he trobat molt més que companys de feina, ja que ho considero una amistat que m'acompanyarà per sempre.

També voldria mostrar el meu agraïment als professors de la primera planta del C3, els quals m'han ajudat i orientat des de que era estudiant de carrera i que durant aquest últims anys s'han convertit també en els meus companys. Especialment, el Jordi Mazón pels seus consells científics i personals i tots els bons moments durant els congressos. No em puc oblidar tampoc d'alguns membres del personal d'administració i serveis com l'Ester Cantos, el Jordi Lino, el Toni Castillo, el Lluís Monfort, la Roser Pons o la Teresa Sanjose, moltes gracies pel vostre suport. Per altra banda, un agraïments sincer als companys del Consell de Doctorands els quals espero que segueixin endavant realitzant amb tan entusiasme aquesta tasca tan important.

I would also like to thank the support of the colleagues from the University of Utah. They welcomed me as one of the team and we had really nice scientific and personal discussions. Konkretno, ja bih da se zahvalim Emina prijateljstvo.

Les nenes també han jugat un paper important durant aquests anys. Han estat participes dels bons moments, mostrant tot el seu entusiasme i dels moments difícils, donant-me tot el seu suport. Per tant, els vull agrair que sempre hagin estat al meu costat.

Finalment, voldria agrair a la meva família, especialment als meus pares i al Josep, el seu suport incondicional i el seu amor sincer. M'heu ensenyat que amb esforç tot es possible i que si creiem en nosaltres mateixos som molt forts.

Resumint, moltes gràcies, muchas gracias, thanks, merci, danksagung ... sense tots vosaltres aquesta aventura no hagués estat possible.

List of presentations and publications

Poster presentation

- Estel Blay-Carreras, D. Pino, J. Vilà, A. van de Boer, O. de Coster, I. Faloona, O. Garrouste, O. K. Hartogensis, M. Jonassen, D. Legain, F. Lohou, M. Lothon, H. Pietersen, C. Román-Cascón, J. Reuder, F. Said, M. Sastre, O. Traulle, and C. Yagüe: *Role of residual layer and large-scale phenomena on the evolution of the boundary layer* in: 20th Symposium on Boundary Layers and Turbulence/18th Conference on Air-Sea Interaction, American Meteorological Society, Boston (USA), 2012.

Oral presentation

- Estel Blay-Carreras: *Numerical simulations of 1st and 2nd July with mixed-layer model and large eddy simulation* in: BLLAST Workshop: Outcome of the 2011 BLLAST field experiment, Firenze, Italy, 2012.

- Estel Blay-Carreras, E. Pardyjak, D. Pino, M. Lothon and F. Lohou: *An investigation of the failure of flux gradient theory during the evening transition period* in: EGU General Assembly 2013, Vienna, Austria, 2014.

  - Award: Young Scientist Travel Awards

- Estel Blay-Carreras, E. Pardyjak, D. Pino, M. Lothon and F. Lohou: *Analysis of the decoupling between surface heat flux and temperature gradient during afternoon transition* in: EMS Annual Meetings - European Meteorological Society, Reading, UK, 2013.

  - Award: Young Scientist Travel Awards

Publications

- Blay-Carreras, E., Pino, D., Van de Boer, A., De Coster, O., Darbieu, C., Hartogensis, O., Lohou, F., Lothon, M., Pietersen, H., and Vilà-Guerau de Arellano, J.: Role of the residual layer and large-scale subsidence on the development and evolution of the convective boundary layer, Atmos. Chem. Phys., 14, 4515-4530, 2014.

- Blay-Carreras, E., Pardyjak, E., Pino, D., Lohou, F., and Lothon, M.: Countergradient heat flux observations during the evening transition period, Atmos. Chem. Phys. Discuss., 14, 7711–7737, 2014.

- Lothon, M., Couvreux, F., Durand, P., Hartogensis, O., Legain, D., Lohou, F., Pardyjak, E. R., Pino, D., Reuder, J., Vilà-Guerau de Arellano, J., Alexander, D., Augustin, P.and Bargain, E., Barrié, J., Bazile, E., Bezombes, Y., Blay- Carreras, E., van de Boer, A., Boichard, J. L., de Coster, O., Cuxart, J., Dabas, A., Darbieu, C., Deboudt, K., Delbarre, H., Derrien, S., Faloona, I., Flamant, P., Fourmentin, M., Garai, A., Gibert, F., Gioli, B., Graf, A., Groebner, J., Guichard, F., Jonassen, A., von Kroonenbeerg, M., Lenschow, D., Martin, S., Martinez, D., Mastrorillo, L., Moene, A., Molinos, F., Moulin, E., Pietersen, H., Piguet, B., Pique, E., Román-Gascón, C., Saï d, F., Sastre, M., Seity, Y., Steeneveld, G. J., Toscano, P., Traullé, O., Tzanos, D., Yagüe, C., Wacker, S., Wildmann, N., and Zaldei, A.: The BLLAST field experiment: Boundary-Layer Late Afternoon and Sunset Turbulence, Atmos. Chem. Phys. Discuss., 14, 10789-10852, 2014.

- Blay-Carreras, E., Pardyjak, E., Pino, D., Hoch, S. W., Cuxart, J., Martínez, D. and Reuder, J.: Lifted Temperature Minimum During the Atmospheric Evening Transition, to be submitted to Atmos. Chem. Phys., 2014.

List of Figures

List of Tables